Spin-flip inelastic electron spectroscopy

Aaron Hurley

A thesis submitted for the degree of
Doctor of Philosophy
School of Physics
Trinity College Dublin

October 2012

Declaration

I, Aaron Hurley, hereby declare that this dissertation has not been submitted as an exercise for a degree at this or any other University.

It comprises work performed entirely by myself during the course of my Ph.D. studies at Trinity College Dublin. I was involved in a number of collaborations, and where it is appropriate my collaborators are acknowledged for their contributions.

A copy of this thesis may be lended or copied by the Trinity College Library upon request by a third party provided it spans single copies made for study purposes only, subject to normal conditions of acknowledgement.

Abstract

Recent experimental advances in scanning tunneling microscopy make the measurement of the conductance spectra of isolated and magnetically coupled atoms on nonmagnetic substrates possible. The typical example is that of Co, Fe or Mn atoms deposited on CuN. Notably, the conductance spectra are characterized by a competition between the Kondo effect and spin-flip inelastic electron tunneling. In this thesis, the interaction between electron spins and local spins is treated at the level of the non-equilibrium Green's function scheme for electron transport. It will be demonstrated that the Green's function method is capable of a semi-quantitative description of the competition between Kondo resonances and spin-flip inelastic electron tunneling at a computational cost significantly lower than that of other approaches. The theory is also extended to explain spin and non-spin polarized STM probes and to cases when the spin-system is driven out of equilibrium.

The predictive power of the Green's function method will also be implemented for hypothetical experiments that could provide insight into future spintronics devices. Firstly, the electric field induced spin-crossover effect, which has been predicted for two-centre dimers and molecular nonowires, will be investigated. Using the second order perturbation theory the conductance spectrum of a dimer containing spin 1/2 atoms will be calculated and it will be shown that spin-crossover manifests itself as a large population dependent dip in the conductance. Secondly, it will be predicted that a quantum spin Hall current, spontaneously generated at the edge of a two-dimensional topological insulator, acts as a source of spin-pumping for a magnetic impurity with uniaxial anisotropy, lead-

ing to the possible manipulation of the impurity spin direction by means of an electrical current without using either magnetic electrodes or an external magnetic field.

Acknowledgments

I rith théimhse mo dhoctúireacta fuair mé tacaíocht agus cabhair riachtanach ó roinnt daoine gur gá dom a lua anseo. Gan iad, ní bheinn ábalta puinn don taighde a rinne mé a chuir i gcríoch. Tá mé an-bhuíoch astu.

During my PhD I received a great deal of important help and support from a number of people that I must mention here. Without them I would not have been able to finish the research that I had undertaken. I am very thankful for them.

First and foremost I would like to thank my esteemed mentor and supervisor Prof. Stefano Sanvito. From humble beginnings in the archway underneath the railway, supervising one student and one post-doc, Stefano has assembled one of the largest groups in the school of physics and one of the largest theoretical and computational groups in Ireland. I have found his most impressive quality to be his ability to understand intimately the details of each group members project, no matter how large the group has grown over the years, and offer sound constructive criticism when sought. I have often left meetings with Stefano feeling rejuvenated and ready to tackle new problems, providing the perfect tonic when the course of the Ph.D begins to suppress one's enthusiasm! I have benefited greatly from his advice and teachings during my time in his research group and am extremely grateful for his support.

During the last four years I have seen roughly 22 group members come and go. Of this 22, the one member of the group with whom I conferred with the most and co-authored in three publications is Dr. Nadjib Baadji. I would regard Nadjib as my second supervisor

and his patience and sincerity in dealing with any technical problems I encountered (no matter how trivial) was admirable. The expertise that he imparted on the fundamental aspects of many-body physics and on density functionl theory (DFT) was vital and for this I am extremely thankful. To this end I would also like to acknowledge Dr. Ivan Rungger for supplying the relaxed CuN structure that was used in the DFT calculations and also Awadhesh Narayan with whom I co-authored a paper that required his specialist knowledge of the field of topological insulators.

The other members of the group both past and present with which I had many useful discussions during my PhD are Dr. Akinlolu Akande, Dr. Das Pemmaraju, Dr. Igor Popov, Dr. Nuala Caffrey, Dr. Andrea Droghetti, Dr. Mauro Mantega, Dr. Sankar Kesanakurthi, Dr. Anna Pertsova, Dr. Maria Tsoneva, Dr. Xihua Chen, Dr. Ruairí Hanafin, Dr. Clotilde Cucinotta, Amaury Melo Souza, Sandip Bhattacharya, Kapildep Dolui, Thomas Cathcart, Ismaeil Abdolhosseini Sarsari and Stefania Sanvito. Special thanks is reserved for Dr. Tom Archer who was always kind enough to solve any computer issues that would arise.

There are also a number of external collaborators that have aided me throughout my thesis. From the theoretical side, I garnered a lot of information from communications with Dr. Magnus Paulsson, Prof. Carlo Canali, Prof. Mats Persson and Dr. Bjorn Sothmann, all of whom have dealt with spin scattering using the model Hamiltonian approach as in this thesis. From the experimental side I would like to thank Dr. Cyrus Hirjibehedin and Dr. Alexander Otte for providing the experimental data that is shown throughout this work and also in other publications.

The research carried out in this work could not be achieved without funding and this was generously provided by the Irish Research Council for Science, Engineering & Technology (IRCSET). Additional funding was also provided by the Science Foundation of Ireland. I would also like to thank CRANN, the Centre for Research on Adaptive Nanostructures and Nanodevices, which provided the office space and suitable working

environment all throughout my PhD. Computational resources were provided by the Trinity Centre for High Performance Computing (TCHPC).

Finally I would like to thank my family and friends, my parents Liam and Marian, my sister Clodagh, my brother Gavin and great friend Tony Hegarty for their unbounded help and support over my cumulative 22 years of education. I would also like to acknowledge useful philosophical discussions with James Sweeney, Ronan Fahey and Dave Kissane over many's the creamy pint of Beamish!

Contents

List of Figures

List of Tables

Chapter 1

Introduction

1.1 Inelastic electron tunneling spectroscopy

Inelastic electron tunneling spectroscopy (IETS) has become an important tool for investigating the elementary excitations of nanoscale systems [1]. An excitation manifests itself as an abrupt change in the differential conductance of a two-probe device as the voltage sweeps across the excitation energy. This is the result of the opening of a new inelastic transport channel for the electron tunneling. As the energy of the probed excitation sets the critical voltage and the temperature range to observe IETS, it is not surprising that the first experiments were all related to molecular vibrations of relatively high energy [2].

In this thesis, the spin degree of freedom of individual atoms will define the inelastic channel as mentioned above. In particular the interaction between conduction electrons and localized spins in transition metals with partially filled d shells is central to many low-temperature spin effects, which may underpin the development of spintronics and quantum information devices. When adsorbed on the surface of a metallic host (see Fig. 1.1(a)), magnetic transition metal atoms exhibit various distinctive features in the conductance spectrum, which are indicative of many-body scattering between the conduction electrons and the localized spins. These manifest themselves as conductance steps at voltages corresponding to the quasi-particle energies of specific magnetic excitations and as

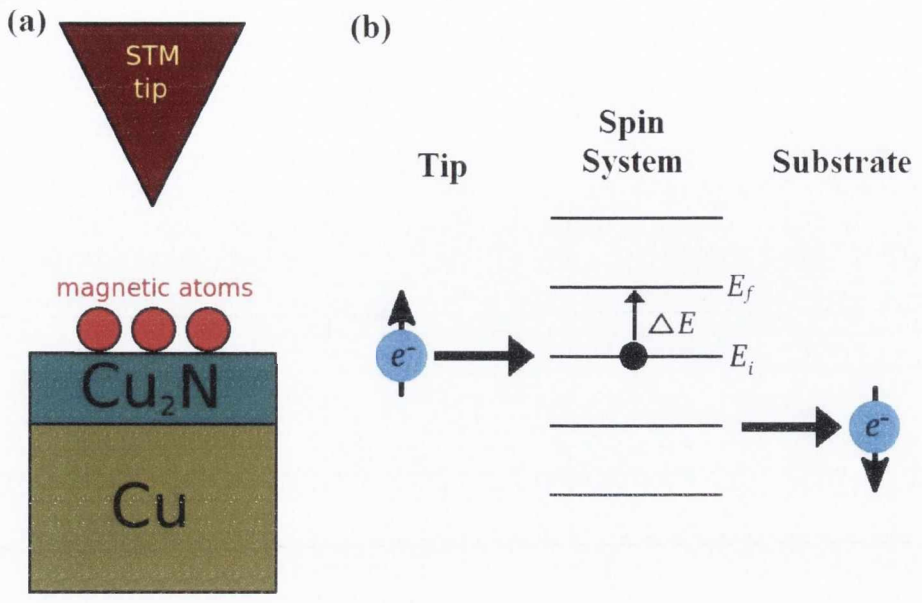

Figure 1.1: (a) Schematic representation of STM experiments where the spin degree of freedom of magnetic atoms on a metallic host are probed using an STM tip. (b) Cartoon showing the inelastic process. An incoming electron from the tip excites the spin system from initial energy E_i to final energy E_f. The scattered electron is spin-flipped and lowered in energy by $\Delta E = E_f - E_i$.

zero-bias conductance peaks, known as Kondo resonances. The various features in the conductance arise as the energy of the spin-scattered electrons is inelastically changed by $\Delta E = E_f - E_i$ when it travels from tip to substrate via the localized spins, as is seen in the cartoon of Fig. 1.1(b). Here E_f and E_i are the final and initial states respectively of the quasi-particle spin system. The first conductance features are associated to spin-flip inelastic electron tunneling and can be described by second order perturbation theory in the electron-spin coupling, but the second results from third order effects due to the electron screening of the local spins.

Recently the continuous advances in low-temperature scanning tunneling microscopy (STM) have allowed for the detection of excitations related to the spin degree of freedom. This type of spectroscopy is usually named spin-flip IETS (SF-IETS). The first measurements of SF-IETS were for single atoms randomly deposited on surfaces [3]. However, STM techniques also open the possibility of assembling and manipulating entire nanostructures [4] and of positioning magnetic ions on a surface at a desired position. This

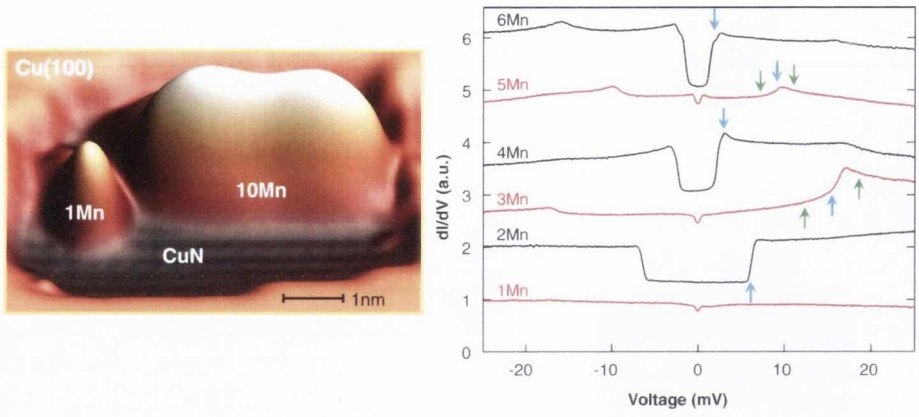

Figure 1.2: Experimental investigation of chains of Mn atoms on a CuN substrate [9]. The panel on the left shows an STM topograph image of Mn chains and the panel on the right shows the conductance steps indicating spin-flip events using IETS. For example, spin excitations for the Mn dimer are seen at $V = \pm 6$eV

enables the construction of atomic magnetic nano-structures and the study of the complex magnetic excitations, resulting from the exchange interaction between the magnetic ions and the substrate, and also between the magnetic atoms themselves. Such a novel fabrication capability has produced a surge of experimental studies on the spin excitations of magnetic nanostructures.

In particular, transition metal magnetic atoms on insulating surfaces, like Mn [5, 6] (see Fig. 1.2), Co [7, 8], Fe [9, 10, 11] and molecular chains composed of Co-phthalocyanines [12], have been the focus of intensive research in the last few years. This is accompanied by investigations of spin-based logic in chains of Fe atoms [13, 14] which can be coupled together to form all logical operations of a quantum bit. The atoms used in these experiments all have partially filled d-shells, which are highly localized and responsible for the magnetic moment, and extended s-like electrons, which are responsible for the electron conduction. In general s and d electrons interact via exchange coupling so that the magnetic structure is coupled to the conducting electrons. The magnetic atoms are usually deposited on carefully prepared CuN-decorated Cu surfaces, where the typical electronic coupling is weak enough that the magnetism is preserved, but it is sufficiently

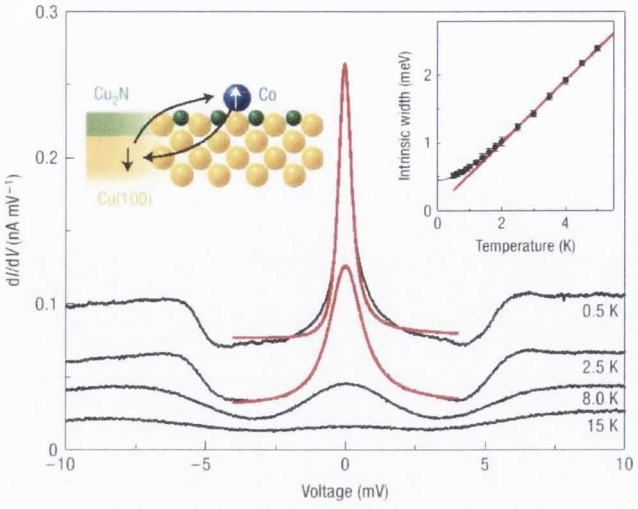

Figure 1.3: The emergence of the Kondo peak is observed at extremely low temperatures for a Co atom deposited on CuN. The additional conductance steps at $V \approx \pm 5$mV represent spin-flip events in the $s = 3/2$ manifold [7]. The inset indicates the variation of the Kondo peak width as the Kondo temperature increases.

strong to break the atomic central symmetry so that magnetic anisotropy develops. STM experiments are then conducted to probe the IETS spectra.

The Kondo effect is the screening of a magnetic impurity due to the exchange coupling between the localized spin and the conduction electrons in the surrounding environment. It manifests itself as a low-energy peak in the conductance as the screened local spin becomes a non-magnetic state and occurs at low temperatures. The detection of Kondo scattering events in Co [7, 10] and Fe adatoms adsorbed on a CuN insulating substrate have also been unearthed by the advent of IETS experiments. Co atoms in particular exhibit interesting Kondo physics and STM experiments have demonstrated the dependence of the Kondo peak on an applied magnetic fields, on the temperature and also on the spatial extent of individual cobalt complexes [8, 15]. The reduced symmetry of the surface leads to significant magnetic anisotropy, especially for Fe and Co. Fe is found to have a large easy-axis anisotropy ($D < 0$), leading to a ground state spin close to that of the maximum z-component of the integer $S = 2$. This results in four evenly spaced conductance steps in the spectrum. For Co the large hard-axis anisotropy ($D > 0$) and

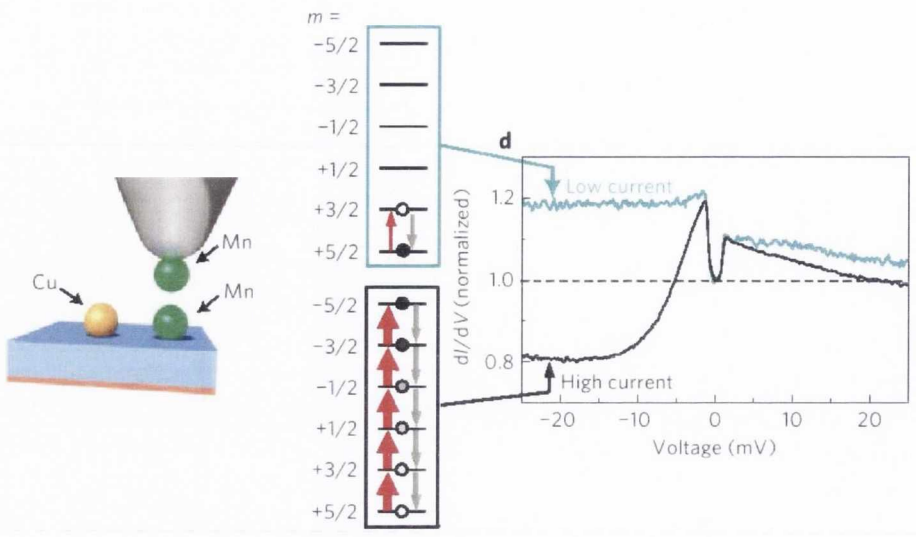

Figure 1.4: Spin polarized STM experiments. Left panel: A Mn-terminated tip yields spin-polarization in the tips electronic density of states. Right panel: The result of IETS experiments with a spin polarized tip is seen here where the low-current spectra (blue) are recorded at a large tipsample distance and the high current spectrum at a reduced tipsample distance. The inelastic step occurs at $V = \pm 0.7$meV and the bias asymmetry is indicative of a spin polarized tip. The Spin-state diagrams schematically show transitions occurring for negative V at low and high spin-polarized currents, respectively.

the half-integer $S = 3/2$ spin produce a doublet ground state. It can be seen from Fig. 1.3 that the measured zero-bias Kondo resonance is then due to spin transitions between the degenerate ground state levels [16]. In addition to the Kondo peaks observed in single Co atoms, single tetracyanoethyelene (TCNE) molecules on Cu(111) are reversibly switched among five states by applying voltage pulses with the tip of a scanning tunneling microscope. One of these states exhibits a large Kondo peak at the Fermi energy and indicates that it is magnetic. This can therefore represent a type of nanoscale "Kondo" switch [17, 18]. Kondo resonances also manifests themselves in heavy fermions like URu_2Si_2 [19] (where the Kondo resonance in this case is a anomaly in the low bias bulk conductance) and in magnetic dimers where the Kondo peak emerges from singlet to triplet transitions [20].

Interesting spin-probing and spin-manipulating features can be explored by a spin-polarized STM tip, where the tip density of states is spin split between majority (spin up) and minority (spin down) carriers. Spin polarization is achieved by placing a magnetic

atom at the apex of the STM tip. This results in a bias asymmetry, with different conductance step heights for positive and negative biases [6, 11]. Spin selection rules enforce a suppression of the inelastic scattering depending on whether electrons tunnel from tip to substrate or vice-versa. This results in a conductance profile which is asymmetric with respect to the applied bias, whose magnitude depends directly on the polarization of the tip. It is also well understood that by driving the spin out of equilibrium (by decreasing the tip-to-sample distance) the conductance lineshape changes [6, 11] as is seen in Fig. 1.4. In this case one must assume that the tunneling electrons will influence the spin of the atom as the time between two inelastic events (or the charging time) is small compared to the spin relaxation time (the time taken by the spin to relax back to its ground state). A tunneling electron can then encounter the local spin in an excited state far from equilibrium. The population of the quantized spin states is then bias-dependent and for a spin-polarized system this enhances the asymmetry of the conductance profile lineshape.

The recent rapid growth in the experimental activity has been matched by an equally fast explosion of theoretical works. A general and now standard approach to calculating the conductance spectra of the various possible magnetic nanostructures is that of combining a master equation solver for the quantum transport problem with a model Hamiltonian describing the magnetic interaction [21]. This is an intrinsic many-body approach, which in principle contains all the ingredients needed for solving the problem, once the various transfer rates are known. As such it usually requires a large number of parameters to be predictive. It is also difficult to incorporate the density of states of the electrodes and as such is limited when looking to describe 2 or 3 dimensional systems. An alternative strategy consists in treating the problem at the single particle level, by using a tunnel Hamiltonian and/or the standard Tersoff-Hamann description [22] for the STM current [23, 24, 25, 26]. This second class of computational scheme appears more amenable to be implemented together with first principles electron transport methods. However it still remains a hybrid theory, where the dynamic part of the problem needs to

be approached at the model Hamiltonian level, although the level of sophistication may include effects related to current generated non-equilibrium spin populations [27, 28].

Theoretical attempts to reproduce the conductance spectra have focused largely on including second order scattering events, which cannot account for Kondo resonances but fare well in reproducing the conductance steps and their relative intensities [23, 24, 25, 26, 27, 28, 29, 30, 31]. Addressing Kondo physics in Co is more involved and one has to look for alternative techniques, such as Wilson's numerical renormalization group theory [32] informed by density functional theory (DFT). This is an inherently non-perturbative approach which was developed to counteract the failings of perturbation theory at energies close to the Kondo temperature, T_K. The method creates a "logarithmically discretized" conduction band where energy intervals become exponentially smaller as the Fermi energy is approached. This makes the low-energy spectrum accessible and has formed the basis of many theoretical descriptions of the Kondo phenomenon in Co [33, 34, 35, 36] and in 2-channel phonon-assisted Kondo systems [37, 38]. Alternative techniques are based on the Anderson model of exchange interaction between a local impurity and conduction electrons. These are generally treated at a mean-field level [39, 40, 41] and achieve good qualitative agreement with experimental results. The Kondo problem has also been addressed by using quantum Monte-Carlo methods [42] and more recently the validity of time dependent density functional theory (TDDFT) in reproducing Kondo physics has also been explored [43]. Although these schemes recreate well the conductance spectra for magnetic atoms exhibiting the Kondo effect, they are numerically expensive.

In order to describe conductance spectra that exhibit both spin-flip conductance steps and Kondo resonances, this work uses the standard theoretical approach to quantum transport. This is the non-equilibrium Green's function (NEGF) formalism [44, 45], whose mean-field version can be combined with state of the art electronic structure theories to produce efficient and predictive algorithms [46, 47]. It is to date the only fully quantitative quantum transport approach capable of scaling to large systems [48] with multiple

dimensions, i.e. it is the only one capable of performing simulations for materials set of current technological relevance. As such, the NEGF method has an additional advantage over the master equation approach. This will prove highly advantageous when investigating IETS of magnetic atoms on 2D topological strips which will be introduced later in the discussion. Importantly, inelastic contributions to the elastic current can also be included within the NEGF formalism. In the case of scattering to phonons the problem is usually treated perturbatively by constructing an appropriate self-energy at the level of either the first (1BA) or the self-consistent Born approximation (SCBA) [49]. A similar approach to the case of spin excitations is currently not available.

There are two main reasons for this gap. On the one hand, the separation between the electronic degrees of freedom and those responsible for the inelastic excitations are well defined in the case of nuclear motion (phonons) but less clear in the case of spins, since even extremely localized spins have full electronic origin [50]. On the other hand, it is also unclear whether the perturbative approach is valid for spins, i.e. whether a suitable expansion parameter can be found. As such, as far as it is known, an expression for a self-energy describing inelastic spin-flip events has not been derived so far.

In the present work this challenge is undertaken and a perturbative theory of spin-flip spectroscopy based on the NEGF formalism for electron transport is formulated. The theoretical analysis is based on a tight-binding Hamiltonian for the transport electrons, which are locally exchange coupled to quantum spins. As such the formulation works by assuming a separation between the transport electrons and the local spins and it is constructed over the *s-d* model for magnetism [51]. An appropriate self-energy for the spin-degrees of freedom up to third order in the interaction is calculated and this is used in the standard NEGF scheme for transport. This self-energy is spin dependent and can therefore be used to describe spin-polarized STM experiments which exhibit asymmetric conductance spectra. By calculating the corresponding local spin self energy, the effect that conduction electrons have on the magnetic atom can also be explored. This can be

used to evaluate the population of different spin states when the spin system is driven out of equilibrium by increasing the current.

An inherent bias asymmetry of the conductance traces of STM experiments on adatoms also exists in non-spin polarized systems. This has been revealed experimentally [9]. In particular this appears to be quite prominent for both single Mn atoms and Mn monoatomic chains. This feature has been previously ascribed to an effect arising from a shifting of the density of states of the atom producing scattering. Such a density of state effect generates a non-trivial slope in the conductance as a function of bias [53]. The density of states shift however does not account for the asymmetry seen in the inelastic step heights, which also depends on bias and on the ratio between tip and substrate coupling to the sample [54, 55]. Here an alternative theoretical description based on the real part of the interacting self energy is provided, which allows a better fit the experimentally found conductance line-shape.

Within the approach developed in this thesis, a qualitative description of the behaviour of the Kondo peaks for Co, when this is exchanged coupled to another magnetic atom, will also be shown. However, due to the aforementioned restrictions of the perturbation method when describing Kondo resonances it cannot be claimed that an exact quantitative agreement with the experiments occurs. In addition for Fe, a quantitative description of the conductance step over-shooting subsequent to inelastic tunneling due to a magnetic excitation and to its decay as a function of bias is found. This was previously ascribed as originating from non-equilibrium effects [27], but here it is demonstrated to simply arise from the third order contribution to the interacting self-energy.

The NEGF formalism that will be outlined in this thesis to describe IETS experiments will be highly dependent on accurate values for different control parameters that enter the scheme. These involve the tip-to-sample coupling strength, the onsite energy of the localized impurity, the spin quantum number of the impurity, the exchange coupling between the local spins and the conduction electrons, the Lande g factor and also the

axial and transverse anisotropy terms. All of these parameters will be extracted either from DFT calculations or directly from experiments. Of particular interest also is the calculation of the magnetic anisotropy energy (MAE) of certain adatoms on surfaces [56, 57, 58]. A high MAE generally results in stable spin orientations which can be kept over years. In this thesis DFT will be used to extract values for the anisotropy for various magnetic atoms and in particular for an Fe-Cu dimer on CuN which until now has not been investigated theoretically. In this case it has been shown experimentally that the presence of the Cu atom drastically increases the anisotropy of the Fe-Cu system and therefore results in a stable spin orientation with long relaxation time [59]. It has also been suggested that the Fe-Cu system is also characterized by a larger than usual Lande g-factor, as it was found in other cases [60], and the validity of this will also be tested.

1.2 Theoretical method as a predictive tool

Having shown how to use the NEGF theory to explain the results of certain experiments, it is then useful to use the theoretical tools to predict future devices or novel experiments. In particular, two different experimental schemes that have gone unexplored to date wil be investigated and the theory will be used to predict what such experiments would reveal.

Firstly, the intriguing prospect of manipulating the magnetic configuration of the spin system with an electric potential rather than an electric current will be explored. It has been theoretically predicted that exchange coupling between local spins can be controlled electrically both for a two centre dimer [61] and a molecular nanowire [62]. It has been demonstrated that the dependence of the Stark shift of a given magnetic system on its magnetic state results in an exchange coupling parameter that has a quadratic dependence on the applied bias voltage. This enables spin-crossover from a low spin to high spin configuration, a crucial effect in the development of quantum information and spintronics devices [63].

In this thesis the possibility of using a scanning tunneling microscope (STM) to detect

the dependence of the exchange coupling on an electrical potential will be investigated. A bias-dependent conductance spectra of the most basic molecule comprising two coupled spin 1/2 atoms will be calculated. Previous attempts to investigate the electrically induced spin-crossover effect have focused on a classical description of the localized spin [64]. The fully quantum mechanical approach of this work, however, is a more realistic description of a possible experimental investigation of the spin-crossover effect in molecules. Furthermore, it can account for quantum excitations that are inaccessible by a closed spin-model. It will be shown that a critical voltage V_C exists where the conductance profile changes drastically during a spin-crossover between low spin and high spin. This effect is highly dependent on the population of the localized spin system and ultimately on the coupling between the STM tip and the localized spins.

Secondly it will be suggested that the quantum spin Hall (QSH) state can be coupled with IETS to probe and manipulate single magnetic atoms without the need of a magnetic field. The possibility of altering and controlling the spin-state of a single magnetic ion or of a small magnetic cluster with an external probe without the need of an external magnetic field represents a unique opportunity towards the understanding and the exploitation of the magnetic interaction at the most microscopic level. Possible areas of application for such ability may include spin-based quantum logic, where one necessitates to prepare, manipulate and read spin-qubits.

The QSH state is a new topological phase of matter which has attracted extensive attention in the past few years. It is a time-reversal invariant state characterized by a bulk gap which has gap-less *helical* edge states with opposite spins counter-propagating at a given edge. In a ground-breaking paper by Kane and Mele in 2005, it was shown that at low energies a QSH effect can be generated on a graphene sheet, subject to a spin- orbit interaction [65]. They also introduced the Z_2 topological invariant, which distinguishes it from an ordinary insulator [66]. However, the spin-orbit interaction in graphene is too small to realize this effect at realistic temperatures. Subsequently, Bernevig, Hughes

and Zhang predicted that HgTe/CdTe quantum wells exhibit this novel phase [67]. This prediction was soon confirmed by experiments [68, 69]. Three-dimensional analogs of QSH state have also been found and are generically termed topological insulators (TIs). More recently, evidence for helical edge modes in InAs/GaSb quantum wells has also been found [70]. Interestingly, Silicene and two dimensional Germanium have been predicted to exhibit QSH state at experimentally accessible temperatures [71, 72]. Furthermore, there are theoretical proposals to realize a QSH phase in graphene by using non-magnetic adatoms [73].

The proposal will be made that the QSH effect in Z_2 TIs can be exploited to probe and manipulate single magnetic atoms exhibiting a quantum spin. In Z_2 TIs, a spin-polarized current exists along the edge of the TI. Therefore an atomic spin coupled to such an edge can be manipulated in a similar way to spin-polarized STM experiments in the presence of an external magnetic field. In this case however, the same spin manipulations can be performed without the need of a magnetic field or a spin polarized tip. Although some theoretical work has been done recently investigating Kondo signatures of transition metal atoms [74] or spin baths coupled to TI edges [75], to the best of our knowledge, IETS investigations of TIs remains unexplored. Here IETS conductance spectra will be calculated using the NEGF formalism for single atoms on insulating substrates. It will be shown how this technique, when coupled to the QSH current, describes spin probing and manipulation on the edges of a TI.

1.3 Layout of thesis

The layout of the thesis is as follows. Chapter 2 will introduce the key concepts of DFT including the various approximation techniques that are employed for different systems. Chapter 3 then focuses upon the electronic Green's function formalism for electronic transport when a perturbation is applied to a non-interacting system. This formalism will then be implemented in Chapter 4 where the perturbation is introduced as the ex-

change coupling between electron spins and localized spins. This will lead to a derivation of the electron and local spin self-energies that can be expanded up to 3rd order in the perturbation expansion both for spin and non-spin polarized electrodes. Chapter 5 will then use the methods developed in Chapters 2, 3 and 4 to reproduce experimental conductance spectra of the transition metal atoms Co, Fe and Mn as a means of testing the validity of the formalism. The possibility of future IETS experiments will be probed in chapter 6, where the formalism will be employed to describe the hypothesized electric field induced spin crossover effect in two centre dimers and to investigate the spin manipulation of magnetic impurities on topological insulator edges. Chapter 7 will then provide the conclusions of the thesis.

Chapter 2

Density Functional Theory

The typical experimental setup for describing inelastic electron tunneling spectroscopy on a number of magnetic atoms involves an STM tip and an underlying insulating substrate. Since the STM tip is generally assumed to interact weakly with the magnetic atoms, the insulating substrate determines the principle electronic quantities of the device i.e. the magnetic anisotropy, the spin polarization, the coupling strength etc. The substrate is generally composed of an insulating layer of CuN, which decouples the magnetic atom from the bulk metallic Cu electrode. The entire device hence contains in excess of 100 atoms and represents a large many body problem. Describing such many-body systems using computational techniques that are both accurate and efficient is therefore a major electronic structure problem. The implementation of exact solutions to the many body problem generally scales poorly with the size of the device therefore approximations must be implemented. Techniques to describe the electronic structure of large systems range from the tight-binding method to the Hartree-Fock method [76]. In this thesis the most popular of ab-initio techniques, density functional theory (DFT) [77, 78, 79], will be used.

DFT is the most widely used approach to the many body problem due to its delicate mix between accuracy and efficiency. The technique reduces a full many body problem down to a series of single body equations defined within an effective potential which includes all the many body interactions. The main approximations lie in the calculation

of the exchange correlation functionals which is a quantity that includes all many body interactions in the problem. Different varieties of exchange correlation functional are implemented for varying degrees of accuracy in different systems, most of which will be explored in this chapter.

The starting point for any many-body problem in quantum mechanics is the many-body Schrödinger equation, which contains a Hamiltonian $\hat{H}$ acting on a many body wavefunction ψ resulting in an energy E

$$\hat{H}\psi = E\psi. \tag{2.1}$$

Throughout the thesis the unit-less parameter $\hbar = 1$ is assumed. The full many body Hamiltonian is then written as follows

$$\hat{H} = \sum_{i=1}^{N_e} \frac{-\nabla_i^2}{2m_e} + \sum_{I=1}^{N_N} \frac{-\nabla_I^2}{2M_I} + \frac{1}{2}\sum_{I\neq J}^{N_N} \frac{e^2 Z_I Z_J}{|\mathbf{X}_I - \mathbf{X}_J|} - \frac{1}{2}\sum_{i,I}^{N_e,N_N} \frac{e^2 Z_I}{|\mathbf{x}_i - \mathbf{X}_I|} + \frac{1}{2}\sum_{i\neq j}^{N_e} \frac{e^2}{|\mathbf{x}_i - \mathbf{x}_j|}, \tag{2.2}$$

where $\mathbf{x}_i$ is the position operator for the ith electron and $\mathbf{X}_I$ is the position operator for the Ith nucleus. The first and second term represent the kinetic energy of the electron with mass m_e and the nucleus with mass M_I respectively. The third term is the Coulomb interaction between the nuclei, the fourth term is the interaction between the electrons and the nuclei and the fifth term is the electron-electron interaction.

This problem can be simplified by employing the Born-Oppenheimer approximation which exploits the fact that the nuclei are much more massive than the electrons $M_N >> m_e$. Therefore it can be assumed that the nuclei remain fixed and unperturbed by the motion of the much lighter electrons. This allows for a separation of the electronic and nuclear components of the full many body wavefunction. The problem can then be reduced to that of a calculation of the eigenvalues of the many-body electron Hamiltonian, which

writes

$$\hat{H} = \sum_{i=1}^{N_e} \Big[-\frac{\nabla_i^2}{2} + v(\mathbf{x}_i) \Big] + \frac{1}{2} \sum_{i \neq j}^{N_e} \frac{e^2}{|\mathbf{x}_i - \mathbf{x}_j|},$$
$$= \hat{T} + \hat{V} + \hat{U}, \tag{2.3}$$

where it is now assumed that $m_e = 1$. The operators $\hat{T}$, $\hat{V}$ and $\hat{U}$ represent the kinetic energy, the Coulomb potential between electrons and nuclei (and any external field) and the electron-electron interaction respectively. The Schrödinger equation $H|\Psi\rangle = E|\Psi\rangle$ is then solved, leading to the many-body wavefunction $\Psi(\{\mathbf{x}_i\}, \{\sigma_i\})$ where $\mathbf{x}_i$ are the electron coordinates with spin σ_i. It then becomes a matter of defining a basis in which to expand the wavefunctions so that the Hamiltonian can be numerically diagonalize.

2.1 Hartree and Hartree-Fock theory

One such expansion is the method employed by Hartree [76], where the wavefunction, which is assumed to be spin degenerate, represents the simple product of single particle wavefunctions

$$\Psi_H(\{\mathbf{x}_i\}) = \psi_1(\mathbf{x}_1)\psi_2(\mathbf{x}_2)\ldots\psi_n(\mathbf{x}_n). \tag{2.4}$$

After writing Eq. (2.3) in second quantization form and finding the variation of the total energy with respect to the single particle orbitals, one arrives at the single particle equation in an effective potential. This is defined as the *Hartree equation*

$$\Big[-\frac{\mathbf{p}^2}{2} + v(\mathbf{x}) + v_H^i(\mathbf{x}) \Big] \psi_i(\mathbf{x}) = \varepsilon_i \psi_i(\mathbf{x}), \tag{2.5}$$

where ε_i are Lagrange multipliers and they approximate the ionization energies. The Hartree potential is written as

$$v_H^i(\mathbf{x}) = \sum_{j \neq i} \int d\mathbf{x}' \frac{|\psi_j(\mathbf{x}')|^2}{\mathbf{x} - \mathbf{x}'}, \tag{2.6}$$

which describes the density of a single orbital interacting with the potential of every other orbital. This is the most basic example of a mean field approximation to the electron-electron interaction. It must be solved self-consistently since the solution depends on the orbital density which itself is calculated at each self-consistent step.

The next approximation in the expansion of the wavefunction includes the spin of the fermionic electron and the takes into account the Pauli exclusion principle, which restricts the occupation of a single orbital to two electrons carrying opposite spin. The total electronic wave function must therefore be antisymmetric and this is trivially satisfied by expanding the wavefunction in linear combinations of *Slater* determinants. In this format the full wavefunction is expressed as

$$\Psi(\{\mathbf{x}_i\}, \{\sigma_i\}) = \begin{vmatrix} \psi_1(\mathbf{x}_1)\chi_1(\sigma_1) & \psi_2(\mathbf{x}_1)\chi_2(\sigma_1) & \dots & \psi_N(\mathbf{x}_1)\chi_N(\sigma_1) \\ \psi_1(\mathbf{x}_2)\chi_1(\sigma_2) & \psi_2(\mathbf{x}_2)\chi_2(\sigma_2) & \dots & \psi_N(\mathbf{x}_2)\chi_N(\sigma_2) \\ \vdots & \vdots & \ddots & \vdots \\ \psi_1(\mathbf{x}_N)\chi_1(\sigma_N) & \psi_2(\mathbf{x}_N)\chi_2(\sigma_N) & \dots & \psi_N(\mathbf{x}_N)\chi_N(\sigma_N) \end{vmatrix}. \tag{2.7}$$

Again imposing the variation principle (where the energy should be minimized by the ground state wave-function) one arrives at the Hartree-Fock equation

$$\Big[-\frac{\mathbf{p}^2}{2} + v(\mathbf{x}) + v_H(\mathbf{x}) \Big] \psi_i(\mathbf{x}) - \sum_j \delta_{\sigma_i \sigma_j} \int d\mathbf{x}' \frac{\psi_j^*(\mathbf{x}')\psi_j(\mathbf{x})}{\mathbf{x} - \mathbf{x}'} \psi_j(\mathbf{x}) = \varepsilon_i \psi_i(\mathbf{x}), \tag{2.8}$$

where, in comparison to the Hartree equation, the summation is now performed over all the j indexes. This eliminates the unwanted and unphysical self-interaction of an electron with the potential generated by itself, which will be discussed further at the end of the

chapter. Note also that the Hartree term in the square brackets becomes an integration over the full charge density $n(\mathbf{x})$ with

$$\begin{aligned} v_H(\mathbf{x}) &= \sum_j \int d\mathbf{x}' \frac{|\psi_j(\mathbf{x}')|^2}{\mathbf{x}-\mathbf{x}'}, \\ &= \int d\mathbf{x}' \frac{n(\mathbf{x}')}{\mathbf{x}-\mathbf{x}'}. \end{aligned} \tag{2.9}$$

The additional term is the exchange interaction which includes non-local terms such as $\psi_j(\mathbf{x})$ and is therefore much more difficult to solve than the Hartree equation.

Unfortunately, the Hilbert space for the above wavefunction technique grows like N^4, where N is the number of electrons, and therefore the problem becomes quickly intractable. Attention is then shifted to density functional theory where the underlying premise is that a calculation is made to determine the quantities $n(\mathbf{x})$ and E rather than the full many-body wavefunction, thereby decreasing the dimension of the Hilbert space.

2.2 Density Functional Theory

2.2.1 Hohnberg-Kohn Theorem

The central idea behind DFT is that the many-body wavefunctions and the energy of the many-body system are functionals of the external potential $v(\mathbf{x})$, i.e. $\Psi = \Psi[v]$ and $E = E[v]$, since this potential parametrizes the Hamiltonian. It has already been stated in the previous section that working with the full many-body wavefunction is not amenable so that the use of the electronic density of the system is sought as the principle means to evaluating relevant quantities such as the total energy. The electronic density is defined as

$$n(\mathbf{x}) = N \int \dots \int |\Psi(\mathbf{x}, \mathbf{x_1}, \mathbf{x_2}, \dots, \mathbf{x_N})|^2 d\mathbf{x_2} \dots d\mathbf{x_N}. \tag{2.10}$$

Hohnberg and Kohn [77] showed that the potential of a system of electrons is uniquely specified by the ground state charge density for the same system. They first established that, up to an arbitrary constant, the electron density n of a non-degenerate ground state uniquely determines the external potential $v(\mathbf{x})$. Therefore the electron density can be used to ascertain all the electronic properties of the ground state of the system. This drastically reduces the size of the calculations that one needs to be perform given that the many-body wavefunction is no longer explicitly required. The many-body Hamiltonian introduced in Eq. (2.3) can be re-written in terms of the electron density of the system

$$\begin{aligned} E[n] &= \langle \Psi[n] | \hat{H} | \Psi[n] \rangle, \\ &= \langle \Psi[n] | \hat{T} + \hat{U} + \hat{V} | \Psi[n] \rangle, \\ &= \langle \Psi[n] | \hat{T} + \hat{U} | \Psi[n] \rangle + \langle \Psi[n] | \hat{V} | \Psi[n] \rangle, \\ &= \hat{F}[n] + \int n(\mathbf{x}) v(\mathbf{x}) d\mathbf{x}, \end{aligned} \tag{2.11}$$

where $\hat{F}[n]$ is independent of the external potential.

Hohnberg and Kohn also proved a second theorem which establishes that the electron ground state which minimizes the above energy functional is the ground state electron density. In other words

$$E_0[n] = \min_n \Big\{ \hat{F}[n] + \int n(\mathbf{x}) v(\mathbf{x}) d\mathbf{x} \Big\}, \tag{2.12}$$

which can be proved using the variational principle [80]. Therefore it can be seen that DFT reduces the problem of an N part interacting system to that of finding a function $n(\mathbf{x})$, which minimizes the ground state energy functional $E_0[n]$. At this point a major problem remains in that the form of $\hat{F}[n]$ is in general not known exactly. Therefore approximations to this functional must be sought. Also note that DFT is useful only in determining the ground state of a system and it is not accurate nor theoretically sound when dealing with excitations. In such cases time dependent DFT (TDDFT) should be

employed [81].

2.2.2 The Kohn-Sham Theory

With the Hohnberg and Kohn theorems at hand, Kohn and Sham [78] set about transforming the problem of finding the ground state electron density to that of solving a series of non-interacting single particle Schrödinger equations. Finding the best approximation to the functional $\hat{F}[n]$ is also paramount to the Kohn-Sham theory. In deriving the Kohn-Sham equations, one must return to the expression for $\hat{F}[n]$ and note that from the second Hohnberg-Kohn theorem one arrives at

$$\hat{F[n]} = \langle \Psi_{\mathrm{GS}}[n] | \hat{T} + \hat{U} | \Psi_{\mathrm{GS}}[n] \rangle = \tag{2.13}$$

$$= \langle \Psi_{\mathrm{GS}} | \hat{T} | \Psi_{\mathrm{GS}} \rangle + E_{\mathrm{H}}[n] + \tilde{E}_{\mathrm{xc}}[n], \tag{2.14}$$

where the first term is the kinetic energy which is generally unknown for an interacting system due to the non local nature of the Laplacian operator. The second is the Hartree term, which is known exactly and is calculated as

$$E_{\mathrm{H}}[n] = \int d\mathbf{x} \int d\mathbf{x}' \frac{n(\mathbf{x}) n(\mathbf{x}')}{\mathbf{x} - \mathbf{x}'}. \tag{2.15}$$

The final term is the exchange/correlation energy and contains all the necessary terms beyond the Hartree energy which up to this point are unknown and must be approximated. One finds that there is a large contribution from the first two terms and a small contribution from the exchange energy.

At this point Kohn and Sham sought about looking for a better approximation to the kinetic energy. They noted that a certain system was known where the kinetic energy could be calculated exactly, the non-interacting system. They decided to implement this kinetic energy under the proviso that the electronic density in the non-interacting system was the same as that in the interacting one. As such the energy functional for the

interacting system can be rewritten as

$$E[n] = T_0[n] + \int d\mathbf{x} n(\mathbf{x}) \Big[v(\mathbf{x}) + \frac{1}{2} v_{\mathrm{H}}(\mathbf{x}) \Big] + E_{\mathrm{xc}}[n], \tag{2.16}$$

where the new exchange correlation functional also includes the difference in the two kinetic energy terms

$$E_{\mathrm{xc}}[n] = \tilde{E}_{\mathrm{xc}}[n] + (T[n] - T_0[n]). \tag{2.17}$$

The total energy functional for the non-interacting system is then

$$E_0[n] = T_0[n] + \int d\mathbf{x} n(\mathbf{x}) v_{\mathrm{eff}}(\mathbf{x}), \tag{2.18}$$

where it is assumed that an effective potential exists such that the density of the non-interacting system matches that of the interacting one. Now, by deriving the variational Euler-Lagrange equations [the functional derivative of both $E[n]$ and $E_0[n]$ with respect to $n(\mathbf{x})$] and eliminating the term $T_0[n]$, one arrives at an expression for the effective potential

$$v_{\mathrm{eff}}[n(\mathbf{x})] = v(\mathbf{x}) + v_{\mathrm{H}}[n(\mathbf{x})] + \frac{\delta E_{\mathrm{xc}}[n]}{\delta n(\mathbf{x})}. \tag{2.19}$$

This represents a single electron non-interacting system and therefore the problem is now reduced to the self-consistent calculation of the following Kohn-Sham equations for the one particle orbitals ϕ_i

$$\Big[-\frac{\nabla^2}{2} + v_{\mathrm{eff}}(\mathbf{x}) \Big] \phi_i(\mathbf{x}) = \varepsilon_i \phi_i(\mathbf{x}), \tag{2.20}$$

where $n(\mathbf{x}) = \sum_i^N f_i |\phi_i(\mathbf{x})|^2$ and f_i is the Fermi function. The problem has now been reduced to a set of non-interacting Schrödinger equations.

The Kohn-Sham set of equations can then be solved for the KS eigenvalues ε_i and the KS eigenvectors ϕ_i, which are correspondingly used to calculate the new charge density $n(\mathbf{x})$. The charge density is then used to find the new expression for the effective potential v_{eff} in Eq. (2.16). This scheme is iterated until self-consistency is reached (i.e. until the charge density doesn't change between consecutive iterations). The Hohnberg-Kohn theorems state that this must be the charge density of the actual system.

The Kohn-Sham orbitals ε_i do not represent physical quantities. They are the eigenvalues of the fictitious, non-interacting Kohn-Sham orbitals. However when using DFT to calculate observables like the total energy, the sum over all the occupied Kohn-Sham orbitals must be performed. Usually, the KS eigenvalues are used to calculate the band-structure of materials so that they are interpreted as single particle energies (note however that this is not justified by the theory itself). In this thesis the Kohn-Sham eigenvalues will also be assumed equivalent to resonances in the transmission coefficients in transport calculations.

At this point a theory has been developed that depends on the accuracy of the exchange correlation functional $E_{\text{xc}}[n]$. This quantity incorporates the difference between the kinetic energies of the non interacting and the interacting systems. It also includes the associated error to using the Hartree approximation for the many-body interactions in the system. Finally it takes into account that the final wavefunction might not be a single Slater determinant. As such all many body effects are contained in this quantity. The following subsection underlines the various approximation techniques used to evaluate this quantity.

2.2.3 Approximate Energy Functionals

The *local density approximation* (LDA) [78] is the simplest approximation to the exchange correlation functional and underlines all approximations to it. It is a local contribution since the potential at a particular point only depends on the charge density at that point. A homogeneous electron gas is used as the reference for the approximation. Instead of

the exactl exchange correlation (XC) functional for the real interacting system (which is unknown), an alternative is adopted where it is replaced with the XC energy of the homogeneous electron gas. The exchange and correlation energy density at position $\mathbf{x}$ is the one of the homogeneous electron gas calculated at the density at the same point $n(\mathbf{x})$. Therefore the approximate functional becomes:

$$E_{\mathrm{xc}}^{\mathrm{LDA}}[n] = \int n(\mathbf{x})\varepsilon_{\mathrm{xc}}(\mathbf{x})d\mathbf{x}, \tag{2.21}$$

where $\varepsilon_{\mathrm{xc}}(\mathbf{x})$ is the XC energy density per particle of the homogeneous electron gas. This is broken into an exchange and a correlation part respectively

$$\varepsilon_{\mathrm{xc}}(n(\mathbf{x})) = \varepsilon_{\mathrm{x}}(n(\mathbf{x})) + \varepsilon_{\mathrm{c}}(n(\mathbf{x})), \tag{2.22}$$

where the exchange part at a given density is known exactly [78]

$$\varepsilon_{\mathrm{x}}(n(\mathbf{x})) = -\frac{3}{4}\left[\frac{3n(\mathbf{x})}{\pi}\right]^{1/3}. \tag{2.23}$$

Although no exact expression is available for the correlation part of the functional, data from highly accurate numerical methods like Quantum Monte Carlo is used to estimate $\varepsilon_{\mathrm{c}}(n(\mathbf{x}))$.

To take into account spin-polarized systems the local spin-density approximation (LSDA) can be implemented by using the XC-energy for the homogeneous spin-polarized electron gas. This becomes a functional of both the up spin ($n_\uparrow$) and the down spin ($n_\downarrow$) electron density.

$$E_{\mathrm{xc}}^{\mathrm{LDA}}[n_\uparrow, n_\downarrow] = \int n(\mathbf{x})\varepsilon_{\mathrm{xc}}(n_\uparrow(\mathbf{x}), n_\downarrow(\mathbf{x}))d\mathbf{x}. \tag{2.24}$$

In situations where the electron density is approximately uniform i.e. metallic systems, the LDA approximation is quite successful. However, in many cases a large gradient in

the electron density exists which hinders the accuracy of the LDA. In this scenario the generalized gradient approximation (GGA) [82, 83, 84] was developed to cater for such occasions (useful in chemistry for the calculation of bond lengths). For GGA the XC functional is also written in terms of the density and of the gradient of the electron density

$$E_{\mathrm{xc}}^{\mathrm{LDA}}[n] = \int n(\mathbf{x})\varepsilon_{\mathrm{xc}}(n(\mathbf{x}), |\nabla n(\mathbf{x})|)d\mathbf{x}. \tag{2.25}$$

This can be systematically improved upon by further increasing the number of derivatives to the electron density however this also increases the computational effort required [83, 84]

There are certain systems where the treatment of the level of LDA/GGA fails in delivering the required accuracy of certain quantities. These systems generally show strong correlations. Where LDA/GGA breaks down is in the approximation's inability to cancel the self-interaction of electrons with themselves. This is called the self interaction error (SIE) and is somewhat rectified by implementing hybrid functionals which partially remove the SIE [85, 86]. The SIE does not exist in Hartree Fock methods and this combined with GGA offers a useful rectification to the problem. Some strongly correlated systems (systems that exhibit unusual electronic and magnetic properties due to a strong electron-electron correlation) are also handled better by using the LDA+U method, where U is a parameter that represents the screened electron-electron interaction [87, 88, 89, 90, 91]. The value of U is usually fitted to reproduce certain quantities like the band-gap or the lattice spacing and results in better approximations of the electronic and magnetic properties of strongly correlated systems like transition metal oxides. This will be dealt with in the following section.

2.3 LDA+U

The LDA+U method is established by separating electrons into two subsystems containing (i) localized d or f shell electrons which can be described by a mean-field approximation to Coulombic electron-electron interaction (the Hubbard model) as $\frac{1}{2}U\sum_{i\neq j} n_i n_j$ (where n_i are d-orbital occupancies) and (ii) delocalized s and p electrons which can be described using the one-electron LDA potential. With this at hand, the total energy functional can be rewritten as a correction to the LDA contribution

$$E^{\mathrm{XC}} = E^{\mathrm{XC}}_{\mathrm{LDA}} - UN(N-1)/2 + \frac{1}{2}U\sum_{i\neq j} n_i n_j, \tag{2.26}$$

where the first term is the LDA-XC energy and the second one is the Coulomb energy due to the d-d interaction of localized electrons with $N = \sum_i n_i$ and subtracts from the LDA energy functional. The last term is the Hubbard-like mean-field term. The Kohn-Sham dependent potential is then obtained by finding the variation of the total energy with respect to the charge density of a given ith orbital $V_i(\mathbf{x}) = \delta E/\delta n_i(\mathbf{x})$

$$V_i(\mathbf{x}) = V_{\mathrm{LDA}}(\mathbf{x}) + U\Big(\frac{1}{2} - n_i\Big). \tag{2.27}$$

Up until now direct and exchange Coulomb interactions inside a partially filled d atomic shell have been neglected, therefore these must be included to obtain a sound computational scheme to describe a single magnetic atom. This is achieved by identifying the regions of space where the electronic states show strong atomic characteristics, called 'atomic spheres'. In the case of d shell electrons this is largely the case anyway. The localized orthonormal basis is expanded within these spheres as $|inlm\sigma\rangle$ where i is the site, n is the main quantum number, l is the orbital quantum number, m is the magnetic quantum number and σ is the spin index. For the special case when a given $nl-$shell is

partially filled, the generalized LDA+U functional is defined as follows:

$$E^{\mathrm{XC}}_{\mathrm{LDA+U}} = E^{\mathrm{XC}}_{\mathrm{LSDA}} + E_U + E_{\mathrm{dc}}, \tag{2.28}$$

where E_{LSDA} is the standard local spin-density approximation energy functional and E_U satisfies

$$E_U[n] = \frac{1}{2}\sum_{\{m\},\sigma}\Big\{\langle m,m''|V_{ee}|m',m'''\rangle n^{\sigma}_{mm'}n^{-\sigma}_{m''m'''} - \Big[\langle m,m''|V_{ee}|m',m'''\rangle - \langle m,m''|V_{ee}|m''',m'\rangle\Big]n^{\sigma}_{mm'}n^{\sigma}_{m''m'''}\Big\}, \tag{2.29}$$

and V_{ee} is the screened Coulomb interaction amongst the nl-electrons. The last term in the expression accounts for the double counting (subtracts the LDA XC contribution from the functional) and is given by

$$E_{\mathrm{dc}} = \frac{1}{2}UN(N-1)/2 - \frac{1}{2}J[N^{\uparrow}(N^{\uparrow}-1) + N^{\downarrow}(N^{\downarrow}-1)], \tag{2.30}$$

where $N^{\sigma} = \mathrm{Tr}(n^{\sigma}_{mm'})$ and $N = N^{\uparrow}+N^{\downarrow}$. The screened Coulomb and exchange parameters are represented by U and J respectively. As shown previously, the variation of the total energy on the charge density $V^{\sigma}_{mm'} = \delta E/\delta n^{\sigma}_{mm'}$ yields an effective single-particle Kohn-Sham potential which is used in the final effective single-particle Hamiltonian

$$V^{\sigma}_{mm'} = \sum_{\{m\},\sigma}\Big\{\langle m,m''|V_{ee}|m',m'''\rangle n^{-\sigma}_{m''m'''} - \Big[\langle m,m''|V_{ee}|m',m'''\rangle - \langle m,m''|V_{ee}|m''',m'\rangle\Big]n^{\sigma}_{m''m'''}\Big\} - U\Big(N-\frac{1}{2}\Big) + J\Big(N^{\sigma}-\frac{1}{2}\Big). \tag{2.31}$$

The value for V_{ee} can be approximated from the assumption that within the atomic spheres, the interactions are largely atomic in nature and, as such, it is determined from the LSDA approximation. The parameters U and J are retained as input parameters and

for materials that concern this work are usually of the order of eV. Note however, that there are also a number of ways to evaluate U and J from first principles, mostly based on linear response theory [92], however this will not be evoked in this thesis.

2.4 DFT in practice

2.4.1 Basis Set

Having described a formula for reducing the many-body problem to that of solving a series of one body Kohn-Sham equations in an effective field, which incorporates accurate approximations to the many body interaction, now an appropriate basis-set is needed in which to expand the KS orbitals ϕ_i appearing in the KS equation

$$\Big[-\frac{p^2}{2} + v_{\text{eff}}(\mathbf{x})\Big]\phi_i(\mathbf{x}) = \varepsilon_i\phi_i(\mathbf{x}). \tag{2.32}$$

For a generic basis set $|\chi_\alpha\rangle$, one can expand the KS orbitals as $|\phi_i\rangle = \sum_\alpha c_i^\alpha|\chi_\alpha\rangle$, in order to arrive at the following generalized linear eigenvalue problem

$$\sum_\alpha \langle\chi_\beta|H|\chi_\alpha\rangle c_i^\alpha = \varepsilon_i \sum_\alpha \langle\chi_\beta|\chi_\alpha\rangle c_i^\alpha, \tag{2.33}$$

$$\sum_\alpha H_{\beta\alpha}c_i^\alpha = \varepsilon_i \sum_\alpha S_{\beta\alpha}c_i^\alpha, \tag{2.34}$$

$$\sum_\alpha \langle\chi_\beta|H|\chi_\alpha\rangle c_i^\alpha = \varepsilon_i \sum_\alpha \langle\chi_\beta|\chi_\alpha\rangle c_i^\alpha, \tag{2.35}$$

$$\sum_\alpha H_{\beta\alpha}c_i^\alpha = \varepsilon_i \sum_\alpha S_{\beta\alpha}c_i^\alpha, \tag{2.36}$$

$$(\mathbf{H} - \varepsilon_i\mathbf{S})\mathbf{c}_i = 0, \tag{2.37}$$

where $\mathbf{S}$ is the overlap matrix between basis set orbitals. The full solution requires matrix diagonalization on operation, which scales with the cube of the dimension of the basis set and it is generally performed by using computational libraries Lapack/Blas.

The choice of basis set now become important as this determine the efficiency of the calculation, the simplicity of use and the completeness. In general there are three classes of basis set each with its own advantages and disadvantages:

The choice of basis set now becomes important as this determines the efficiency of the process, the simplicity of use, and the completeness. In general there are three classes of basis-set each with varying advantages and disadvantages.

- Plane waves: Here a finite number of plane-wave functions are used to expand the basis set. A specific cutoff energy is chosen for a given calculation. These are simple and describe every point in space, are in principle complete and moderately efficient. (examples include VASP, WIEN2K etc.)

- Augmented functions: In this case the basis set is expanded in terms of hallow Gaussian functions which more accurately represent the tail portion of the atomic orbitals. These are in general quite complicated but very efficient since they do not deal with the entire space. (examples include GAUSSIAN, ASW)

- Local orbitals, LCAO: Expansion is performed in this case over the single atomic wavefunctions. These are somewhere in between the two and use sparse matrices for computation. They are also the most chemically intuitive. (examples include SIESTA, BAND)

The problem of choosing the correct basis set lies in the electronic structure of different atoms in the periodic table of elements, in particular the fact that atoms have a shell structure with different numbers of electrons occupying the s, p, d and f shells. Consequently, there are two classes of electronic states in solids; core states which are localized with a weak spread of electrons over the material and valence states which are delocalized and show a large spread of electrons over the material. Both states therefore require a contrasting basis set expansion, one localized and one delocalized. A problem then arises when one wants to use one basis set to describe a given material.

Furthermore, the effective potential of a given material has quite different characteristics close to and far away from the nucleus. Close to the nucleus the potential is deep and Coulomb-like because it represents the 1/r strong repulsion close to the nucleus. In the interstitial region between atoms and far from the centre of the nucleus, the effective potential is described by smooth, flat potentials as electron screening takes place. A general approximation

The problem with choosing the 'correct' basis set lies in the electronic structure of different atoms in the periodic table of elements, in particular the fact that atoms have a shell structure with different numbers of electrons occupying the s, p, d and f shells. Consequently there are two classes of electronic states in solids; those involving core states which are localized and act like single atoms and also valence states which are delocalized and generally result in a spread of electrons over the material. These are characterized by Bloch waves and account for the binding properties of the material and involve principally the outer shells of the atom. Therefore the problem arises when seeking to describe these contrasting states with a single basis set.

Moreover, the effective potential of a given material has quite different characteristics close to and far away from the nucleus. Close to the nucleus the potential has deep Coulomb like wells that represent the 1/r strong repulsion close to the nucleus. In the interstitial region between atoms and far from the centre of the nucleus, the effective potential is described by smooth, flat potentials. A general approximation is taken to overcome this problem called the pseudo-potential approximation where both the wavefunction and the effective potential are replaced by smoother functions which match the originals at a given cut-off radius. The properties of this approximation will be discussed in the following section.

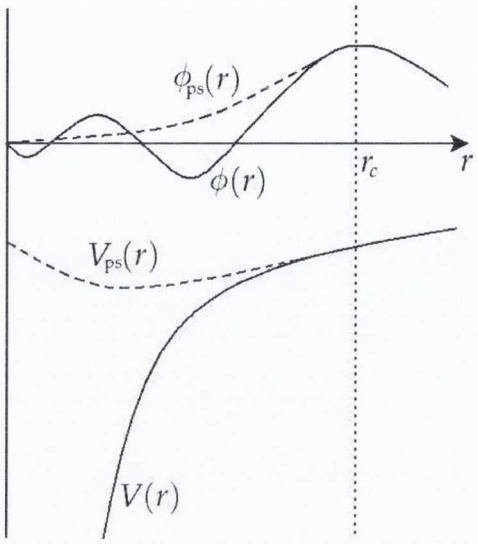

Figure 2.1: Representation of the pseudo wave function and pseudo-potential. The pseudo functions match those of the exact all electron functions at a given cut-off radius r_c

2.5 Pseudo-potentials

Most chemical, electronic and structural properties of materials are governed by the interstitial region between nuclei which contain the outermost "valence" electrons. The energy of the inner or "core" electrons is usually much lower and therefore will not take part in bond formation or electrical conduction. These "core" states can then be omitted from the entire self-consistent DFT calculation. The pseudo-potential approximation involves removing the core electrons and the nuclear potential and replacing them by a weaker effective potential called a "pseudo-potential" [79, 93]. This pseudo-potential acts on a set of pseudo wave functions rather than on the true valence wave functions. The resulting pseudo wave functions can be constructed to behave smoothly in the core region which improves efficiency by ensuring that only a small number of plane waves are needed to represent it. The pseudo wave function is constructed so as to match the exact valence wave function beyond a certain cutoff radius r_c, as seen in Fig. 2.1.

It is also important to preserve the scattering properties of the atomic orbitals when constructing a smooth pseudo wave function. These are different depending on the angular momentum channel l and therefore the resulting pseudo-potential is also dependent on l.

The Phillips Kleinman construction of pseudo-potential is the general method used in most pseudo-potential generation schemes [94]. It exploits the fact that strong oscillations of valence wavefunctions in the core region result in non-orthogonality between valence (v) and core (c) functions. In this sense a pseudo valence wave function can be defined such that a non-zero overlap between different core states exists i.e.

$$|\phi_v\rangle_{\rm ps} = |\phi_v\rangle + \sum_c \alpha_{cv}|\phi_c\rangle, \tag{2.38}$$

where $\alpha_{cv} = \langle\phi_c|\phi_v\rangle_{\rm ps} \neq 0$. With this definition the new smooth pseudo wavefunction is the eigenfunction of a pseudo-Hamiltonian with the same eigenvalues as the original valence wavefunction

$$\begin{aligned} &\Big[H + \sum_c (\varepsilon_v - \varepsilon_c)|\phi_c\rangle\langle\phi_c|\Big]|\phi_v\rangle_{\rm ps} = \varepsilon_v|\phi_v\rangle_{\rm ps}, \\ &\rightarrow H_{\rm ps}|\phi_v\rangle_{\rm ps} = \varepsilon_v|\phi_v\rangle_{\rm ps}. \end{aligned} \tag{2.39}$$

Therefore an energy and angular momentum dependent pseudo-potential exists with an extra non-zero term in the core region

$$V_{\rm ps} = V_0 + \sum_c (\varepsilon_v - \varepsilon_c)|\phi_c\rangle\langle\phi_c|, \tag{2.40}$$

where the new pseudo wavefunction has a different norm and resultantly a different charge than the original valence potential. As a result this scheme must be generalized to conserve the norm of the pseudo-potential. This is achieved by constructing an energy independent pseudo-potential that also depends on the angular momentum quantum number l. This pseudo-potential is then transferable to other systems. The new pseudo-potential is

expressed as

$$V_{\rm ps} = \sum_{lm} v^l_{\rm ps}(r)|lm\rangle\langle lm| = \\ = v^{loc}_{\rm ps}(r) + \sum_{l=0}^{l_{\rm max}} \Delta v^l_{\rm ps}(r) P_l, \tag{2.41}$$

where the sum rule has been invoked and $l_{\rm max}$ is the highest l component in the core region. The pseudo-potential is now broken into a local and non-local part up to and including $l_{\rm max}$. In order to construct a good pseudo-potential one must ensure both softness (so that the wavefunction can be expanded in a small number of plane waves) and transferability (that it remains accurate even when describing electronic configurations different from what it has been designed from).

With all this at hand the following steps are taken to generate an optimal pseudo-potential:

- The exact all-electron wavefunctions for a suitable atomic reference configuration is calculated. This is generally the ground state configuration of a given atom i.e. for Si: $3s^2\ 3p^2$.

- A smooth pseudo wave function is constructed that matches the all-electron wave-function beyond a suitably chosen cut-off radius r_c, ensuring also that the pseudo wave function is node-less. The added criteria are that that the pseudo wave function matches the all-electron wave function beyond r_c with continuous derivative. Furthermore the norm is conserved for both i.e. one has the condition

$$\int_0^{r_c} dr r^2 [\phi^l_{\rm ps}(r)]^2 = \int_0^{r_c} dr r^2 [\phi^l_{\rm ae}(r)]^2. \tag{2.42}$$

  This ensures better transferability.

- The pseudopotential is calculated by inverting the radial Schrödinger equation

At this point almost all the necessary tools for ab initio studies on large scale systems have been described. The final correction, called the spin-orbit correction, is also important in this thesis since the systems that are dealt with include localized spins which exhibit large magnetic anisotropies due mainly to the spin-orbit interaction. This correction will be discussed in the final section.

2.6 Spin-orbit correction: onsite approximation

The spin-orbit interaction is a relativistic effect, which increases in magnitude as Z^4 for central spherical potentials, where Z is the atomic number. Therefore, for transition metal magnetic systems, such as those considered in this work, the effect becomes pronounced. Such magnetic atoms, when placed on a non-magnetic substrate, can exhibit large easy-axis and hard-axis anisotropies, due mostly to the spin-orbit interaction, an important quantity which determines the local spin-relaxation time. It is therefore apparent that an efficient implementation of the spin-orbit interaction must be developed within DFT and the pseudo-potential method. This is briefly outlined below.

Kleinman and Bylander have shown how the generation of non-relativistic pseudo-potentials can be extended to account for relativistic effects [95, 96]. This is achieved by solving the all-electron Dirac equation for a single atom. From this a pseudo-potential can be extracted. This now depends on the total angular momentum $j = l \pm 1/2$. The pseudo-potential can be written as

$$V = \sum_{j,m_j} |j, m_j\rangle V_j \langle j, m_j|, \tag{2.43}$$

and includes all relativistic corrections up to order α^2, where α is the fine structure constant and $|j, m_j\rangle$ are the total angular momentum states. The expression in Eq. (2.43) can be recast in terms of the more familiar angular momentum and spin quantum

numbers l and m [97]

$$V_{\sigma,\sigma'} = V^{\mathrm{sc}}_{\sigma,\sigma'} + V^{\mathrm{SO}}_{\sigma,\sigma'} = \sum_{l,m} [\tilde{V}_l I_{\sigma,\sigma'} + \tilde{V}_l^{\mathrm{SO}} \mathbf{L}.\mathbf{S}_{\sigma,\sigma'}] |l,m\rangle\langle l,m|, \tag{2.44}$$

where

$$\begin{aligned} \tilde{V}_l &= \frac{1}{2l+1}[(l+1)V_{l+1/2} + V_{l-1/2}], \\ \tilde{V}_l^{\mathrm{SO}} &= \frac{2}{2l+1}[V_{l+1/2} - V_{l-1/2}]. \end{aligned} \tag{2.45}$$

Here $\tilde{V}_l$ represents the scalar part of the pseudo-potential containing the non-relativistic pseudo-potential and also the scalar relativistic corrections. $\tilde{V}_l^{\mathrm{SO}}$ is the relativistic spin-orbit correction. At this point, the spin-orbit corrected Kohn-Sham Hamiltonian now looks like

$$H_{\sigma,\sigma'} = T_{\sigma,\sigma'} + V^{\mathrm{sc}}_{\sigma,\sigma'} + V^{\mathrm{SO}}_{\sigma,\sigma'} + V^{\mathrm{H}} + V^{\mathrm{xc}}_{\sigma,\sigma'}, \tag{2.46}$$

where the non-diagonal elements of the Hamiltonian originate from the spin-orbit potential but also from the exchange and correlation potential, whenever the system exhibits a non-collinear spin. The first term is the kinetic energy contribution, the second and third are the scalar and spin-orbit contributions to the energy respectively and the fourth and fifth are the Hartree and exchange correlational energies.

This Hamiltonian can then be diagonalized with the preferred basis set in order to determine the total energy of the system. Anisotropy parameters for a given magnetic ion deposited on a substrate can be determined from the difference between the total energy calculated by aligning the atom magnetic moment along the x, y or z-axes.

Chapter 3

Zero Temperature Green's Function Formalism

This chapter deals with the procedure used when dealing with a system that experiences a perturbation. This will be treated as a general perturbation V and could represent the interaction of an electronic system with an external field, with a phonon or, as introduced in the previous section, the exchange interaction with a localized impurity. In particular for problems of this nature that cannot be solved exactly, the Green's function formalism is generally employed to treat the problem perturbatively. The starting point is a Hamiltonian which comprises an unperturbed part H_0 (this can be solved exactly) and the perturbation V (unspecified for the moment). The initial non-interacting system is completely described by H_0 and the effects of V are assumed small to ensure convergence of the perturbation expansion. At this point the operators used in this scheme must be transformed to take into account the interaction term. All the analysis will be performed at zero-temperature for simplicity (this approximation is accurate when dealing with low temperatures <1K) and with the help of reference [98].

3.1 Interaction representation

The interaction representation must be used when dealing with a perturbation to a system. In this representation it is assumed that both operators, O, and wavefunctions, ψ, have a time dependence, contrary to the Heisenberg and Schrödinger representations. The Hamiltonian can then be separated into two parts where the commutation relation $[H_0, V] \neq 0$ holds. The following quantities are defined

$$H = H_0 + V, \tag{3.1}$$

$$\hat{O}(t) = e^{iH_0 t} O e^{-iH_0 t}, \tag{3.2}$$

$$\hat{\psi}(t) = \hat{U}(t)\psi(0), \tag{3.3}$$

where the unitary operator $\hat{U}(t) = e^{iH_0 t}e^{-iHt}$ is introduced and the symbol $\hat{}$ indicates that one is in the interaction representation. This choice of operators ensures that the time dependence of the wavefunctions is governed by the interaction $\hat{V}(t)$

$$\frac{\partial}{\partial t}\hat{\psi}(t) = -i\hat{V}(t)\hat{\psi}(t). \tag{3.4}$$

The unitary operator also obeys the differential equation:

$$\frac{\partial}{\partial t}\hat{U}(t) = -i\hat{V}(t)\hat{U}(t), \tag{3.5}$$

and with the initial condition $\hat{U}(0) = 1$ has the formal solution

$$\hat{U}(t) = \sum_{n=0}^{\infty}(-i)^n \int_0^t dt_1 \int_0^{t_1} dt_2 \ldots \int_0^{t_{n-1}} dt_n \hat{V}(t_1)\hat{V}(t_2)\ldots\hat{V}(t_n). \tag{3.6}$$

After introducing the time ordering operator T, which arranges operators in order of decreasing time from left to right, and after having redefined the time integration variables,

one arrives at the following expression for the unitarity operator

$$\hat{U}(t) = 1 + \sum_{n=1}^{\infty} \frac{(-i)^n}{n!} \int_0^t dt_1 \int_0^t dt_2 \ldots \int_0^t dt_n T[\hat{V}(t_1)\hat{V}(t_2)\ldots\hat{V}(t_n)], \tag{3.7}$$

$$\hat{U}(t) = T\exp\Big[-i\int_0^t dt_1 \hat{V}(t_1)\Big]. \tag{3.8}$$

In addition to the unitary operator the S matrix must also be defined. This is the operator which propagates the wave function $\hat{\psi}(t)$ from time t to the time t'

$$\hat{\psi}(t) = \hat{S}(t,t')\hat{\psi}(t'). \tag{3.9}$$

The S-matrix also satisfies the differential equation

$$\frac{\partial}{\partial t}\hat{S}(t,t') = -i\hat{V}(t)S(t,t'), \tag{3.10}$$

with solution

$$\hat{S}(t,t') = T\exp\Big[-i\int_{t'}^t dt_1 \hat{V}(t_1)\Big]. \tag{3.11}$$

The S-matrix is important when dealing with the ground state of the full interacting Hamiltonian, for which one has no information. The ground-state wave-function of the unperturbed system (denoted by $\hat{\phi}_0$), however, can be found exactly. It can be shown [99] that the relation between the ground states of the interacting and non-interacting systems can be defined as

$$\hat{\psi}(0) = \hat{S}(0,-\infty)\hat{\phi}_0, \tag{3.12}$$

so that $\hat{\psi}(-\infty) = \hat{\phi}_0$. This indicates that at $t = -\infty$ the system is in the non-interacting ground-state, $\hat{\phi}_0$. The operator $\hat{S}(0, -\infty)$ then propagates adiabatically the wave-function up to the present ($t = 0$), following the evolution dictated by the interaction potential $\hat{V}$.

3.2 Green's function formalism

One is now in the position to introduce the Green's function formalism to treat the system perturbation. At zero temperature the electron Green's function, G, is defined as

$$G_{\lambda,\lambda'}(t,t') = -i\langle|Tc_\lambda(t)c^\dagger_{\lambda'}(t')|\rangle, \tag{3.13}$$

where $|\rangle$ is the ground state of the full Hamiltonian, H. The c's are the electron creation ($c^\dagger$) and annihilation (c) operators with the indexes λ labeling the eigenstates of the Hamiltonian, $H = \sum_\lambda \varepsilon_\lambda c^\dagger_\lambda c_\lambda$, with eigenvalues ε_λ. In order to convert this expression from the Heisenberg to the interaction representation the S-matrix from the previous section, Eq. (3.12), is used which gives

$$G_{\lambda,\lambda'}(t,t') = \frac{-i_0\langle|T\hat{c}_\lambda(t)\hat{c}^\dagger_{\lambda'}(t')S(\infty,-\infty)|\rangle_0}{{}_0\langle|S(\infty,-\infty)|\rangle_0}. \tag{3.14}$$

In Eq. (3.14) the Green function is the expectation value of an operator calculated over the non-interacting ground state $|\rangle_0$, where the operators $\hat{c}$ and $\hat{c}^\dagger$ are now written in the interaction representation. By using the S-matrix expansion provided in Eq. (3.11) one arrives at the final expression for the fully interacting Green's function, which reads

$$G_{\lambda,\lambda'}(t,t') = \sum_{n=0} \frac{(-i)^{n+1}}{n!} \int_{-\infty}^{\infty} dt_1 \ldots \int_{-\infty}^{\infty} dt_n \frac{{}_0\langle|T\hat{V}(t_1)\ldots\hat{V}(t_n)\hat{c}_\lambda(t)\hat{c}^\dagger_{\lambda'}(t')|\rangle_0}{{}_0\langle|S(\infty,-\infty)|\rangle_0}. \tag{3.15}$$

At this point the formalism encounters a problem. In fact, although the ground state of the system at $t = -\infty$ is well defined [from Eq. (3.12)], there is now no means of describing

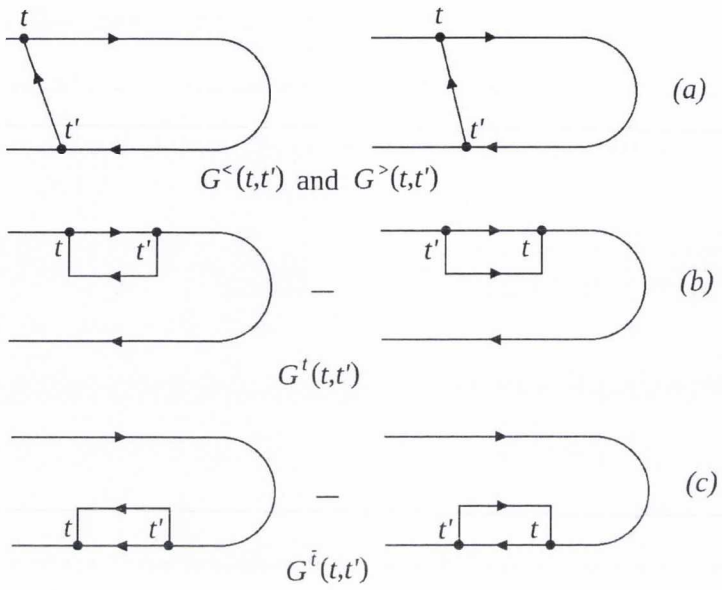

Figure 3.1: Feynman rules for non-equilibrium Green's functions calculated over the contour running from $-\infty$ to $-\infty$. The four configurations are the lesser and greater Green's functions (a) and the time-ordered (b) and time-anti-ordered (c) Green's functions.

the ground state at the time $t = +\infty$. This problem was overcome by Schwinger [100], who proposed to write the time integral in the S-matrix in terms of two contributions, one that evolves from $(-\infty, \tau)$ and the other from $(\tau, -\infty)$. This process ensures that eventually τ will reach $+\infty$. The advantage of this idea is that the integration begins and ends with a known ground state $\hat{\psi}(-\infty) = \hat{\phi}_0$. This is called the *time loop method* and it is the primary way to deal with non-equilibrium systems. Therefore, the formalism is adjusted accordingly. The S-matrix then becomes

$$\hat{S}(-\infty, -\infty) = T_C \exp\Big[-i \int_C d\tau_1 \hat{V}(\tau_1) \Big], \tag{3.16}$$

where the time-loop contour C has been defined as the one that runs over the time intervals $(-\infty, \tau_1)$ and then $(\tau_1, -\infty)$, and the operator T_C as the time-ordering operator

along the entire loop. The full Green's function expansion finally becomes

$$G_{\lambda,\lambda'}(\tau,\tau') = \sum_{n=0} \frac{(-i)^{n+1}}{n!} \int_C d\tau_1 \dots \int_C d\tau_n \frac{{}_0\langle|T_C \hat{V}(\tau_1)\dots\hat{V}(\tau_n)\hat{c}_\lambda(\tau)\hat{c}^\dagger_{\lambda'}(\tau')|\rangle_0}{{}_0\langle|\hat{S}(-\infty,-\infty)|\rangle_0}. \quad (3.17)$$

Although the introduction of the C contour solves the issue of the $t = +\infty$ limit, it also brings the drawback of introducing six new Green's functions, depending on how the times t and t' are positioned over the loop contour. These are schematically represented in Fig. 3.1. In the Heisenberg representation for operators such Green's functions are written as

$$G^<_{\lambda,\lambda'}(t,t') = i\langle|c^\dagger_{\lambda'}(t')c_\lambda(t)|\rangle, \quad (3.18)$$

$$G^>_{\lambda,\lambda'}(t,t') = -i\langle|c_\lambda(t)c^\dagger_{\lambda'}(t')|\rangle, \quad (3.19)$$

$$G^t_{\lambda,\lambda'}(t,t') = \theta(t-t')G^>_{\lambda,\lambda'}(t,t') + \theta(t'-t)G^<_{\lambda,\lambda'}(t,t'), \quad (3.20)$$

$$G^{\bar{t}}_{\lambda,\lambda'}(t,t') = \theta(t'-t)G^>_{\lambda,\lambda'}(t,t') + \theta(t-t')G^<_{\lambda,\lambda'}(t,t'), \quad (3.21)$$

$$G^{\text{ret}}_{\lambda,\lambda'}(t,t') = G^t_{\lambda,\lambda'}(t,t') - G^<_{\lambda,\lambda'}(t,t'), \quad (3.22)$$

$$G^{\text{adv}}_{\lambda,\lambda'}(t,t') = G^t_{\lambda,\lambda'}(t,t') - G^>_{\lambda,\lambda'}(t,t'). \quad (3.23)$$

Here $G^<$ and $G^>$ are respectively the lesser and greater Green's functions, G^t and $G^{\bar{t}}$ are the time-ordered and time-anti-ordered Green's functions and G^{r} and G^{a} are retarded and advanced ones. More information about the properties of these six Green's functions can be obtained by considering the unperturbed Hamiltonian, i.e. by looking at the non-interacting case, which can be solved exactly. After diagonalization the unperturbed Hamiltonian takes the form $H_0 = \sum_\lambda \varepsilon_\lambda c^\dagger_\lambda c_\lambda$, where ε_λ are the eigenvalues. The Green's functions are then evaluated over the known ground state $|\rangle_{\lambda=0}$, whose energy is ε_0. In this case, the explicit time dependence of the creation and annihilation operators can be

found from the Heisenberg equation. For instance the one for the annihilation operator is

$$\frac{\partial}{\partial t}c_\lambda(t) = -i[H_0, c_\lambda(t)], \tag{3.24}$$

which has solution (the initial condition is $c_\lambda(0) = c_\lambda$)

$$c_\lambda(t) = c_\lambda \exp(-i\varepsilon_\lambda t). \tag{3.25}$$

Likewise, the solution for the creation operator $c_\lambda^\dagger(t)$ is

$$c_\lambda^\dagger(t) = c_\lambda^\dagger \exp(+i\varepsilon_\lambda t). \tag{3.26}$$

If one now inserts such solutions into the expressions for the lesser and greater Green's functions provided by Eqs. (3.18) and (3.19), these can be written as

$$G^<_{\lambda,\lambda'}(t,t') = i\delta_{\lambda,\lambda'}(1 - \langle n_\lambda \rangle)\exp[-i\varepsilon_\lambda(t-t')], \tag{3.27}$$

$$G^>_{\lambda,\lambda'}(t,t') = -i\delta_{\lambda,\lambda'}\langle n_\lambda \rangle \exp[-i\varepsilon_\lambda(t-t')], \tag{3.28}$$

where the expectation value over the contour of the electron number operator, $n_\lambda = c_\lambda^\dagger c_\lambda$, has been introduced and the fermion anti-commutation relations have been used. It is notable that at thermal equilibrium the number operator average is given by the Fermi-Dirac distribution $\langle n_\lambda \rangle = f(\varepsilon_\lambda) = 1/[\exp(\beta\varepsilon_\lambda) + 1]$, with Fermi energy ε_F, and $\beta = 1/(k_\mathrm{B}T)$ with k_B being the Boltzmann constant. By using these relations the full energy resolved dependence of all the six Green's functions can be constructed. This is obtained

by Fourier transform of their time-dependent counterparts

$$G^{<}(\lambda,\omega) = 2\pi i f(\varepsilon_\lambda)\delta(\omega-\varepsilon_\lambda), \tag{3.29}$$

$$G^{>}(\lambda,\omega) = -2\pi i[1-f(\varepsilon_\lambda)]\delta(\omega-\varepsilon_\lambda), \tag{3.30}$$

$$G^{t}(\lambda,\omega) = \frac{1}{\omega-\varepsilon_\lambda+i\eta_\lambda}, \tag{3.31}$$

$$G^{\bar{t}}(\lambda,\omega) = \frac{-1}{\omega-\varepsilon_\lambda-i\eta_\lambda}, \tag{3.32}$$

$$G^{\mathrm{ret}}(\lambda,\omega) = \frac{1}{\omega-\varepsilon_\lambda+i\eta}, \tag{3.33}$$

$$G^{\mathrm{adv}}(\lambda,\omega) = \frac{1}{\omega-\varepsilon_\lambda-i\eta}, \tag{3.34}$$

where η is a positive and satisfies $\eta \to 0^+$, while η_λ is positive for $\varepsilon_\lambda > \varepsilon_{\mathrm{F}}$ and negative for $\varepsilon_\lambda < \varepsilon_{\mathrm{F}}$.

3.3 Wick's theorem

In order to tackle the interacting problem one needs to return to Eq. (3.17) and ascertain the rules, which determine the contour time ordering of the product of the $\hat{V}(\tau)$ operators. These are different depending on whether the $\hat{V}$'s describe electrons, phonons or, as in this case, spins. Assuming that the perturbation is electronic in nature (for instance a density-density operator representing Coulomb repulsion), one then needs to deal with time ordering products of the form

$$G_{\lambda,\lambda'}(\tau,\tau') = \sum_{n=0}\frac{(-i)^{n+1}}{n!}\int_C d\tau_1\ldots\int_C d\tau_n \frac{{}_0\langle|T_C\hat{V}(\tau_1)\ldots\hat{V}(\tau_n)\hat{c}_\lambda(\tau)\hat{c}^\dagger_{\lambda'}(\tau')|\rangle_0}{{}_0\langle|S(-\infty,-\infty)|\rangle_0}, \tag{3.35}$$

where there is always an equal number of creation and annihilation operators and an operator that creates a state is always followed by an operator that destroys one. In this case, the task is that of re-expressing Eq. (3.35) in terms of products of time ordered pairs ${}_0\langle|T_C\{\hat{c}_\lambda(\tau)\hat{c}^\dagger_{\lambda'}(\tau')\}|\rangle_0$. Clearly, as there are λ pairs of operators, there are $\lambda!$ different

possible orderings for such pairs. Using Wick's theorem, which is extensively described in ref. [101], there are three simple rules that can be gleaned for ordering the operators.

1. There is a sign change whenever two neighbouring Fermi operators are interchanged. Therefore the number of interchanges must be noted.

2. If there are a mixture of particles in the time-ordering bracket, i.e. if there exists operators that do not commute, these can be separated into different time-ordering brackets.

3. We recognize the time ordering of a product of operators with different time arguments as the unperturbed Green's function, namely

$$ {}_0\langle|T_C\left\{\hat{c}_\lambda(\tau)\hat{c}^\dagger_{\lambda'}(\tau')\right\}|\rangle_0 = iG_{0,\lambda,\lambda'}(\tau,\tau')\,. \tag{3.36}$$

These rules will be implemented when performing the full time-ordering of the interaction Hamiltonian, which will be introduced later in the chapter. This will show Wick's theorem in action.

3.4 Langreth's theorem and Dyson's equation

Wick's theorem essentially allow the expansion of the fully interacting Green's function in terms of the non-interacting Green's functions up to a given order, n. This can be generalized at any order, $n = \infty$, by *Dyson's equation*. Dyson's equation is a reformulation of the general perturbation expansion of the full interacting Green's function of Eq. (3.14) in terms of a quantity called the *self-energy*. This quantity in itself can be evaluated perturbatively and provides a compact way to describe the effect of a perturbation on a

physical (non-interacting) system. Dyson's equation takes the form

$$G(\tau,\tau') = G_0(\tau,\tau') + \int_C d\tau_1 \int_C d\tau_2 G_0(\tau,\tau_1)\Sigma(\tau_1,\tau_2)G(\tau_2,\tau'), \tag{3.37}$$

where G_0 is the unperturbed Green's function and Σ is the self-energy. In order to find the real time components of this relation the reader should refer to Haug and Jauho [102], who describe Langreth's theorem for the evaluation of "contour-convolutions" as the one written above. It can be shown that the retarded/advanced and the lesser/greater components of the Green's function are respectively

$$G^{\mathrm{r(a)}}(\tau,\tau') = G_0^{\mathrm{r(a)}}(\tau,\tau') + \int_C d\tau_1 \int_C d\tau_2 G_0^{\mathrm{r(a)}}(\tau,\tau_1)\Sigma^{\mathrm{r(a)}}(\tau_1,\tau_2)G^{\mathrm{r(a)}}(\tau_2,\tau'), \tag{3.38}$$

$$G^{\lessgtr}(\tau,\tau') = G_0(\tau,\tau') + \int_C d\tau_1 \int_C d\tau_2 G^{\mathrm{r}}(\tau,\tau_1)\Sigma^{\lessgtr}(\tau_1,\tau_2)G^{\mathrm{a}}(\tau_2,\tau')\,, \tag{3.39}$$

whose energy resolved components can be calculated by Fourier transform

$$G^{\mathrm{r(a)}}(\omega) = G_0^{\mathrm{r(a)}}(\omega) + G_0^{\mathrm{r(a)}}(\omega)\Sigma^{\mathrm{r(a)}}(\omega)G^{\mathrm{r(a)}}(\omega), \tag{3.40}$$

$$G^{\lessgtr}(\omega) = G_0(\omega) + G^{\mathrm{r}}(\omega)\Sigma^{\lessgtr}(\omega)G^{\mathrm{a}}(\omega)\,. \tag{3.41}$$

3.5 General expression for the current through an interacting region

The power of the Green's function formalism will be demonstrated by describing the perturbation to a close system originating from the coupling to two semi-infinite leads. This is a problem that can be solved exactly within the approximations that will be introduced. Such an approach coincides with the widely used non-equilibrium Green's function (NEGF) method, which has been extensively used in the literature [44, 45, 46] to describe the electron transport problem. Here it will be discussed how to construct

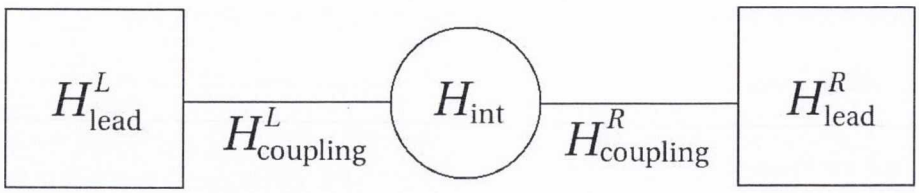

Figure 3.2: Schematic of the transport device containing two decoupled leads connected to a central region, which contains information on the interactions in the system

a transport theory starting from the Green's functions that have been covered in the previous sections. At this point a specific Hamiltonian that describes an interacting region sandwiched between M semi-infinite, non-interacting leads is introduced. This has the form

$$H = H_{\text{int}}(\{c^\dagger_\lambda; c_\lambda\}) + \sum_i^M H^i_{\text{lead}} + \sum_i^M H^i_{\text{coupling}}, \tag{3.42}$$

$$H^i_{\text{lead}} = \sum_\alpha \varepsilon_{\alpha i} b^\dagger_{\alpha i} b_{\alpha i}, \tag{3.43}$$

$$H^i_{\text{coupling}} = \sum_{\alpha,\lambda} \left(V_{\alpha i,\lambda} b^\dagger_{\alpha i} c_\lambda + \text{h.c.} \right), \tag{3.44}$$

Here H^i_{lead} is the Hamiltonian of the i-th lead with $b^\dagger_{\alpha i}(b_{\alpha i})$ creating (destroying) electrons at the energy $\varepsilon_{\alpha i}$, while $H_{\text{int}}(\{c^\dagger_\lambda; c_\lambda\})$ describes the interacting region and it is constructed with the creation and annihilation operators $c^\dagger_\lambda$ and c_λ (they form an orthonormal set). Finally H^i_{coupling} couples the i-th leads with the interacting region, through the hopping matrix elements $V_{\alpha i,\lambda}$. Initially it is assumed that the leads are completely decoupled from the scattering region, i.e. that $V_{\alpha i,\lambda} = 0$ for every i. One can then define the number operator in each of the leads as $\hat{n}^i = \sum_\alpha b^\dagger_{\alpha i} b_{\alpha i}$. The rate of change of the expectation value of this operator gives the current, I^i, flowing into the interacting region from the i-th lead. This is simply

$$I^i = -\frac{\partial}{\partial t}\langle n^i \rangle = -i\langle [H, n^i] \rangle = i \sum_{\alpha,\lambda} \left[V_{\alpha i,\lambda} \langle b^\dagger_{\alpha i} c_\lambda \rangle(t) - V^*_{\alpha i,\lambda} \langle c^\dagger_\lambda b_{\alpha i} \rangle(t) \right]. \tag{3.45}$$

Clearly, one can now recast Eq. (3.45) in terms of the Green's functions introduced before. In this particular case one can define the *hybrid* real-time Green's functions describing the overlap between the i-th lead and the interacting region as

$$G^{<}_{\lambda,\alpha i}(t,t') = i\langle b^{\dagger}_{\alpha i}(t)c_{\lambda}(t')\rangle, \tag{3.46}$$

$$G^{<}_{\alpha i,\lambda}(t,t') = i\langle c^{\dagger}_{\lambda}(t)b_{\alpha i}(t')\rangle, \tag{3.47}$$

so that the current can be written as

$$\begin{aligned} I^{i} &= \sum_{\alpha,\lambda}\Big[V_{\alpha i,\lambda}G^{<}_{\lambda,\alpha i}(t,t) - V^{*}_{\alpha i,\lambda}G^{<}_{\alpha i,\lambda}(t,t)\Big], \\ &= \int_{-\infty}^{\infty}\frac{d\omega}{2\pi}\sum_{\alpha,\lambda}\Big[V_{\alpha i,\lambda}G^{<}_{\lambda,\alpha i}(\omega) - V^{*}_{\alpha i,\lambda}G^{<}_{\alpha i,\lambda}(\omega)\Big]. \end{aligned} \tag{3.48}$$

At this point there is still no expression for the lesser *hybrid* Green's functions. Therefore, in order to proceed, one must define the following contour ordered Green's functions

$$G_{\lambda,\alpha i}(\tau,\tau') = -i\langle T_C\{c_{\lambda}(\tau)b^{\dagger}_{\alpha i}(\tau')\}\rangle, \tag{3.49}$$

$$G_{\alpha i,\lambda}(\tau,\tau') = -i\langle T_C\{b_{\alpha i}(\tau)c^{\dagger}_{\lambda}(\tau')\}\rangle, \tag{3.50}$$

$$G_{\lambda,\lambda'}(\tau,\tau') = -i\langle T_C\{c_{\lambda}(\tau)c^{\dagger}_{\lambda'}(\tau')\}\rangle, \tag{3.51}$$

$$G_{\alpha i,\alpha i}(\tau,\tau') = -i\langle T_C\{b_{\alpha i}(\tau)b^{\dagger}_{\alpha i}(\tau')\}\rangle. \tag{3.52}$$

Finally, by using the Dyson equation, the following expressions for $G_{\lambda,\alpha i}$ and $G_{\alpha i,\lambda}$ are obtained, in which the coupling between the interacting region and the leads appears explicitly

$$G_{\lambda,\alpha i}(\tau,\tau') = \sum_{\lambda'}\int_{C} d\tau_1 G_{\lambda,\lambda'}(\tau,\tau_1)V^{*}_{\alpha i,\lambda'}G_{\alpha i,\alpha i}(\tau_1,\tau'), \tag{3.53}$$

$$G_{\lambda,\alpha i}(\tau,\tau') = \sum_{\lambda'}\int_{C} d\tau_1 G_{\alpha i,\alpha i}(\tau,\tau_1)V_{\alpha i,\lambda'}G_{\lambda',\lambda}(\tau_1,\tau'). \tag{3.54}$$

Now, by following the contour integration rules and by using the relations defined in Eqs. (3.19) to (3.23) one arrives at the following real time expression for the hybrid Green's functions

$$G^{<}_{\lambda,\alpha i}(t,t') = \sum_{\lambda'} V^{*}_{\alpha i,\lambda'} \int_{-\infty}^{\infty} dt_1 \Big[G^{r}_{\lambda,\lambda'}(t,t_1) G^{<}_{\alpha i,\alpha i}(t_1,t') + G^{<}_{\lambda,\lambda'}(t,t_1) G^{a}_{\alpha i,\alpha i}(t_1,t') \Big], \quad (3.55)$$

$$G^{<}_{\alpha i,\lambda}(t,t') = \sum_{\lambda'} V_{\alpha i,\lambda'} \int_{-\infty}^{\infty} dt_1 \Big[G^{r}_{\alpha i,\alpha i}(t,t_1) G^{<}_{\lambda,\lambda'}(t_1,t') + G^{<}_{\alpha i,\alpha i}(t,t_1) G^{a}_{\lambda,\lambda'}(t_1,t') \Big], \quad (3.56)$$

which after Fourier transform becomes

$$G^{<}_{\lambda,\alpha i}(\omega) = \sum_{\lambda'} V^{*}_{\alpha i,\lambda'} \Big[G^{r}_{\lambda,\lambda'}(\omega) G^{<}_{\alpha i,\alpha i}(\omega) + G^{<}_{\lambda,\lambda'}(\omega) G^{a}_{\alpha i,\alpha i}(\omega) \Big], \quad (3.57)$$

$$G^{<}_{\alpha i,\lambda}(\omega) = \sum_{\lambda'} V_{\alpha i,\lambda'} \Big[G^{r}_{\alpha i.\alpha i}(\omega) G^{<}_{\lambda,\lambda'}(\omega) + G^{<}_{\alpha i,\alpha i}(\omega) G^{a}_{\lambda,\lambda'}(\omega) \Big]. \quad (3.58)$$

Finally the expression for the current can now be written as

$$\begin{aligned} I^{i} &= \int_{-\infty}^{\infty} \frac{d\omega}{2\pi} \sum_{\alpha,\lambda,\lambda'} V^{*}_{\alpha i,\lambda} V_{\alpha i,\lambda'} \Big[G^{<}_{\alpha i,\alpha i}(\omega) G^{>}_{\lambda,\lambda'}(\omega) - G^{>}_{\alpha i,\alpha i}(\omega) G^{<}_{\lambda,\lambda'}(\omega) \Big] = \\ &= \int_{-\infty}^{\infty} \frac{d\omega}{2\pi} \sum_{\lambda,\lambda'} \Big[\Sigma^{i,<}_{\lambda,\lambda'}(\omega) G^{>}_{\lambda,\lambda'}(\omega) - \Sigma^{i,>}_{\lambda,\lambda'}(\omega) G^{<}_{\lambda,\lambda'}(\omega) \Big] = \\ &= \int_{-\infty}^{\infty} \frac{d\omega}{2\pi} \mathrm{Tr} \Big\{ [\Sigma^{i,<}(\omega)][G^{>}(\omega)] - [\Sigma^{i,>}(\omega)][G^{<}(\omega)] \Big\}, \end{aligned} \quad (3.59)$$

where the square brackets denote the matrix form of the operator describing the interacting region. In the same equation the lesser and greater parts of the self-energy have been defined in the same region as

$$\Sigma^{i,\lessgtr}_{\lambda,\lambda'}(\omega) = \sum_{\alpha} V^{*}_{\alpha i,\lambda} G^{\lessgtr}_{\alpha i,\alpha i}(\omega) V_{\alpha i,\lambda'}. \quad (3.60)$$

These represent the rates at which a particle with energy ω leaves ($<$) or enter ($>$) the i-th lead. Equation (3.59) provides a rather transparent interpretation for the current,

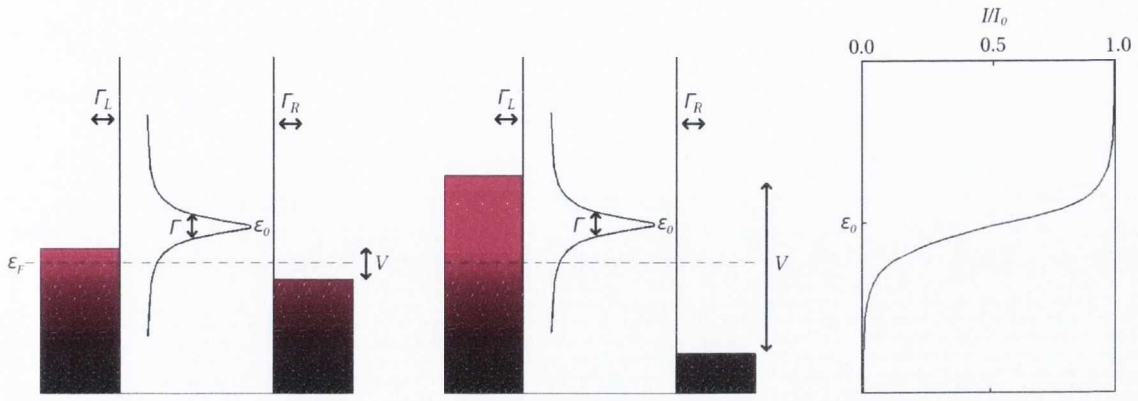

Figure 3.3: Schematic representation of resonant tunneling through a single onsite level when (a) the bias window is just below the level and (b) the bias window includes the level. The current vs voltage profile is for the process is shown in (c) where the current is calculated in units of the saturation current $I_0 = 2\Gamma_L\Gamma_R/\Gamma$

which is nothing but the difference between the in-scattering rate and the out-scattering one to and from the scattering region.

3.6 Current through single non-interacting level

As an illustration of the method developed so far the simple case of a non-interacting region consisting of a single level with energy ε_0 is considered (note that the index λ is no longer necessary and it has been dropped), whose Hamiltonian is simply

$$H_{\text{int}} = \varepsilon_0 c^\dagger c. \tag{3.61}$$

It is further assumed that the level is coupled to only two semi-infinite, non-interacting leads, respectively to the left, $i = \text{L}$ and to the right, $i = \text{R}$. These are described by a single-orbital tight-binding model with hopping parameter γ_0 and on-site energy $\varepsilon_i = 0$. The self energy associated to each lead is then

$$\Sigma_i^{\lessgtr}(\omega) = \sum_\alpha V_{\alpha i}^* G_{\alpha i,\alpha i}^{\lessgtr}(\omega) V_{\alpha i}. \tag{3.62}$$

As the leads are semi-infinite and under the condition that the density of states of each of the lead, $\rho_i(\varepsilon_\alpha)$, is known, the sum over α can be replaced with an integration over energy

$$\Sigma_i^{\lessgtr}(\omega) = \sum_\alpha \int_{-\infty}^{\infty} d\varepsilon_\alpha \rho_i(\varepsilon_\alpha) V_i^*(\varepsilon_\alpha) G_{\alpha i,\alpha i}^{\lessgtr}(\omega) V_i(\varepsilon_\alpha), \tag{3.63}$$

$$= \begin{cases} i f_i(\omega)\Gamma_i(\omega) \\ -i[1 - f_i(\omega)]\Gamma_i(\omega) \end{cases}, \tag{3.64}$$

where the Green's function derived in Eq. (3.29) has been used for non-interacting fermions. A bias, V, is applied between the left-hand side and the right-hand side lead so that the resulting chemical potential in each lead is shifted by $\mu = eV/2$ (e is the electron charge), namely $\mu_{\mathrm{L}} = \varepsilon_{\mathrm{F}} + \mu$ and $\mu_{\mathrm{R}} = \varepsilon_{\mathrm{F}} - \mu$ (note that each lead in isolation is in equilibrium). Here the Fermi function is defined at the relative chemical potential, namely $f_i(\omega) = 1/[\exp(\frac{\omega - \mu_i}{k_B T}) + 1]$. In the expression for the self-energy, Eq. (3.63), the broadening function $\Gamma_i(\varepsilon_\alpha) = 2\pi\rho_i(\varepsilon_\alpha)|V_i(\varepsilon_\alpha)|^2$ has also been introduced. This gives a finite lifetime to the energy level of the interacting region. Clearly such a broadening (and consequently the lifetime) depends on the strength of the coupling to the leads. It can be shown (see Appendix A) that the broadening function for the single-site, one-dimensional tight-binding model is given by

$$\Gamma_i(\omega) = \frac{2\gamma_i^2}{\gamma_0} \sqrt{1 - \left(\frac{\omega - \varepsilon_0}{2\gamma_0}\right)^2}, \tag{3.65}$$

where γ_i is the hopping from the closest atom in the semi-infinite chain to the interacting region, i.e. there is only a single non-vanishing $V_{i\alpha} = \gamma_i$. In the wide-band limit, $\gamma_0 >> \varepsilon_0$, which is assumed throughout this work, the broadening function becomes a constant $\Gamma_i = 2\gamma_i^2/\gamma_0$. The resulting retarded and advanced self energies in the leads can then be

found from the relation

$$\Sigma_i^{r(a)}(\omega) = \sum_\alpha V_{\alpha i}^* G_{\alpha i,\alpha i}^{r(a)}(\omega) V_{\alpha i}. \tag{3.66}$$

After substitution Eqs. (3.33) and (3.34) the energy integral can be evaluated to obtain

$$\Sigma_i^{r(a)}(\omega) = \pm i\frac{\Gamma_i}{2}. \tag{3.67}$$

The full artillery to calculate the energy-resolved Green's functions for the interacting region is now available, which in turn allows one to access to the current. From advanced and retarded Green's functions defined earlier, one has the following energy resolved relations in terms of the un-perturbed (or unconnected) interacting region (denoted with the subscript 0)

$$\begin{aligned} G^{r(a)}(\omega) &= G_0^{r(a)}(\omega) + G_0^{r(a)}\Sigma^{r(a)}(\omega)G^{r(a)}(\omega), \\ &= \frac{1}{\omega - \varepsilon_0 - \Sigma^{r(a)}}, \end{aligned} \tag{3.68}$$

$$G^{\lessgtr}(\omega) = G^r(\omega)\Sigma^{\lessgtr}(\omega)G^a(\omega), \tag{3.69}$$

where the total self energy is defined as the sum over both contributions coming from the left-hand side and the right-hand side lead $\Sigma(\omega) = \sum_i \Sigma_i(\omega)$. The final expression for the current through a single non-interacting level then takes the form

$$I_i = \int_{-\infty}^{\infty} \frac{d\omega}{2\pi}\Big\{\Sigma_i^<(\omega)G^>(\omega) - \Sigma_i^>(\omega)G^<(\omega)\Big\}, \tag{3.70}$$

$$= \int_{-\infty}^{\infty} d\omega \frac{\Gamma_L\Gamma_R}{\Gamma}\rho(\omega)[f_L(\omega) - f_R(\omega)], \tag{3.71}$$

where the total broadening is $\Gamma = \sum_i \Gamma_i$ and the density of states in the interacting region is $\rho(\omega) = (\Gamma/2\pi)/[(\omega - \varepsilon_0)^2 + \Gamma^2]$. With this expression, the standard result from

scattering theory, namely the Landauer-Büttiker formula [45], has been recovered. In fact the current is simply the product of the transmission coefficient $T(E) = \frac{\Gamma_L \Gamma_R}{2\pi[(\omega-\varepsilon_0)^2+\Gamma^2]}$ and the difference between the Fermi functions of the two leads. In this particular case the transmission coefficient has the form of a Breit-Wigner resonance at the energy level, ε_0. This relation indicates that current will flow only when the energy level is within the bias window. The corresponding current-voltage plot (see Fig. 3.3) presents a characteristic current step when the energy level first enters the bias window. With the convention for the chemical potential in the two leads this happens when $V = 2\varepsilon_0/e$.

Chapter 4

Calculation of the Interacting Spin Self energy

In this chapter the specific interaction between electrons and spins is introduced, upon which a perturbative theory of spin-flip spectroscopy will then be formulated. The theoretical analysis is based on a tight-binding Hamiltonian for the conducting electrons (as in the simple case of Chapter 3), locally exchange coupled to quantum spins. The formulation is then based on the assumption of a separation between the transport electrons and those contributing to form local spins, i.e. it is constructed over the *s-d* model for magnetism [51, 52]. An appropriate self-energy is then constructed for the spin-degrees of freedom up to the second order in the perturbation expansion and this is used in the standard NEGF scheme for transport. The methodology is then applied to describing SF-IETS in atoms and atomic chains and the results are compared with experiments.

4.1 Impurity Spin Models

The spin impurity model that will be used in this thesis stems from the Kondo formalism [103] where an impurity atom at position $\mathbf{x}_n$ immersed in an electron continuum has an associated wavefunction given by $\psi_L(\mathbf{x} - \mathbf{x}_n)$, where L denotes a localized state. The

continuum wavefunctions are defined by $\psi_k(\mathbf{x})$ and can have an overlap between each other. The total many-body wavefunction is the sum of all the possible states of the system.

$$\Psi(\mathbf{x}) = \sum_{\mathbf{k}\sigma} \chi_\sigma \psi_{\mathbf{k}}(\mathbf{x}) c_{\mathbf{k}} + \sum_{\sigma} \chi_\sigma \psi_L(\mathbf{x} - \mathbf{x}_n) c_{L\sigma}, \tag{4.1}$$

where the c's are destruction operators of the given state. The Hamiltonian is as defined in Chapter 1:

$$\begin{aligned} \hat{H} &= \sum_{i=1}^{N_e} \Big[-\frac{\nabla_i^2}{2} + v(\mathbf{x}_i) \Big] + \frac{1}{2} \sum_{i \neq j}^{N_e} \frac{e^2}{|\mathbf{x}_i - \mathbf{x}_j|} = \\ &= \sum_{i=1}^{N_e} T(\mathbf{x_i}) + \frac{1}{2} \sum_{i \neq j}^{N_e} U(\mathbf{x_i}, \mathbf{x_j}), \end{aligned} \tag{4.2}$$

where v is the potential of the host lattice which also includes that of the impurity and U represents an electron-electron interaction. By using second quantization it is seen that the first term, which does not contain any many body interaction, can be written as

$$\begin{aligned} \int \Psi^\dagger(\mathbf{x}) T(\mathbf{x}) \Psi(\mathbf{x}) d\mathbf{x} = &\sum_{\mathbf{k},\sigma} \varepsilon_{\mathbf{k}} c^\dagger_{\mathbf{k}\sigma} c_{\mathbf{k}\sigma} + \sum_{\sigma} \varepsilon_L c^\dagger_{L\sigma} c_{L\sigma} + \sum_{\mathbf{k}\mathbf{k}',\sigma} v_{\mathbf{k}\mathbf{k}'} c^\dagger_{\mathbf{k}\sigma} c_{\mathbf{k}'\sigma} + \\ &+ \sum_{\mathbf{k},\sigma} V_{\mathbf{k}} (c^\dagger_{\mathbf{k}\sigma} c_{L\sigma} + c^\dagger_{L\sigma} c_{\mathbf{k}\sigma}). \end{aligned} \tag{4.3}$$

The first two terms are the onsite contribution to the continuum and the local states respectively. The third term is a potential scattering term between both type of states and can generally be incorporated into the Hamiltonian with a suitable choice of the basis wavefunctions. The important term here is the hybridization term between the continuum and the local atom. This describes a process where electrons are exchanged between the continuum and the local state and survives due to the orthogonality of the electron and local spin system.

The magnetic properties of a system are investigated by examining the electron-

electron interaction terms, which have the form

$$H_U = \int d\mathbf{x} \int d\mathbf{x}' \Psi^\dagger(\mathbf{x})\Psi(\mathbf{x})U(\mathbf{x},\mathbf{x}')\Psi^\dagger(\mathbf{x}')\Psi(\mathbf{x}'). \tag{4.4}$$

This results in a wealth of different terms, involving the local state and contributing differently to the magnetic properties of the system.

(1) The first involves terms which look like

$$H_{\text{direct}} = \frac{1}{2}\sum_{\mathbf{k}\mathbf{k}'}\sum_{\sigma,\sigma'} U_{\mathbf{k}\mathbf{k}'} c^\dagger_{L\sigma} c_{L\sigma} c^\dagger_{\mathbf{k}\sigma'} c_{\mathbf{k}'\sigma'}, \tag{4.5}$$

where

$$U_{\mathbf{k}\mathbf{k}'} = \int d\mathbf{x} \int d\mathbf{x}' \psi^*_{\mathbf{k}}(\mathbf{x})\psi_{\mathbf{k}'}(\mathbf{x})U(\mathbf{x},\mathbf{x}')|\psi_L(\mathbf{x}'-\mathbf{x}_n)|^2, \tag{4.6}$$

which is a direct term and is generally ignored since it does not contribute to any magnetic phenomena.

(2) The second comprises terms which look like

$$H_{\text{sf}} = \frac{1}{2}\sum_{\mathbf{k}\mathbf{k}'}\sum_{\sigma,\sigma'} J_{\mathbf{k}\mathbf{k}'} c^\dagger_{L\sigma} c_{L\sigma'} c^\dagger_{\mathbf{k}\sigma'} c_{\mathbf{k}'\sigma}, \tag{4.7}$$

where

$$J_{\mathbf{k}\mathbf{k}'} = \int d\mathbf{x} \int d\mathbf{x}' \psi^*_{\mathbf{k}}(\mathbf{x})\psi_L(\mathbf{x}-\mathbf{x}_n)U(\mathbf{x},\mathbf{x}')\psi^*_L(\mathbf{x}'-\mathbf{x}_n)\psi_{\mathbf{k}'}(\mathbf{x}'). \tag{4.8}$$

This term represents a spin-flip process where an electron spin can be flipped as it scatters from state k to k'. In order to uphold spin conservation this must be matched by a spin flip of the local spin state. It is easily shown that this term can be restated in terms of

the spin operator $\mathbf{S}_L$ (see Appendix B for definition of spin operators)

$$\frac{1}{2}\sum_{\mathbf{k}\mathbf{k}'}\sum_{\alpha,\alpha'} J_{\mathbf{k}\mathbf{k}'} c^{\dagger}_{\mathbf{k}\alpha} c_{\mathbf{k}'\alpha'} c^{\dagger}_{L\alpha'} c_{L\alpha} = \frac{1}{2}\sum_{\mathbf{k}\mathbf{k}'}\sum_{\alpha,\alpha'} J_{\mathbf{k}\mathbf{k}'} (c^{\dagger}_{\mathbf{k}\alpha}[\boldsymbol{\sigma}]_{\alpha\alpha'} c_{\mathbf{k}'\alpha'}) \cdot \mathbf{S}_L, \tag{4.9}$$

where $[\boldsymbol{\sigma}]$ is a vector of Pauli matrices and $\mathbf{S}_L$ can be written in terms of the localised spin creation and destruction operators as

$$\mathbf{S}_L = (c^{\dagger}_{L\uparrow} c_{L\downarrow} + c^{\dagger}_{L\downarrow} c_{L\uparrow})\hat{\mathbf{x}} + i(c^{\dagger}_{L\downarrow} c_{L\uparrow} - c^{\dagger}_{L\uparrow} c_{L\downarrow})\hat{\mathbf{y}} + (c^{\dagger}_{L\uparrow} c_{L\uparrow} - c^{\dagger}_{L\downarrow} c_{L\downarrow})\hat{\mathbf{z}}. \tag{4.10}$$

This is called the $s-d$ model and is exact for spin $S = 1/2$ but, to a good approximation, can also be satisfied for any general spin with spin quantum number S. The $s-d$ model describes the interaction of conduction s-band electrons with more localized d-orbital electrons, whose total spin component is represented by S. It is clear that the spin-flip terms are those which cause mixing of the quantum state away from the z-axis. This is the model that will be employed in the formalism here-on-out. This Hamiltonian form is useful since conduction electron spins and local electron spins are orthogonal and can therefore be treated separately.

(3) The third and final term involves four local operators and resembles the Anderson Hamiltonian [104]. This looks like

$$H_U = U \sum_{\sigma,\sigma',\sigma'',\sigma'''} c^{\dagger}_{L\sigma} c^{\dagger}_{L\sigma'} c_{L\sigma''} c_{L\sigma'''}, \tag{4.11}$$

where

$$U = \int d\mathbf{x} \int d\mathbf{x}' |\psi_L(\mathbf{x} - \mathbf{x}_n)|^2 U(\mathbf{x}, \mathbf{x}') |\psi_L(\mathbf{x}' - \mathbf{x}_n)|^2. \tag{4.12}$$

H_U becomes the standard Hubbard Hamiltonian [105] if the orbital is non-degenerate and can only support opposite spin states. In this case the sum in Eq. (4.11) is simply

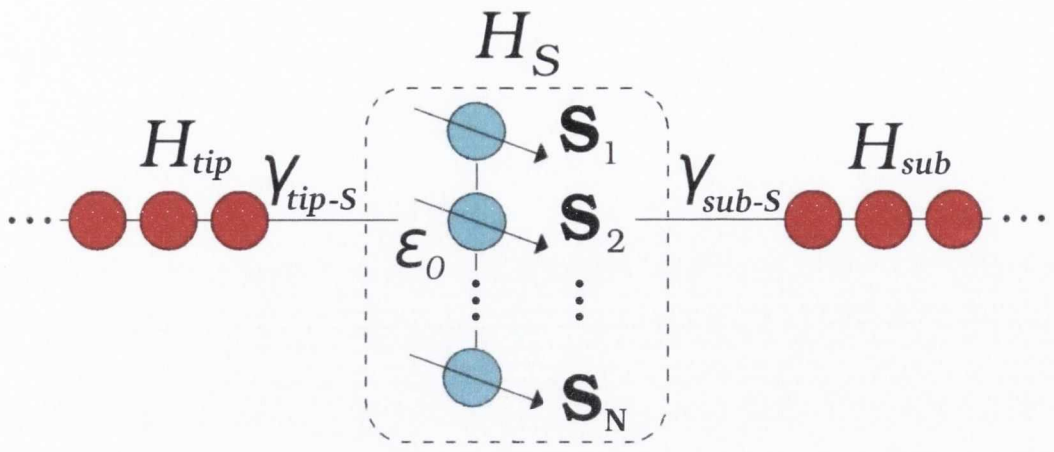

Figure 4.1: Schematic representation of the device investigated in this work. A scattering region, comprising N spin-carrying atoms (light-blue circles) and described by the Hamiltonian H_S, is sandwiched in between two semi-infinite electrodes (red circles). These mimic the substrate and the tip in a typical STM experiment. The electrodes are non-spin polarized and they are described by the Hamiltonian H_{sub} and H_{tip}. In the scattering region the transport electrons are exchange coupled to local quantum spins $\mathbf{S}_i$.

$Uc^\dagger_{L\uparrow}c_{L\uparrow}c^\dagger_{L\downarrow}c_{L\downarrow}$. It should be noted that a canonical transformation exists wherein the Anderson/Hubbard model is transformed into a form similar to that of the Kondo model with additional terms. In this thesis the Kondo $s-d$ model will be used and it will be treated as an approximation to a more general Anderson/Hubbard formalism.

4.2 Hamiltonian of scattering region

The typical experimental setup considered in this thesis is that of an STM measurement, i.e. it comprises an STM tip positioned above one of the atoms of a magnetic nanostructure, which in turn is weakly coupled to a metallic substrate across an insulating barrier. This system is modeled by a pair of non-interacting semi-infinite leads sandwiching a scattering region, as outlined in Fig. 4.1. The left-hand side lead, the scattering region and the right-hand side lead represent respectively the STM tip, the spin-coupled nanostructure and the substrate. They are described respectively by the Hamiltonian $H_{\rm tip}$, $H_{\rm S}$ and $H_{\rm sub}$. For simplicity we assume an identical electronic structure for both the leads (i.e. they are made of the same material), which we describe by a one orbital per site

tight-binding model with nearest neighbour interaction (as in Chapter 3).

To fix the ideas the assumption is made that the scattering region consists of N atoms arranged in a chain structure (note that for this discussion the spatial arrangement of the atoms does not necessarily need to be a chain form). The λ-th atom carries a quantum mechanical spin $\mathbf{S}_\lambda$ and it is characterized by an on-site energy ε_0. It is assumed that the tip and substrate can only couple to one atom at the time in the scattering region, i.e. that only one atom of the magnetic nanostructure is in electronic contact with the electrodes. Such a coupling is given by the two hopping integrals $\gamma_{\text{tip-S}}$ and $\gamma_{\text{sub-S}}$. This means that the electronic states of the scattering region are broadened by the interaction with the electrodes by $\Gamma_{\text{tip-S}} = 2\gamma^2_{\text{tip-S}}/\gamma_0$ and $\Gamma_{\text{sub-S}} = 2\gamma^2_{\text{sub-S}}/\gamma_0$, where γ_0 is again the hopping parameter within the leads. It is assumed that $\varepsilon_0 \gg \Gamma_{\text{tip-S}}$ and also $\varepsilon_0 \gg \Gamma_{\text{sub-S}}$, leading to a constant density of states of the scattering region at the Fermi energy. This assumption has two main consequences. On the one hand, the electronic interaction among the atoms in the scattering region can be neglected (i.e. the creation of bonding and anti-bonding levels is irrelevant), as this will generate states far enough from the Fermi energy to ensure a constant density of states. On the other hand, one can simplify the interaction between the atoms in the chain and the substrate to an electronic coupling to a single atom, as additional coupling (as far as it remains weak) will not introduce additional density of states around ε_{F}.

The Hamiltonian of the scattering region then contains three parts $H_{\text{S}} = H_{\text{e}} + H_{\text{sp}} + H_{\text{e-sp}}$, where H_{e} is the tight-binding electronic part, H_{sp} is the spin part and $H_{\text{e-sp}}$ describes the electron-spin interaction. More explicitly these three components are written

respectively as

$$H_{\mathrm{e}} = \varepsilon_0 \sum_{\lambda\,\alpha} c^{\dagger}_{\lambda\alpha} c_{\lambda\alpha} \,, \tag{4.13}$$

$$H_{\mathrm{sp}} = 2J_{\mathrm{dd}} \sum_{\lambda}^{N-1} \mathbf{S}_\lambda \cdot \mathbf{S}_{\lambda+1} + \sum_{\lambda}^{N} \left\{ g\mu_{\mathrm{B}} \mathbf{B} \cdot \mathbf{S}_\lambda + D(S^z_\lambda)^2 + E[(S^x_\lambda)^2 - (S^y_\lambda)^2] \right\}, \tag{4.14}$$

$$H_{\mathrm{e-sp}} = J_{\mathrm{sd}} \sum_{\lambda\,\alpha,\alpha'} (c^{\dagger}_{\lambda\alpha} [\boldsymbol{\sigma}_\lambda]_{\alpha\alpha'} c_{\lambda\alpha'}) \cdot \mathbf{S}_\lambda \,. \tag{4.15}$$

The electronic part consists only of an on-site potential, i.e. the electron hopping between the sites is neglected [the electron ladder operators $c^{\dagger}_{\lambda\alpha}/c_{\lambda\alpha}$ create/annihilate an electron at site λ with spin α $(=\uparrow,\downarrow)$].

The spin-spin interaction between the localized spins $\{\mathbf{S}_\lambda\}$ is modeled by a nearest neighbour Heisenberg Hamiltonian with coupling strength J_{dd}. Furthermore an interaction with an external magnetic field $\mathbf{B}$ is included (μ_{B} is the Bohr magneton and g the gyromagnetic ratio) and so are both the uni-axial and transverse anisotropy of magnitude D and E, respectively [9, 106]. This form for the spin Hamiltonian is the one proposed before to describe some of the SF-IETS experiments that recently appeared in the literature [5]. Note, however, that the formalism does not depend on the particular choice of such Hamiltonian, and additional terms, such as for instance the one describing Dzyaloshinskii-Moriya interaction [107], can be included. It will be seen that the particular choice of H_{sp} determines the spectrum of the system and consequently the shape of the IETS spectrum, but does not require any modifications of the formalism.

The electron-spin interaction Hamiltonian is constructed within the *s-d* model [51] where the transport electrons, *s*, are locally exchanged coupled to quantum spins, $\{\mathbf{S}_\lambda\}$ ("*d*" indicates that the local moments originate from the atomic *d* shell). The electronic spins are described by the operator $c^{\dagger}_{\lambda\alpha}[\boldsymbol{\sigma}_\lambda]_{\alpha\alpha'} c_{\lambda\alpha'}$,with $\boldsymbol{\sigma}$ being the vector of Pauli matrices. The use of the *s-d* model means that it is implicitly assumed that an adiabatic separation occurs between the transport electrons and those forming the local spins. As

a consequence a single interaction parameter, J_{sd}, can be defined which is used to develop a perturbation theory (note, however, that J_{sd} is not the perturbation expansion parameter, as it will be explained later). Such an approximation is valid in the limit of weak electronic coupling between the electron reservoirs and the scattering region, as in the case of the STM measurements that are described here. Note that going beyond such an approximation will require formulating an entirely electronic theory for inelastic spin transport. An Anderson-like impurity model as introduced in the first section can be a starting Hamiltonian for such a task [108], but this will require abandoning the perturbative approach and it is outside the scope of the present work.

4.3 Many-body Green's functions and interacting electron self energy

The Hamiltonian for the scattering region contains two terms, H_e and H_{sp}, which independently can be diagonalized exactly, so that the problem is easily solvable when $J_{sd} = 0$. However the electron-spin interaction H_{e-sp}, transforms the system into an intrinsic many-body one, for which a perturbation theory will now be derived. The strategy is that of first constructing the electronic many-body Green's function at the 2nd order [98, 109, 110, 111] in the electron-spin coupling and then, by Dyson's equation, evaluating the interacting self-energy. In particular, the procedure laid out in Ref. [98] will be closely followed. Since a non-equilibrium situation at zero-temperature is considered, the starting point is the Schwinger [44] contour-ordered spin-dependent single-body Green's function in the many-body ground state (note that for simplicity the "$\hat{}$" symbol over the operators, denoting the interaction representation, has been dropped),

$$[G(\tau,\tau')]_{\sigma\sigma'} = -i\langle|T_C\{c_\sigma(\tau)c^\dagger_{\sigma'}(\tau')\}|\rangle\,, \tag{4.16}$$

where the time-average is performed over the full interacting ground state $|\rangle$. Note that for clarity the spin index σ has been maintained but the site index λ has been dropped. This will be explicitly included only where necessary. By following the procedure highlighted in the previous sections Eq. (4.16) can be expanded up to the n-th order in the interaction Hamiltonian, $H_{\text{e-sp}}$, as

$$[G(\tau,\tau')]_{\sigma\sigma'} = \sum_n \frac{(-i)^{n+1}}{n!} \int_C d\tau_1 \dots \int_C d\tau_n \times$$
$$\times \frac{{}_0\langle|T_C\{H_{\text{e-sp}}(\tau_1)\dots H_{\text{e-sp}}(\tau_n)c_\sigma(\tau)c^\dagger_{\sigma'}(\tau')\}|\rangle_0}{{}_0\langle|S(-\infty,-\infty)|\rangle_0}, \tag{4.17}$$

where S is the time-evolution unitary operator defined in Eq. (3.11) and the time-averages are now over the known non-interacting ($J_{\text{sd}} = 0$) ground state $|\rangle_0$. The time integration over τ is ordered on the contour C going from $-\infty$ to $+\infty$ and then returning from $+\infty$ to $-\infty$, since the ground state of the non-equilibrium system can only be defined at $-\infty$ [102]. If the expansion is truncated to the first order one obtains a Zeeman-like term which can be neglected as long as $\varepsilon_0 \gg \gamma_{\text{tip-S(sub-S)}}$. The first contribution of interest then appears at the second order. This can be obtained by inserting the explicit expression for $H_{\text{e-sp}}(t)$ [Eq. (4.15)] into Eq. (4.16)

$$[G(\tau,\tau')]^{(2)}_{\sigma\sigma'} = \frac{(-i)^3}{2!} J^2_{\text{sd}} \sum_{i,\alpha,\alpha',j,\beta,\beta'} \int_C d\tau_1 \int_C d\tau_2 \times$$
$$\times {}_0\langle|T_C\{c_\sigma(\tau)c^\dagger_\alpha(\tau_1)c_{\alpha'}(\tau_1)c^\dagger_\beta(\tau_2)c_{\beta'}(\tau_2)c^\dagger_{\sigma'}(\tau')\}|\rangle_{00}\langle|T_C\{S^i(\tau_1)S^j(\tau_2)\}|\rangle_0[\sigma^i]_{\alpha\alpha'}[\sigma^j]_{\beta\beta'}, \tag{4.18}$$

where the indexes i and j of the local spin operators and the Pauli matrices run over the Cartesian coordinates x, y and z (not to be confused with the site index).

A full contour-ordered expansion must now be performed on both the electron and the spin brackets. The electron bracket has six different time-ordering combinations, which

are explicitly below

$$
\begin{aligned}
&{}_0\langle|T_C\{c_\sigma(\tau)c^\dagger_\alpha(\tau_1)c_{\alpha'}(\tau_1)c^\dagger_\beta(\tau_2)c_{\beta'}(\tau_2)c^\dagger_{\sigma'}(\tau')\}|\rangle_0+\\
&=\,{}_0\langle|T_C\{c_\sigma(\tau)c^\dagger_\alpha(\tau_1)\}|\rangle_0\times{}_0\langle|T_C\{c_{\alpha'}(\tau_1)c^\dagger_\beta(\tau_2)\}|\rangle_0\times{}_0\langle|T_C\{c_{\beta'}(\tau_2)c^\dagger_{\sigma'}(\tau')\}|\rangle_0+\\
&+\,{}_0\langle|T_C\{c_\sigma(\tau)c^\dagger_\beta(\tau_2)\}|\rangle_0\times{}_0\langle|T_C\{c_{\alpha'}(\tau_1)c^\dagger_{\sigma'}(\tau')\}|\rangle_0\times{}_0\langle|T_C\{c_\alpha(\tau_2)c^\dagger_{\beta'}(\tau_1)\}|\rangle_0+\\
&+\,{}_0\langle|T_C\{c_\sigma(\tau)c^\dagger_\alpha(\tau_1)\}|\rangle_0\times{}_0\langle|T_C\{c_{\alpha'}(\tau_1)c^\dagger_{\sigma'}(\tau')\}|\rangle_0\times{}_0\langle|T_C\{c^\dagger_\beta(\tau_2)c_{\beta'}(\tau_2)\}|\rangle_0+\\
&+\,{}_0\langle|T_C\{c_\sigma(\tau)c^\dagger_\beta(\tau_2)\}|\rangle_0\times{}_0\langle|T_C\{c_{\beta'}(\tau_2)c^\dagger_{\sigma'}(\tau')\}|\rangle_0\times{}_0\langle|T_C\{c^\dagger_\alpha(\tau_1)c_{\alpha'}(\tau_1)\}|\rangle_0+\\
&+\,{}_0\langle|T_C\{c_\sigma(\tau)c^\dagger_{\sigma'}(\tau')\}|\rangle_0\times{}_0\langle|T_C\{c^\dagger_\alpha(\tau_1)c_{\alpha'}(\tau_1)\}|\rangle_0\times{}_0\langle|T_C\{c^\dagger_\beta(\tau_2)c_{\beta'}(\tau_2)\}|\rangle_0+\\
&-\,{}_0\langle|T_C\{c_\sigma(\tau)c^\dagger_{\sigma'}(\tau')\}|\rangle_0\times{}_0\langle|T_C\{c_{\alpha'}(\tau_1)c^\dagger_\beta(\tau_2)\}|\rangle_0\times{}_0\langle|T_C\{c_{\beta'}(\tau_2)c^\dagger_\alpha(\tau_1)\}|\rangle_0. \qquad (4.19)
\end{aligned}
$$

The first and the second terms represent Fock-like Feynman diagrams [see Fig. (4.2)(B)], while the third and the fourth ones correspond to Hartree-like ones (note that Hartree-like diagrams vanish because of the spin selection rules as discussed later in this section). Both these pairs are equal under index exchange. Finally, the last two combinations can be eliminated since they represent unconnected Feynman diagrams, which vanish in the averaging process [98]. This leaves a simplified expression which, when compared to Eq. (4.16), gives

$$
\begin{aligned}
&{}_0\langle|T_C\{c_\sigma(\tau)c^\dagger_\alpha(\tau_1)c_{\alpha'}(\tau_1)c^\dagger_\beta(\tau_2)c_{\beta'}(\tau_2)c^\dagger_{\sigma'}(\tau')\}|\rangle_0\\
&=2i^3\delta_{\sigma\alpha}\delta_{\alpha'\beta}\delta_{\beta'\sigma'}[G_0(\tau,\tau_1)]_{\sigma\sigma}[G_0(\tau_1,\tau_2)]_{\alpha'\alpha'}[G_0(\tau_2,\tau')]_{\sigma'\sigma'}+\\
&+\;2i^3\delta_{\sigma\alpha}\delta_{\alpha'\sigma'}\delta_{\beta\beta'}[G_0(\tau,\tau_1)]_{\sigma\sigma}[G_0(\tau_1,\tau')]_{\sigma'\sigma'}[G_0(\tau_2,\tau_2)]_{\beta\beta}. \qquad (4.20)
\end{aligned}
$$

In this case, since the averaging bracket is over the non-interacting ground state, G_0 represents the non-interacting electronic Green's function and can be calculated exactly (see Chapter 3).

Returning to Eq. (4.17) the spin bracket is now evaluated. The ground state of the spin system alone ($J_{\rm sd}=0$) can be found by diagonalizing exactly $H_{\rm sp}$. This is achieved

by constructing the full spin basis $\{|n\rangle\}$ where $n = -S, -S+1, ..., +S$. Note that this step does not require any particular form for $H_{\rm sp}$, although the details of the spin Hamiltonian determine the nature of the spin states and how these interact with the conducting electrons. Note also that in the discussion of the results the labeling of the eigenvalues of $H_{\rm sp}$ will be kept with the z-component of the total spin S, which in general is not a good quantum number because of the presence of the transverse anisotropy. However, such an anisotropy is typically small so that the notation remains approximately valid. The resulting eigenvectors, $|m\rangle$, and eigenvalues, ε_m, satisfy the Schrödinger equation $H_{\rm sp}|m\rangle = \varepsilon_m|m\rangle$ and they can be used to re-write the operators $S^i(\tau)$, for $i = \{x, y, z\}$, as

$$S^i(\tau) = \sum_{m,n} \langle m|S^i|n\rangle d_m^\dagger(\tau) d_n(\tau) \,. \tag{4.21}$$

Here d_n ($d_n^\dagger$) is an annihilation (creation) operator for a quasi-particle of the spin system. The quasi-particles are then assumed to be fermionic in nature so that they obey the anti-commutation rules $[d_m^\dagger, d_n] = \delta_{mn}$ and $[d_m^\dagger, d_n^\dagger] = [d_m, d_n] = 0$. Such an assumption is valid as long as the excitations considered are always around the ground state, i.e. under the condition that the spin system can always efficiently relax back to the ground state between spin-flip events. Note that in this situation only a single spin-state $|m\rangle$ can be excited at a time, so that the particular particle statistics, bosons or fermions, becomes irrelevant.

A contour-ordered spin Green's function is then defined as follows

$$[D(\tau, \tau')]_{n,m} = -i\langle|T_C\{d_n(\tau) d_m^\dagger(\tau')\}|\rangle \,. \tag{4.22}$$

By inserting the expressions contained in Eqs. (4.21) and (4.22) into the spin bracket and

by computing the time-ordered contraction one finally obtains

$$\langle 0|T_C\{S^i(\tau_1)S^j(\tau_2)\}|0\rangle = -\sum_{m,n}\langle m|S^i|n\rangle\langle n|S^j|m\rangle[D_0(\tau_1,\tau_2)]_{n,n}[D_0(\tau_2,\tau_1)]_{m,m}\,, \quad (4.23)$$

where D_0 is the unperturbed spin Green's function.

The set of Eqs. (4.20) and (4.23) can now be incorporated into the expression for the second order contribution to the many-body Green's function [Eq. (4.17]. Then, by using Dyson's equation [98], one can finally write the second order contribution to the interacting self-energy which reads

$$[\Sigma_{\rm int}(\tau_1,\tau_2)]^{(2)}_{\sigma\sigma'} = -J_{\rm sd}^2\sum_{i,j,\beta}\left\{[\sigma^i]_{\sigma\beta}[\sigma^j]_{\beta\sigma'} + [\sigma^i]_{\sigma\sigma'}[\sigma^j]_{\beta\beta}\right\}$$
$$\times\,[G_0(\tau_1,\tau_2)]_{\beta\beta}\sum_{m,n}\langle m|S^i|n\rangle\langle n|S^j|m\rangle[D_0(\tau_1,\tau_2)]_{n,n}[D_0(\tau_2,\tau_1)]_{m,m}\,. \quad (4.24)$$

If it is now assumed that the ground state electronic spin levels are degenerate (the electrodes are not magnetic), i.e. $[G_0]_{\uparrow\uparrow} = [G_0]_{\downarrow\downarrow}$, then the only quantity of interest is the trace of the self-energy over spin indexes. By performing such a trace, the spin-independent self-energy finally reads

$$\Sigma_{\rm int}(\tau_1,\tau_2)^{(2)} = -2J_{\rm sd}^2\sum_{i,m,n}|\langle m|S^i|n\rangle|^2 G_0(\tau_1,\tau_2)[D_0(\tau_1,\tau_2)]_{n,n}[D_0(\tau_2,\tau_1)]_{m,m},\,. \quad (4.25)$$

where the results $\mathrm{Tr}[\sigma^i\sigma^j] = \delta_{ij}$ and $\mathrm{Tr}[\sigma^i] = 0$ have been used. Note that the relation $\mathrm{Tr}[\sigma^i] = 0$ guarantees that the Hartree-like diagrams do not contribute to the self-energy. Such a relation is not present when the interaction of the conducting electrons is with atomic vibrations (phonons), hence in that situation the Hartree-like diagrams cannot be *a priori* neglected. Interestingly, for the phonon case the Hartree-like diagrams drive possible polaronic distortions in the system [112], which are expected not to have an equivalent in the case of spin scattering.

At this point the real-time quantities can be calculated, such as the lesser (greater) self-energies, by using the Langreth's theorem for time ordering over the contour, $\tau_1 \in C_1(C_2)$ and $\tau_2 \in C_2(C_1)$ [102]. C_1 is the time ordering contour going from $-\infty$ to $+\infty$ and C_2 is the time anti-ordering contour going from $+\infty$ to $-\infty$. It is found that

$$\begin{aligned}\Sigma^{\lessgtr}_{\text{int}}(t_1,t_2)^{(2)} &= -2J^2_{\text{sd}} \sum_{i,m,n} |\langle m|S^i|n\rangle|^2 G^{\lessgtr}_0(t_1,t_2)[D^{\lessgtr}_0(t_1,t_2)]_{n,n}[D^{\gtrless}_0(t_2,t_1)]_{m,m} \\ &= -2J^2_{\text{sd}} \sum_{i,m,n} |\langle m|S^i|n\rangle|^2 G^{\lessgtr}_0(t_1,t_2) P_n(1-P_m) e^{\pm i(\varepsilon_m-\varepsilon_n)(t_1-t_2)} , \end{aligned} \tag{4.26}$$

where in the second step $D^{\lessgtr}_0(t_1,t_2)$ has been written explicitly in terms of the spin-level occupations, $P_n = d^\dagger_n d_n$. It is reiterated that this form of the spin Green's function is correct in the limit that excitations are always close to the ground state and therefore the latter expression is a good approximation. The dependence of $\Sigma^{\lessgtr}_{\text{int}}$ over the energy, E, can be found by simple Fourier transform

$$\Sigma^{\lessgtr}_{\text{int}}(\omega)^{(2)} = -2J^2_{\text{sd}} \sum_{i,m,n} |\langle m|S^i|n\rangle|^2 P_n(1-P_m) G^{\lessgtr}_0(\omega \pm \Omega_{mn}) , \tag{4.27}$$

where $\Omega_{mn} = \varepsilon_m - \varepsilon_n$ and where the $+$ $(-)$ symbol corresponds to $\Sigma^<$ $(\Sigma^>)$.

Electron-spin scattering events are now fully described by $[\Sigma^{\lessgtr}_{int}(\omega)]$. In particular Eq. (4.27) describes the process where an incoming electron with energy E experiences a spin-flip process, which changes its energy by $\pm\Omega_{mn}$. This is the result of the electron-spin interaction with the local spins. Such a process is schematically represented in Fig. 4.2. Note that the probability for an excitation to occur is determined by the prefactors $\langle m|S^i|n\rangle|^2 P_n(1-P_m)$, i.e. by the state of the spin system.

This section is concluded by discussing the limits of validity of the perturbative expansion. From a first inspection of the Eq. (4.27) one could conclude that the strength of the second order interacting self-energy is solely dependent on J^2_{sd}. This will indeed result in a large perturbation parameter and thus in a possibly divergent perturbative expansion

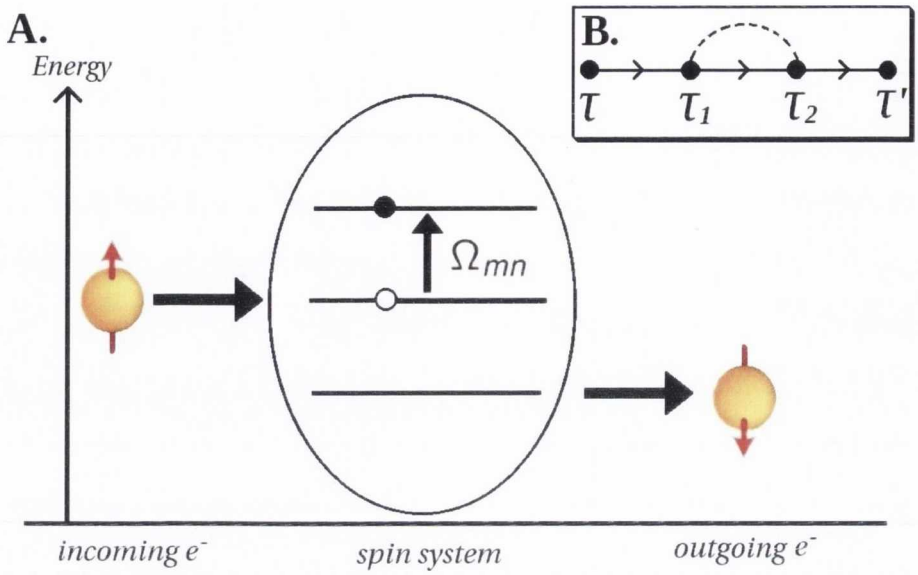

Figure 4.2: (A) Schematic representation of the inelastic process described by the greater self-energy, $\Sigma^{>}_{\rm int}$. An incoming electron scatters against a localized spin and decreases its energy by Ω_{mn}. This is transfer to the local spin system, which undergoes a spin transition $|n\rangle \rightarrow |m\rangle$. (B) Feynman Fock-like diagram describing the interaction in the time domain.

(see Table (5.3) for an estimate of the various parameters). However, both the lesser and the greater Green's functions are proportional to the density of states of the scattering region, ρ. In the weak coupling limit one has $\rho \sim \Gamma/\varepsilon_0^2$, where ε_0 is the onsite energy of the atom under consideration (the one under the tip) and Γ is the total broadening due to the electrodes, $\Gamma = \Gamma_{\rm tip-S} + \Gamma_{\rm sub-S}$. As a consequence one has that $\Sigma^{\lessgtr}_{\rm int}(\omega)^{(2)} \sim \alpha J_{\rm sd}$, where $\alpha = \rho J_{\rm sd}$ is a dimensionless quantity. By continuing the expansion to the third order (see next section) one will find an additional contribution to the interacting self-energy proportional to $\alpha^2 J_{\rm sd}$, i.e. it will be discovered that the perturbation expansion parameter is the dimensionless quantity α. Interestingly, α is the product between the Fermi level density of state at the spin site and the exchange parameter $J_{\rm sd}$, i.e. it is essentially the Stoner parameter [113]. The convergence of the perturbation series is then guaranteed by the weak coupling condition, which establishes that ρ is small and then $\alpha \ll 1$.

4.4 3rd order electron interacting self energy

Having described how to deal with the electron spin interaction up to the 2nd order, it is now interesting to continue such a perturbative expansion further to third order and to examine what effects this has on the conductance spectra. Our starting point is again the interacting contour ordered Green's function expanded up to order n, Eq. (4.17). Once the explicit form for $H_{\mathrm{e-sp}}$ is introduced the third order contribution to the perturbative series reads

$$
\begin{aligned}
[G(\tau,\tau')]^{(3)}_{\sigma,\sigma'} = & \frac{(-i)^4}{3!} J^3_{\mathrm{sd}} \sum_{\alpha\alpha',\beta\beta',\gamma\gamma'} \int_C d\tau_1 \int_C d\tau_2 \int_C d\tau_3 \times \\
& \times \langle T_C\{c_\sigma(\tau) c^\dagger_\alpha(\tau_1) c_{\alpha'}(\tau_1) c^\dagger_\beta(\tau_2) c_{\beta'}(\tau_2) c^\dagger_\gamma(\tau_3) c_{\gamma'}(\tau_3) c^\dagger_{\sigma'}(\tau')\}\rangle \times \\
& \times \sum_{i,j,k} \langle T_C\{S^i(\tau_1) S^j(\tau_2) S^k(\tau_3)\}\rangle [\sigma^i]_{\alpha\alpha'} [\sigma^j]_{\beta\beta'} [\sigma^k]_{\gamma\gamma'} \, . \qquad (4.28)
\end{aligned}
$$

Firstly the spin operators are considered. Following the procedure presented in the previous section these are decomposed into products of quasi-particle operators obeying the Fermi-Dirac statistics, thus that the i-th component ($i = x, y, z$) of the spin operator $\mathbf{S}$ is written according to Eq. (4.21) and the corresponding Green's function is that of Eq. (4.22). By substituting these expressions into Eq. (4.28) one obtains

$$
\begin{aligned}
[G(\tau,\tau')]^{(3)}_{\sigma,\sigma'} = & \frac{(-i)^4}{3!} J^3_{\mathrm{sd}} \sum_{\alpha\alpha',\beta\beta',\gamma\gamma'} \int_C d\tau_1 \int_C d\tau_2 \int_C d\tau_3 \times \\
& \times \langle T_C\{c_\sigma(\tau) c^\dagger_\alpha(\tau_1) c_{\alpha'}(\tau_1) c^\dagger_\beta(\tau_2) c_{\beta'}(\tau_2) c^\dagger_\gamma(\tau_3) c_{\gamma'}(\tau_3) c^\dagger_{\sigma'}(\tau')\}\rangle \times \\
& \times \sum_{mm',nn',ll'} \langle T_C\{d^\dagger_m(\tau_1) d_{m'}(\tau_1) d^\dagger_n(\tau_2) d_{n'}(\tau_2) d^\dagger_l(\tau_3) d_{l'}(\tau_3)\}\rangle \times \\
& \times \sum_{i,j,k} \langle m|S^i|m'\rangle \langle n|S^j|n'\rangle \langle l|S^k|l'\rangle [\sigma^i]_{\alpha\alpha'} [\sigma^j]_{\beta\beta'} [\sigma^k]_{\gamma\gamma'} \, . \qquad (4.29)
\end{aligned}
$$

The chronological contractions are now performed by using Wick's theorem for both the electron and spin bracket. It has previously been stated that the electron brackets, the

spin selection rules and the electronic spin-degeneracy impose a vanishing contribution for any "fermion loop" contraction of the form $\langle c^{\dagger}(\tau)c(\tau)\rangle$. Therefore, one needs only to consider the three Fock-like contributions to the electron bracket. These are all equal under exchange of contour indexes. Furthermore the spin bracket brings two Fock-like terms. Here we retain only one of them in order to simplify the discussion, but both have been included in the numerical simulations that we will show later. With this information in hand Eq. (4.29) can be written in terms of the known non-interacting electron and spin Green's functions

$$
\begin{aligned}
[G(\tau,\tau')]^{(3)}_{\sigma,\sigma'} = i\frac{J^3_{\mathrm{sd}}}{2}\sum_{\beta,\gamma}\int_C d\tau_1\int_C d\tau_2\int_C d\tau_3\ \times \\
\times\,[G_0(\tau,\tau_1)]_{\sigma\sigma}[G_0(\tau_1,\tau_2)]_{\beta\beta}[G_0(\tau_2,\tau_3)]_{\gamma\gamma}[G_0(\tau_3,\tau')]_{\sigma'\sigma'}\times \\
\times\sum_{m,n,l}[D_0(\tau_1,\tau_2)]_{n,n}[D_0(\tau_2,\tau_3)]_{l,l}[D_0(\tau_3,\tau_1)]_{m,m}\times \\
\times\sum_{i,j,k}\langle m|S^i|n\rangle\langle n|S^j|l\rangle\langle l|S^k|m\rangle[\sigma^i]_{\sigma\beta}[\sigma^j]_{\beta\gamma}[\sigma^k]_{\gamma\sigma'}. \qquad (4.30)
\end{aligned}
$$

Dyson's equation is now used to extract from Eq. (4.30) the third-order contribution to the interacting self energy, which takes the form

$$
\begin{aligned}
\Sigma(\tau_1,\tau_3)^{(3)} = 2iJ^3_{\mathrm{sd}}\int_C d\tau_2 G_0(\tau_1,\tau_2)G_0(\tau_2,\tau_3)\times \\
\times\sum_{m,n,l}D_n(\tau_1,\tau_2)D_l(\tau_2,\tau_3)D_m(\tau_3,\tau_1)\sum_{i,j,k}(2i\varepsilon_{ijk})\langle m|S^i|n\rangle\langle n|S^j|l\rangle\langle l|S^k|m\rangle. \qquad (4.31)
\end{aligned}
$$

Note that in order to simplify the notation the diagonal elements of the non-interacting spin self-energy have been written as $D_m(\tau,\tau')$. In the same Eq. (4.33) the electron spin degeneracy has also been taken into account ($[G_0]_{\uparrow\uparrow} = [G_0]_{\downarrow\downarrow}$) and traced over the spin indices. Finally it is noted that $\mathrm{Tr}[\sigma^i\sigma^j\sigma^k] = 2i\varepsilon_{ijk}$.

Equation (4.31) now needs to be expressed in terms of the real times (t,t'), so that a close expression for the energy resolved lesser and greater interacting self-energies can be

explicitly written. Such a derivation is based on the Schwinger formalism for evaluation of time-contour integrals [44, 102] and is illustrated in Appendix C. Finally the complete expression for the interacting self-energies is obtain by adding the second order term derived before, see Eq. (4.27), to give

$$\Sigma^{\lessgtr}_{\rm int}(\omega) = -2J_{\rm sd}^2 \sum_{m,n,l} P_l(1-P_m) G_0^{\lessgtr}(E \pm \Omega_{ml}) \Big\{ \delta_{nl} \sum_i |\langle m|S^i|n\rangle|^2 + \\ + 2i(\rho J_{\rm sd}) \sum_{ijk} \varepsilon_{ijk} \langle m|S^i|n\rangle\langle n|S^j|l\rangle\langle l|S^k|m\rangle \times \\ \times \Big[\ln\Big| \frac{W}{\sqrt{(E+V\pm\Omega_{mn})^2 + (k_{\rm B}T)^2}} \Big| + \ln\Big| \frac{W}{\sqrt{(E+V\pm\Omega_{nl})^2 + (k_{\rm B}T)^2}} \Big| \Big] \Big\}, \tag{4.32}$$

where the plus (minus) sign corresponds to $<$ ($>$). If it is now assumed that the scattering region is much more strongly coupled to the substrate than to the STM tip ($\gamma^{\rm sub-S} \gg \gamma^{\rm tip-S}$) and $\varepsilon_0 \gg \varepsilon_{\rm F}$, one can approximate the tip density of states around $\varepsilon_{\rm F}$ with a constant, $\rho = (\Gamma/2\pi)/[\varepsilon_0^2 + \Gamma^2]$. The weak coupling to the STM tip also ensures that the spin system remains always close to equilibrium [27], i.e. in its ground state, so that $P_0 \sim 1$. A crucial feature of the third order contribution to the self-energies is the appearance of a zero-temperature logarithmic divergence at the excitation energies Ω_{mn}. This is the fingerprint of the Kondo effect and will be the key ingredient to describe zero-bias anomalies in the conductance spectrum as well as the details of the spectrum line-shape. Note that the formalism and derivation leading to Eq. (4.32) has been proposed first for describing the Kondo effect in quantum dots [20, 54].

4.5 Additional lineshape features

In the following section the NEGF formalism will be extended to spin scattering to include the additional features necessary to describe transport in the case that the electrodes are spin-polarized or when the current is intense. In particular, the spin interaction

electronic self-energy will be generalized to the spin-polarized case and a second order perturbative expansion for the spin propagator will be constructed, so that the non-equilibrium occupation of the various spin-states will be evaluated. Finally, examples will be shown of how the various levels of theory perform when applied to real problems.

4.5.1 Modifications to the interaction Hamiltonian and spin-polarized electron self-energy

The same Hamiltonian as introduced in Eqs. (4.13-4.15) is used in this section with the only difference being that the electron-spin interaction, Eq. (4.15), is now modified as follows

$$H_{\mathrm{e-sp}} = J_{\mathrm{sd}} \sum_{\lambda\,\alpha,\alpha'} (c^{\dagger}_{\lambda\alpha}[\boldsymbol{\sigma}_{\lambda}]_{\alpha\alpha'} c_{\lambda\alpha'}) \cdot \mathbf{S}_{\lambda} \; + \varepsilon_0 \sum_{\lambda\,\alpha} c^{\dagger}_{\lambda\alpha} c_{\lambda\alpha}. \tag{4.33}$$

$H_{\mathrm{e-sp}}$ now includes a second term, which represents the potential scattering elastic contribution to the *s-d* interaction with strength ε_0 (this is sometimes called the magnetoresistive elastic term and will be included now in the perturbation expansion). The inelastic ratio, $\chi = \varepsilon_0/J_{\mathrm{sd}}$, is typically in the range of 1 to 2. This term was not included before as it becomes important only in the case of spin-polarized electrodes.

The starting point for generalizing the theory to spin-polarized electrodes is once again the perturbation expansion of the spin-resolved contour ordered interacting Green's function, namely Eq. (4.17). Here only the tip is considered to be spin-polarized, with the spin-polarization being described by a single parameter, η. This means that the tip-induced electronic broadening is different for the two spin species, namely $[\Gamma_{\mathrm{tip-S}}]_{\uparrow\uparrow} = (1+\eta)\Gamma_{\mathrm{tip-S}}/2$ and $[\Gamma_{\mathrm{tip-S}}]_{\downarrow\downarrow} = (1-\eta)\Gamma_{\mathrm{tip-S}}/2$, where $\Gamma_{\mathrm{tip-S}}$ is the non-polarized broadening. As a result one has $[G_0^{\lessgtr}(E)]_{\uparrow\uparrow} \neq [G_0^{\lessgtr}(E)]_{\downarrow\downarrow}$. One then needs to carry out the same steps as in the previous expansion to the second order, with the only exception that the trace over the spin indexes is not taken. The following expression for the spin resolved

components of the interacting self-energy is then obtained

$$[\Sigma^{\lessgtr}_{\text{int}}(E)]^{(2)}_{\uparrow\uparrow} = - J^2_{\text{sd}} \sum_{m,n} [G^{\lessgtr}_0(E \pm \Omega_{mn})]_{\uparrow\uparrow} \Big(\delta_{nm} \chi P_n S^z_{mn} + P_n(1 - P_m) |S^z_{mn}|^2 \Big) + \\ - J^2_{\text{sd}} \sum_{m,n} [G^{\lessgtr}_0(E \pm \Omega_{mn})]_{\downarrow\downarrow} P_n(1 - P_m) |S^+_{mn}|^2, \tag{4.34}$$

$$[\Sigma^{\lessgtr}_{\text{int}}(E)]^{(2)}_{\downarrow\downarrow} = - J^2_{\text{sd}} \sum_{m,n} [G^{\lessgtr}_0(E \pm \Omega_{mn})]_{\downarrow\downarrow} \Big(- \delta_{nm} \chi P_n S^z_{mn} + P_n(1 - P_m) |S^z_{mn}|^2 \Big) + \\ - J^2_{\text{sd}} \sum_{m,n} [G^{\lessgtr}_0(E \pm \Omega_{mn})]_{\uparrow\uparrow} P_n(1 - P_m) |S^-_{mn}|^2. \tag{4.35}$$

The lesser/greater self-energies describe the process where an incoming/outgoing electron can excite/relax the spin system by Ω_{mn} with a probability dependent on the occupation of the spin levels P_m and P_n and on the spin selection rules $S^{z,+,-}_{mn}$ (note: $S^+ = S^x + iS^y$ and $S^- = S^x - iS^y$). The first term in both Eqs. (4.34) and (4.35) preserves the electron spins in the scattering event and it is associated to the magnetoresistive elastic term of the *s-d* Hamiltonian [see Eq. (4.33)]. The other contributions are inelastic in nature and depend on the spin orientation of the incoming/outgoing electron from/to the tip.

4.5.2 The spin propagator

So far it has been assumed that the spin system is always in its ground state before a scattering event, i.e. that there is no build up of spin population. This is justified by the fact that in typical STM experiments the current is usually small, the temperature is extremely low and the electrodes are not spin-polarized. The situation however changes for spin-polarized electrodes and/or large current density, since a spin-flip scattering event can be followed by a second one without the spin system having enough time to relax to its ground state. In this case a realistic transport description should include the calculation of the non-equilibrium spin population. The same argument goes for the inclusion of finite

temperature in the problem.

Firstly, the following non-interacting case is considered in which there is no exchange coupling between the current and the spins but the temperature is finite. It is then assumed that the spin system is adiabatically coupled to a heat-bath kept at temperature T, which generates a weak broadening to the single spin states ε_m of magnitude k_BT. In this non-interacting case the spin Green's function (propagator) of Eq. (4.22) simply becomes

$$[D_0^{\lessgtr}(E)]_{m,n} = \frac{[\Pi_0^{\lessgtr}(E)]_{m,n}}{(E-\varepsilon_m)^2 + (k_BT)^2}\,, \tag{4.36}$$

where $[\Pi_0^{>}(E)]_{m,n} = \delta_{m,n}(1-P_m^0)k_BT$ and $[\Pi_0^{<}(E)]_{m,n} = \delta_{m,n}P_m^0 k_BT$, with P_m^0 being the ground state population at zero-temperature.

If the interaction with the conducting electrons is now switched on the spin population becomes dependent on the bias as spins can be pumped from the spin-polarized electrodes. The task is then that of calculating the non-equilibrium spin population P_n, as these are the relevant quantities entering the total electronic Green's function. By combining the first and second order contributions to the spin self-energy one can derive (see Appendix D for details) a master equation for P_n, in terms of the total spin self-energy $\Pi^{\lessgtr}(E)$

$$\frac{dP_n}{dt} = \frac{1}{\hbar}\sum_m \int_{-\infty}^{+\infty} dE\Big\{[\Pi^{>}(E)]_{nm}[D_0^{<}(E)]_{mn} - \Pi^{<}(E)]_{nm}[D_0^{>}(E)]_{mn}\Big\}. \tag{4.37}$$

After some rearrangement this can be written in more compact form as

$$\frac{dP_n}{dt} = \frac{1}{hbar}\sum_l \Big[P_n(1-P_l)W_{ln} - P_l(1-P_n)W_{nl}\Big] + (P_n^0 - P_n)/\beta, \tag{4.38}$$

where the bias dependent transition rate from an initial state l to a final state n is calculated after evaluating the integral in Eq. (D.7) from the appendix and $\beta = 1/k_BT$.

Its final form is given by

$$W_{nl} = -4\frac{(\rho J_{\rm sd})^2}{\Gamma}\sum_{\eta,\eta'}\zeta(\mu_\eta - \mu_{\eta'} + \Omega_{ln})\Big\{\chi S^z_{nn}\Big([\Gamma_\eta]_{\uparrow\uparrow}[\Gamma_{\eta'}]_{\uparrow\uparrow} - [\Gamma_\eta]_{\downarrow\downarrow}[\Gamma_{\eta'}]_{\downarrow\downarrow}\Big) +$$
$$+ |S^z_{nl}|^2\Big([\Gamma_\eta]_{\uparrow\uparrow}[\Gamma_{\eta'}]_{\uparrow\uparrow} + [\Gamma_\eta]_{\downarrow\downarrow}[\Gamma_{\eta'}]_{\downarrow\downarrow}\Big) + |S^+_{nl}|^2[\Gamma_\eta]_{\downarrow\downarrow}[\Gamma_{\eta'}]_{\uparrow\uparrow} + |S^-_{nl}|^2[\Gamma_\eta]_{\uparrow\uparrow}[\Gamma_{\eta'}]_{\downarrow\downarrow}\Big\}, \quad (4.39)$$

where $\zeta(x) = x/[1 - e^{-x/k_{\rm B}T}]$ and μ_η is the chemical potential in lead $\eta = \{\text{tip}, \text{sub}\}$. The form of $\zeta(x)$ is such that for $\eta = \eta'$ the resulting transition rates W_{nl} are bias independent and do not contribute to the current. They do however contribute to the spin relaxation time, i.e. to the time taken for the spin to relax back to its equilibrium state. This relaxation time gets shorter if the coupling between the sample and the leads increases. Also, the smaller the inelastic energy transition Ω_{mn}, the longer the spin will remain in its excited state before relaxing back to equilibrium. Again, one assumes that the onsite energy is large enough so that the density of states of the sample remains constant in the small energy window of interest, i.e. $\rho = \Gamma/(\varepsilon_0^2 + \Gamma^2)$.

Returning to Eq. (4.38), it is worth noting that one is interested only in steady state transport, so that the relevant quantities are the non-equilibrium steady-state spin populations at a given bias. Therefore the condition $dP_n(t)/dt = 0$ is evoked and Eq. (4.38) is solved for the steady-state, by simply iterating from an initial trial population ($P_l = P_l^0$). Finally the converged populations are used to evaluate the electronic spin-scattering self-energy.

4.5.3 Real Part of the Electron Self Energy

In order to provide an explanation to the inherent bias-asymmetry that has been observed in most of the STM inelastic conductance spectra for magnetic atoms probed by a non-magnetic STM tip [5, 9], the expression for the full retarded self-energy must be revisited. This is defined by the Hilbert transform (for simplicity only the non-spin polarized case

will be considered)

$$\Sigma_{\text{int}}(E) = \mathcal{PV}\int_{-\infty}^{+\infty}\frac{dE'}{2\pi}\frac{\Sigma^{>}_{\text{int}}(E')+\Sigma^{<}_{\text{int}}(E')}{E-E'}+ \\ -\frac{i}{2}\{\Sigma^{>}_{\text{int}}(E')+\Sigma^{<}_{\text{int}}(E')\}\,. \tag{4.40}$$

By using the expressions derived in Section 4.3 for the 2$^{\text{nd}}$ order lesser and greater self-energies an analytic expression is found for the real contribution to the retarded self-energy

$$\text{Re}[\Sigma_{\text{int}}(E)^{(2)}] = 2\rho J_{\text{sd}}^2\sum_{i,m,n}|S^i_{mn}|^2P_n(1-P_m)\times \\ \times\frac{1}{\Gamma}\Big\{2\pi\varepsilon_0+\sum_{\eta}\Gamma_{\eta-\text{S}}\ln\Big[\frac{(E+\Omega_{mn}-\mu_\eta)^2+(k_BT)^2}{(E-\Omega_{mn}-\mu_\eta)^2+(k_BT)^2}\Big]\Big\}\,. \tag{4.41}$$

Such a final expression is heavily dependent on the on-site energy ε_0 but it is also noted that the ratio $\Gamma_{\text{tip}-\text{S}}/\Gamma_{\text{sub}-\text{S}}$ has a profound influence on the degree of asymmetry present in the conductance spectrum. If $\Gamma_{\text{tip}-\text{S}}/\Gamma_{\text{sub}-\text{S}} = 1$ then the asymmetry is removed. Provided that $\Gamma_{\text{tip}-\text{S}} < \Gamma_{\text{sub}-\text{S}}$, which is a condition normally met in STM-IETS experiments, an asymmetry will always be present. This is a result also found in references [20, 55]. The condition $\Gamma_{\text{tip}-\text{S}} < \Gamma_{\text{sub}-\text{S}}$ makes the real part of the self-energy an odd function of the energy and the bias via its logarithmic dependence on the spin eigenvalues with opposite polarity for $+\Omega_{mn}$ and $-\Omega_{mn}$. Therefore one of the main physical causes of the bias asymmetry in the conductance spectra is the uneven electronic couplings between the scattering atoms and two non-interacting leads. As such this is a feature common to all IETS experiments, including those using non spin-polarized tips or scattering to phonon. In this work we solely focus on non spin-polarized tip and spin-excitations.

4.6 Non-equilibrium Green's function method for electron transport

Finally, before showing a sample of results obtained by applying the theory discussed so far, one needs to generalize the electron transport scheme introduced in Chapter 3 to include the effect of the inelastic electron-spin interaction in the scattering region. A two-probe device is considered, which is then divided into three distinct regions, two semi-infinite leads representing respectively the STM tip and the underlying substrate and a central scattering region (see Fig. 4.1). As mentioned before the leads act as charge reservoirs and they are characterized by their chemical potentials, respectively $\mu_{\rm tip}$ and $\mu_{\rm sub}$. An external bias is introduced in the form of a relative shift (symmetric) of the two chemical potentials with respect to each other. The underlying assumption of the method is that under the external bias there is no rearrangement of the electronic structure of the leads, i.e. that the electron screening and the spin relaxation in the leads are efficient. This simplifies the problem to that of calculating the retarded (and the advanced) Green's function of the scattering region [45, 46, 111] only

$$G^r(\omega) = \lim_{\delta \to 0}[(\omega - i\delta)I - H_{\rm e} - \Sigma^r(\omega)]^{-1} \, . \tag{4.42}$$

Here $H_{\rm e}$ is the electronic part of the Hamiltonian [Eq. (4.13)] and $\Sigma^{\rm r}(\omega)$ is the retarded self-energy, which now incorporates the effects of the leads and of the inelastic interaction. In particular $\Sigma(\omega)$ writes as

$$\Sigma^r(\omega) = \Sigma^r_{\rm tip}(\omega) + \Sigma^r_{\rm sub}(\omega) + \Sigma^r_{\rm int}(\omega) \, , \tag{4.43}$$

where $\Sigma^r_{\rm tip}(\omega)$ and $\Sigma^r_{\rm sub}(\omega)$ are respectively the STM tip and substrate retarded self-energies, while $\Sigma^r_{\rm int}$ is the scattering self-energy describing the electron-spin interaction. Formally the action of the electron-spin interaction is similar to that of a current-voltage

electrode, so that it can be interpreted as a fictitious lead, which conserves the total current but breaks the electron and the spin phase-coherence. The leads' self-energies are defined in Eq. (3.59), where now i=tip, sub. Finally, the retarded electron-spin scattering self-energy is found from the Hilbert transform of the lesser and greater counterparts [111]

$$\Sigma^r_{\rm int}(\omega) = \mathcal{PV}\int_{-\infty}^{\infty}\frac{d\omega'}{2\pi}\frac{\Sigma^>_{\rm int}(\omega')+\Sigma^<_{\rm int}(\omega')}{\omega'-\omega} + -\frac{i}{2}[\Sigma^>_{\rm int}(\omega)+\Sigma^<_{\rm int}(\omega)], \tag{4.44}$$

where $\mathcal{PV}$ denotes the principal value and where the full expressions for $\Sigma^>_{\rm int}(\omega)$ and $\Sigma^<_{\rm int}(\omega)$ have been given in the previous sections. Note that at variance with a similar expression for the self-energy describing electron-phonon scattering, in Eq. (4.44) there is no Hartree-like contribution. This usually describes polaronic effects and it is known to cause the breakdown of the Born approximation for strong electron-phonon coupling [112], the absence of which makes this similar perturbative approach for spins quite advantageous.

In addition to the retarded self-energy also the lesser and greater ones and the Green's function can be expressed as a sum over all three contributions

$$\Sigma^{\lessgtr}(\omega) = \Sigma^{\lessgtr}_{\rm tip}(\omega) + \Sigma^{\lessgtr}_{\rm sub}(\omega) + \Sigma^{\lessgtr}_{\rm int}(\omega)\,. \tag{4.45}$$

$$G^{\lessgtr}(\omega) = G^r(\omega)[\Sigma^{\lessgtr}(\omega)]G^a(\omega)\,, \tag{4.46}$$

The external bias, introduced as a shift of the leads chemical potentials $\mu_{\rm tip} = \varepsilon_{\rm F} + eV/2$ and $\mu_{\rm sub} = \varepsilon_{\rm F} + eV/2$, enters in the leads self-energies via the replacement $E \to \omega \pm eV/2$. Finally, the current can be calculated at finite V at any of the leads i as

$$I_i = \int_{-\infty}^{\infty}\frac{d\omega}{2\pi}\Big\{\Sigma^<_i(\omega)G^>(\omega) - \Sigma^>_i(\omega)G^<(\omega)\Big\}, \tag{4.47}$$

while the bias-dependent conductance is found by numerical differentiation of I_i with respect to the bias.

In concluding this section it is informative to discuss the expected magnitude of the

inelastic contribution to the conductance with respect to the elastic one. The ratio between two such contributions essentially corresponds to the ratio between the interacting and the non-interacting ($J_{sd} = 0$) Green's functions. A simple calculation shows that the unperturbed Green's function differs by a factor of Σ_{int}/Γ from the fully interacting one. In the previous section it was shown that to the second order self-energy goes as $\Sigma_{int}^{(2)} \sim \alpha J_{sd}$. Therefore, to the second order, the ratio between the elastic and inelastic contributions to the conductance turns out to be proportional to the dimensionless factor $\alpha(J_{sd}/\Gamma) \sim (J_{sd}/\varepsilon_0)^2$. Analogously, the third order contribution will account for a factor $\alpha^2(J_{sd}/\Gamma)$. With this at hand and by using the experimental parameters [see Table (5.3)], one can conclude that the contribution originating from the second order expansion will be significant, while that from the third order will be small.

Chapter 5

Examples of spin-flip scattering in STM experiments

All the theoretical machinery developed so far will now be put to work to describe a recent range of experiments, where an STM tip probes a magnetic nanostructure deposited on an insulating surface. Results will be presented by looking at increasingly complex situations, where increasingly higher levels of theory are necessary.

5.1 Density Functional Theory Calculations

First-principles total energy and force calculations were carried out using the projected augmented-wave (PAW) method [114] as implemented in the Vienna Ab-initio Simulation Package (VASP) for Fe, Mn and Co on a CuN substrate. VASP is a package for performing atomic relaxation using a plane wave basis set. Exchange and correlation effects have been taken into account by using the local spin-density approximation (LSDA). In order to recreate the correct parameters for strongly correlated materials, which exhibit highly localized d-shell electrons (as in this work) the LDA+U method has been employed. This accounts for the on-site Coulomb interaction within the localized d-shell electrons. In the following calculations, an energy cutoff of 400 eV is used in the plane-wave basis

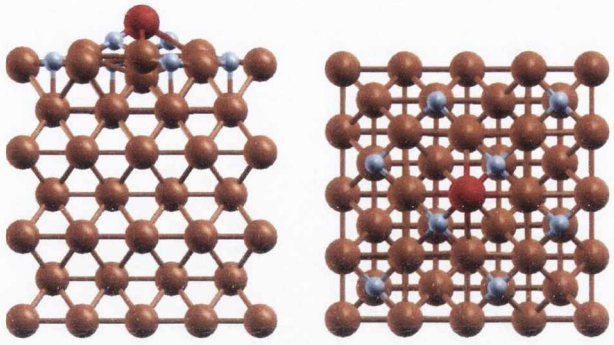

Figure 5.1: In-plane (left panel) and out-of-plane (right panel) structure diagram of the relaxed CuN substrate with magnetic transition metal atom (red) sitting on top of a Cu atom (brown) and between two N atoms (blue).

construction and the energy convergence criteria is 10^{-5} eV. The crystal structure was optimized until the forces acting on atoms were less than 0.01 eV/Å. For the Brillouin-zone integration, a $2 \times 2 \times 1$ Monkhorst-Pack mesh and Gaussian-smearing approach with σ=0.015 eV were used.

As mentioned, the system of interest consists of a 3d transition metal atom coupled to a Cu substrate with a separating layer of N (i.e. through a CuN monolayer). The lattice constant for the Cu fcc lattice was taken as the experimental value of 3.61Å since the LSDA is known to over-bind. The lowermost layer of Cu atoms was fixed during the relaxation process to their bulk positions. Five layers in the CuN slab are enough to simulate the CuN surface and subsequent increasing of the number of layers does not significantly affect the atomic structure and both the electronic and magnetic properties. The relaxed structures for 3d transition metal atoms Fe, Mn or Co on CuN is illustrated in Fig. 5.1. In particular a view from both the in-plane and the out-of-plane perspective is shown. It is notable how the particular 3d atom sits on top of a Cu atom, which is then pushed towards the bulk (note that the relaxation for the three different atoms of Fe, Co and Mn remains unchanged). In the following it will be shown how the various model parameters (substrate couplings, spin-exchange energies, magnetic anisotropies etc.) that were introduced in the last chapter are estimated from DFT calculations.

Atom	M (Exp. Fit)	M (LSDA)	M (LDA+U)
Co	3.0	2.2	2.4
Fe	4.0	2.9	3.1
Mn	5.0	3.9	4.2

Table 5.1: Values of magnetic moment, M, in units of μ_B) projected over the single 3d atoms from experiment [5, 6] and from theory. Results are repeated calculated with both the LSDA and LDA+U for $U = 5$eV

5.1.1 Atomic magnetic moment and density of states

The magnetic moment projected over the localized 3d atom atop the CuN substrate is calculated by using the PAW method for both the LSDA and the LDA+U. The magnetization, M, was found in each case to be mostly concentrated on the localized atom with little to no contribution coming from the underlying Cu or N atoms. Table 5.1 shows the corresponding values of M for each atom. In the case of LDA+U a value of $U = 5$eV was used. This value is in agreement with similar works for these materials [115]. It is clear that the LDA+U method recreates the experimental values of M more accurately than the LSDA. This is to be expected since the system in question involves highly localized d-shell electrons which, as outlined in Chapter 2, is well described by the LDA+U method.

The density of states (DOS) resolved over the s and d orbitals of each of the three atoms is shown in Fig. 5.2, for the LDA+U method. It is clear that the magnetization originates from the d-shell electrons because the majority to minority carrier splitting is greatest in this case. It is also worth noting that the s-level contribution to the total DOS is weak compared to that of the d-electrons. This reaffirms the approximation made throughout this thesis that the density of states for current carrying electrons (i.e. s-electrons) about the Fermi level is small enough to ensure that the perturbation parameter ρJ_{sd} as introduced in the last chapter remains below 1. As a final point, an approximate value for the exchange coupling parameter J_{sd} can be extracted from the spin-polarized splitting of the s-electron DOS, as this determines how the conduction electrons react to

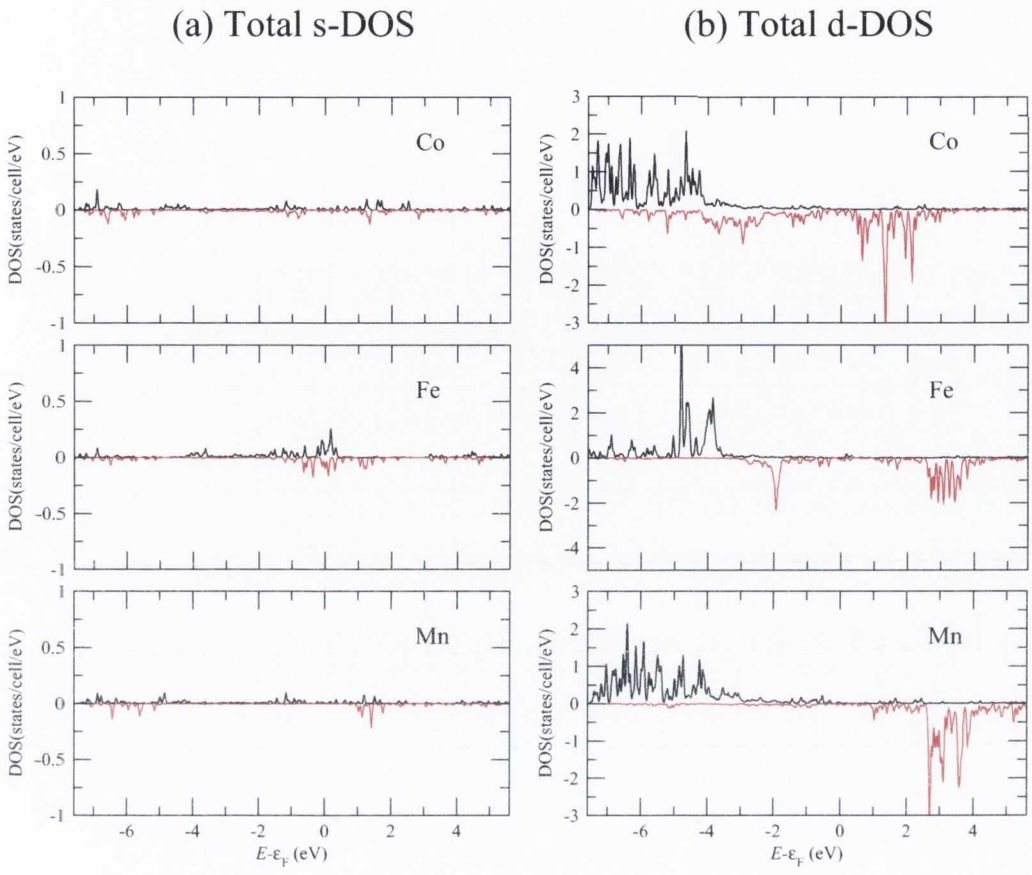

Figure 5.2: Total s (a) and d (b) projected DOS for the magnetic atoms Co, Fe and Mn. The majority DOS is shown in black while the minority is shown in red (and negative).

the magnetic moment of the localized d-shell electrons. Although the splitting can also be mediated by other factors, it is assumed that the coupling between the d and s-shell electrons has the strongest impact on the splitting of the DOS. This is a rather crude approximation but nonetheless offers an insight in to the order of magnitude of J_{sd}. This approximation has also been applied by Lucignano *et al.* [116]. The broadening of the main peaks in the s and d-density of states can also serve as a crude approximation to the coupling parameter between atom and substrate Γ_{sub} introduced in the previous chapter.

Atom	$\Delta E_A(z-x)$	D (Theory)	D (Exp.)
Co	+0.79meV	+0.35meV	+2.75meV
Fe	-4.95meV	-1.24meV	-1.55meV
Mn	-2.60meV	-0.42meV	-0.04meV
Fe-Cu	-17.26meV	-4.32meV	-

Table 5.2: Values of the MAE in meV for Co, Fe, Mn and a Fe-Cu dimer on CuN. The corresponding values for the axial anisotropy parameter D is compared to the equivalent found from experiment [5, 6].

5.1.2 Magnetic anisotropy

The magnetic anisotropy energy (MAE) can be calculated by switching on the spin-orbit interaction in the calculation performed with VASP. This is performed with spin pointing along specific axes in order to acquire an approximation to the axial and transverse anisotropy terms D and E respectively. Since in general the value for E is quite small, it is not informative to approximate its value using DFT since it is outside the bounds of the VASP accuracy ($\sim$ meV). To that end, the larger and more significant axial anisotropy D will only be investigated.

From the previous chapter, the energy splitting due to the axial anisotropy was defined as $\Delta E = DS_z^2$. Therefore, to find an approximation to this value, one must calculate the total energy E_A with spin pointed along the x axis and the z axis. The difference between these two values $\Delta E_A(z-x)$ gives the total axial MAE. The value for D is then found by normalizing $\Delta E_A(z-x)$ to the value S^2 where S is the total (nominal) spin magnetic moment of the localised atom. Table 5.2 shows the comparison between the experimental and theoretical calculations for D for the single atoms of Co, Fe and Mn. Whereas the sign of D is recreated by the VASP calculation (which indicates hard (-) or easy (+) axis of anisotropy), the exact value is poorly recreated for Co and Mn but quite well for the Fe atom. The reason for the disparity in the case of Co and Mn is unclear however a similar result was found in previous DFT calculations for the MAE [117].

In addition to the three single magnetic atoms, the MAE was also calculated for a dimer consisting of Cu and Fe in light of an experiment performed by Loth *et al.* [59],

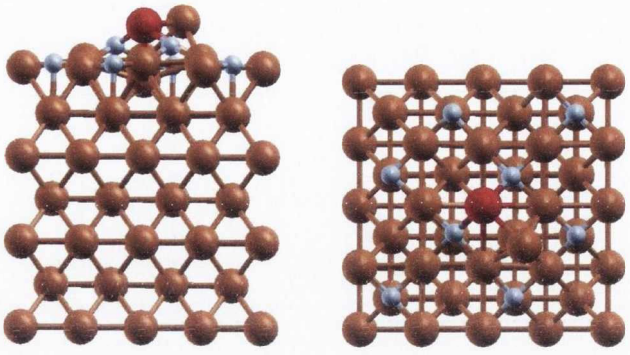

Figure 5.3: In-plane (left panel) and out-of-plane (right panel) views of the relaxed CuN substrate with an Fe (red) - Cu (brown) dimer sitting on top of a Cu substrate decorated by a single layer of N (blue)

which investigated the spin relaxation time of the dimer. Loth *et al.* showed experimentally that the presence of a Cu atom on the surface drastically increases the anisotropy of the Fe-Cu dimer and therefore results in a stable spin orientation with long relaxation time [59]. It was suggested that the Cu atom has a zero net polarization and therefore the Fe-Cu dimer acquires the spin of the single Fe atom on CuN, $S = 2$. An exact experimental value for the axial and transverse anisotropy terms could not be found because the axis of anisotropy could not be determined. Therefore, a calculation of the MAE for the Fe-Cu dimer would shed some light on the situation.

Figure 5.3 shows the relaxed structure for the Fe-Cu dimer on the CuN substrate, again with 5 layers of Cu where the bottom layers were fixed during the relaxation. Indeed, the total magnetization associated to the Cu atom in the dimer was found to be zero and that of Fe was $3.2\mu_{\mathrm{B}}$. This confirmed the experimental findings. From table 5.2 it was found that $D = -4.32$meV, i.e. that the MAE of the dimer is roughly 3.5 times larger than that of the single Fe atom. This also agrees with what is found experimentally, in that the addition of the Cu atom drastically increases the MAE of the system. It will be shown later in the chapter that the 3.5 fold increase (along with other assumptions) will recreate well the experimental dependence of the spin-relaxation time on the magnetic field applied to the Fe-Cu dimer. Due to the observed increase in magnitude of the axial anisotropy, it was informative to investigate the corresponding change in the transverse anisotropy E

as its magnitude in this case might be significant enough that a VASP calculation could be trusted. E was estimated from the change in total energy when the spin is pointing along the x and y directions i.e. $\Delta E_A(y-x)$. Indeed a value of $E = 0.54$meV was found which is well within the accuracy of a VASP calculation with spin-orbit correction. This also agrees with the direction of transverse anisotropy found for a single Fe atom [5].

5.2 Mn mono-atomic chains on a CuN surface: second-order theory

Having shown how to estimate the various model parameters from DFT, the discussion continues by firstly looking at the SP-IETS spectrum of Mn mono-atomic chains of different lengths deposited on a CuN surface and probed, in a low current mode, by a non-magnetic STM tip [9]. The main features of the experiments can be captured by the second order perturbation theory for non-magnetic leads and equilibrium spin populations. In Table 5.3 all the parameters needed for the simulations are listed together with their assigned values. These have been either inferred from experiments (Exp) [9] or have been estimated from density functional theory (DFT) calculations performed in this work. The local Mn spin is set to be 5/2, as proposed in the original experimental works [5, 9], confirmed by DFT calculations and in agreement with the DFT analysis of Ref. [34]. The spin-spin coupling parameter J_{dd} corresponds to an anti-ferromagnetic order between the neighbouring Mn spins, a feature verified in the experimental conductance spectra. The lead on-site energy is suitably set to zero and simply defines the reference potential. One also notes that the value for J_{sd} is determined from theory (splitting in the s-electron DOS) to be of the order of 500 meV. The Fermi functions of the leads is evaluated at the small temperature of 0.6 K. This allows one to include minor thermal smearing of the electron gas in the leads and consequently of the conductance profile. Finally one notices that the scattering region is expected to be significantly more strongly coupled to the

Quantity	Symbol	Value	Origin
Atomic Spin	S	$\frac{5}{2}$	Exp.
Temperature	T	0.6 K	Exp.
d-d exchange	J_{dd}	+6.2 meV	Exp.
s-d exchange	J_{sd}	+500 meV	DFT
Fermi Energy	E_{F}	0 meV	DFT
Lead hopping integral	γ_0	10000 meV	DFT
Channel (s-state) on-site energy	ε_0	1000 meV	DFT
Substrate-channel hopping	$\gamma_{\mathrm{sub-S}}$	500 meV	DFT
Axial anisotropy	D	-0.037 meV	Exp.
Transverse anisotropy	E	0.007 meV	Exp.

Table 5.3: Empirical parameters used in the numerical simulations presented in this work and their assigned numerical values and origin. "Channel" here means the scattering region.

substrate than to the tip.

Figure 5.4(a) shows the calculated conductance spectra normalized against the elastic contribution, G_{el}, [this is the conductance calculated for $\Sigma_{\mathrm{int}}(E) = 0$] for N-atom long Mn chains ($N \leq 4$) in no external magnetic field. This is in favourable comparison with the experimental findings as shown in Fig. 5.4(b). The most obvious feature is the presence of a number of conductance steps characteristic of a specific chain, which appear at well-defined biases. These correspond to critical voltages where a magnetic excitation becomes possible. Such an excitation opens an additional conducting channel (inelastic) and the conductance increases. Note that in general one does not necessarily expect the conductance to increase at the excitation bias threshold. In fact, in the case of inelastic scattering to phonons both conductance enhancements and suppressions have been observed, with the latter originating from the suppression of the elastic channel following the opening of the inelastic one. In general, however, SP-IETS experiments show a conductance increase.

From the figure one observes that the relative conductance increase due to the inelastic contribution is of the order of 1/4 (for $N = 2$, where the amplitudes of the spin matrix elements of the self-energy are approximately unity). For the given choice of parameters the scaling factor $(J_{\mathrm{sd}}/\varepsilon_0)^2$ is 1/4, so that precisely a relative conductance step of 1/4

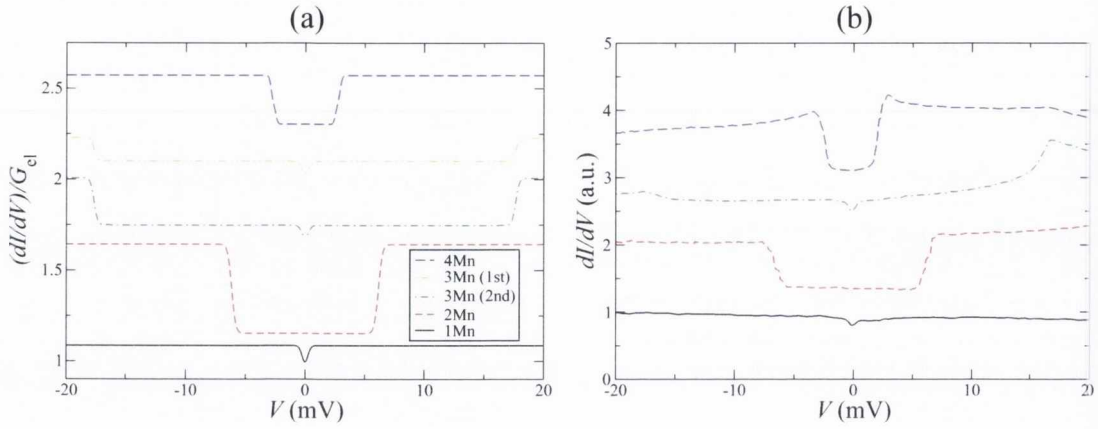

Figure 5.4: Theoretical (a) and experimental (b) conductance spectra for Mn chains of different lengths N. The various spectra, except for $N = 1$, are offset for clarity. The tip is placed above the second atom of the chain for chains with $N > 2$ and also over the first atom in the case of $N = 3$. One notices the strong dependence of the spectra on the chain parity.

is expected. Such good agreement constitutes a strict validity test for the theory and demonstrates that the perturbative expansion is the right tool to tackle these problems. In the case of $N = 3$ and $N = 4$ the spectrum is calculated for the STM tip placed above the second atom in the chain, but in Fig. 5.4(a), for $N = 3$, results obtained by placing the tip above the first atom are also shown. Notably the spectra in the two cases are relatively different as the size of the conductance step at around 17 meV seems to depend on the specific atomic site probed by the tip. A similar occurrence is seen for $N = 4$.

When the calculated conductance profiles are compared with the experimental ones of Fig. 5.4(b) a good qualitative agreement emerges. In particular one notices the intriguing dependence of the conductance profile over the parity of the chains, with chains comprising an odd number of atoms (odd chains) exhibiting a conductance dip at around $V = 0$, which is absent for even chains. It is worth noting, however, that the spectra for $N = 3$ and $N = 4$ contrast slightly with the experimental spectra, which are asymmetric with respect to the bias and also exhibit some slope at the conductance steps. It will be argued later in the chapter that such minor deviations are simply due to fine features in the density of states. In order to recreate the conductance profile of the trimer (3Mn), an

additional ferromagnetic second nearest-neighbour interaction between the local spins at the edge of the chain must be included in the model [23]. The magnitude of this additional exchange parameter is approximately half of that of J_{dd}. The inclusion of such a second nearest-neighbour coupling constant changes the position of the conductance step from a second excited state at 27 mV to a first excited state at 16 mV. This correction is also included in the calculations for $N = 4$, again giving good agreement with experiments.

Going into more detail of the conductance spectra, the case of odd chains and their zero-bias conductance anomaly is first discussed. The ground state of each odd chain has a net total spin $S_{\mathrm{tot}} = 5/2$. This is affected by the transverse and axial anisotropy, which lift the ground state degeneracy and allow a transition between the ground state and the first spin-flip excited state to occur. The excitation of such a transition results in a conductance step at a voltage corresponding to the transition energy. Since the anisotropy energies are small (see Table 5.3), the excitation energy is small as well and the feature in the conductance profile appears near V=0. In contrast the even chains do not show any zero-bias excitation, since the ground state is a singlet and does not carry a magnetic moment. This is a direct proof that the magnetic interaction between Mn ions is anti-ferromagnetic. Should this have been ferromagnetic, even chains would also have shown zero-bias anomalies.

As mentioned above the conductance steps encountered at around V=0 correspond to spin-flip events, i.e. to electron scattering processes that produce the transition $|m = 5/2\rangle \rightarrow |m = 3/2\rangle$ (m is the magnetic quantum number) but that also preserve the total spin $S_{\mathrm{tot}} = 5/2$. The first net spin changing transition occurs for $N = 2$ and corresponds to the large conductance step found at $V = J_{\mathrm{dd}}/e = 6.2$ mV. This is investigated in more detail in Fig. 5.5, where the dimer's spectrum calculated when a magnetic field is applied along the z-direction is also included. The effect of the magnetic field is that of splitting the single excitation line into three distinct conductance steps. In this case in fact the anti-ferromagnetic dimer has a singlet (S_{tot}=0) ground state and a triplet (S_{tot}=1) first

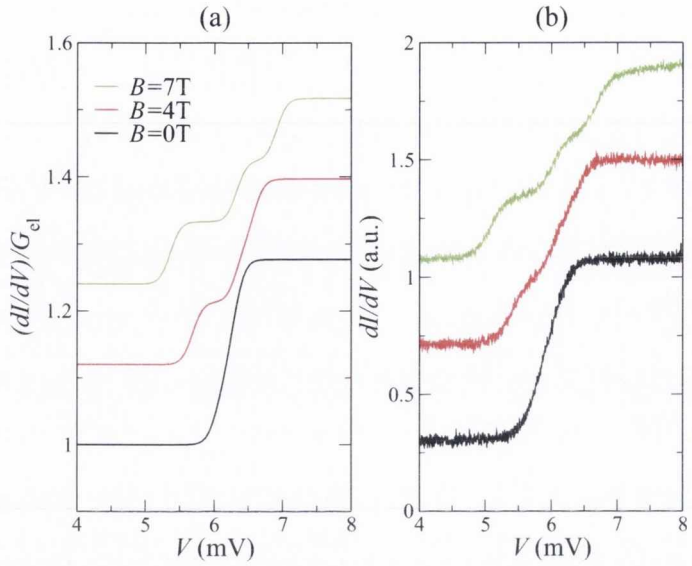

Figure 5.5: Theoretical (a) and experimental (b) conductance spectra for the N=2 chains in a finite external magnetic field. For $\mathbf{B} \neq 0$ we note a splitting of the conductance steps, corresponding to the Zeeman split of the final triplet excited state. This is observed in the experiments of reference [9], which are reported in panel (b).

excited state. Therefore, an excitation from the ground state to the first excited state changes the net spin of the dimer. When a magnetic field is applied the degeneracy of the triplet excited state is lifted and excitations having the three Zeeman-split levels as final states are possible. This produces the three-fold splitting of the conductance steps as seen to agree well with experiment in Fig. 5.5.

Figure 5.6 shows the conductance spectrum for the trimer (N=3). This chain exhibits similar trends to those found for the dimer as a magnetic field is applied, i.e. there is a Zeeman split of the zero-field conductance steps. From the figure one may notice that for both the theoretical (a) and experimental (b) data there is a shift of the principle step to lower voltages as the magnetic field is increased. It is recalled here that in order to recreate the conductance profile of the trimer, an additional ferromagnetic second-nearest-neighbour interaction must be included in the model [23].

In all the spectra investigated the most striking agreement with the experiments concerns the correct prediction of the SF-IETS excitation voltages. In particular not all the

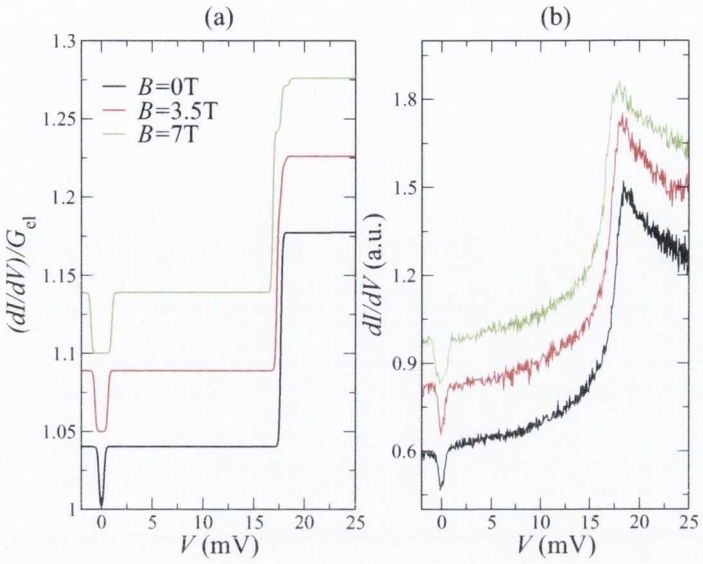

Figure 5.6: Theoretical (a) and experimental (b) conductance spectra for the $N = 3$ trimer at different magnetic field. We notice the shift of the first conductance step transition to lower voltages as the magnetic field increases. This is in good agreement with STM experiments of reference [9], which are reproduced here in panel (b).

possible spin excitations feature in the $\mathrm{d}I/\mathrm{d}V - V$ curve as a result of the spin-selection rules. A careful analysis of the inelastic process, as outlined in the first section, reveals why some excitations occur and why some other do not. In particular it is noted that the proper selection rules for the transitions are governed by the prefactor in the self-energy, namely $|\langle m|S^i|n\rangle|^2$ [Eq. (4.27)]. This effectively selects which excitations are more probable to occur. For example, the full energy spectrum of the trimer has $6^3 = 216$ eigenvalues but only a small portion of these eigenvalues will contribute significantly to the scattering self-energy. Consequently only a few transitions will have influence on the conductance spectrum. This for instance explains why the first conductance step of the dimer is considerably larger than that of other chains of different lengths. In fact our calculations show that a transition from the singlet ground state (S=0) to any of the triplet excited states (S=1; m= -1, 0, +1) has equal probability. This results in a conductance step which is approximately three times larger than any single spin-flip event that occurs in an odd chain.

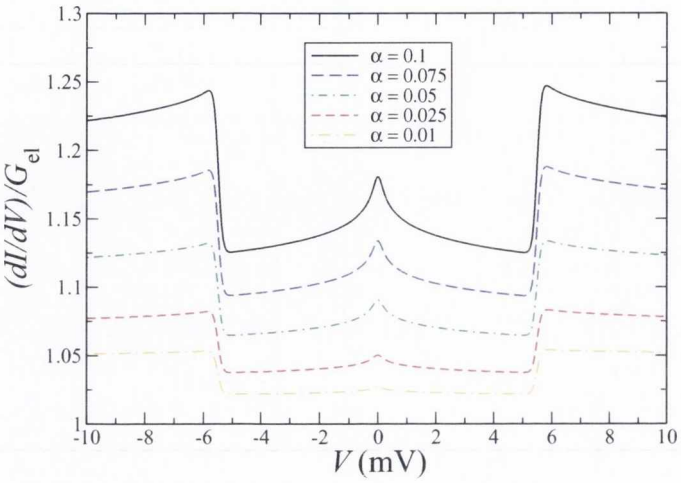

Figure 5.7: Normalized conductance spectrum for Co ($S = 3/2$) on CuN as $\alpha = \rho J_{sd}$ is increased. Note the emergence of a Kondo resonance at zero-bias, i.e. at the Fermi level. The curves are arbitrarily displaced for clarity.

5.3 Kondo effect and improved lineshape: third order calculations

In order to illustrate the effects of continuing the perturbation expansion to third order the conductance spectra of Co and Fe atoms deposited on the CuN surface will be discussed. This section therefore aims at rationalizing the experiments described in reference [10], where both Co and Fe ions were investigated by low temperature STM spectroscopy. Intriguingly in the experiment it is possible to place the two ions at different distances from each other. Thus one can investigate how the spectrum of the Kondo active Co is affected by the presence of Fe and, viceversa, as the spectrum of Fe is affected by the presence of Co.

Figures 5.7 and 5.8 show the calculated conductance spectra respectively for single Co and single Fe atoms on CuN as the dimensionless parameter $\alpha = \rho J_{sd}$ is varied (note that the spectra are normalized relative to the elastic conductance, G_{el}). The α parameter is the coupling constant of the perturbation expansion as discussed extensively in the

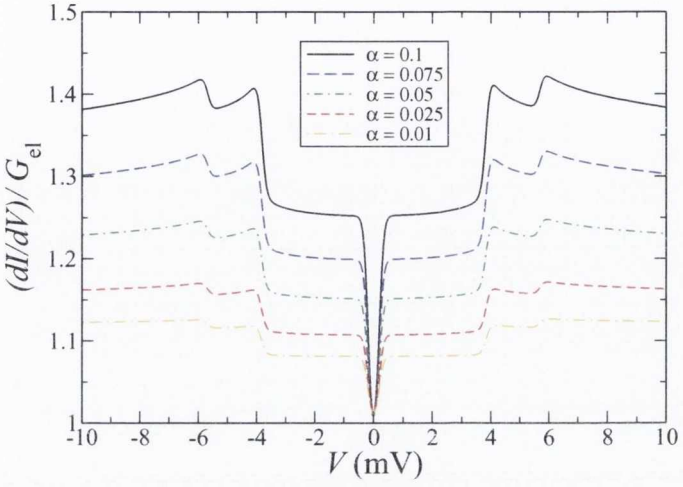

Figure 5.8: Normalized conductance spectrum for Fe ($S = 2$) on CuN as $\alpha = \rho J_{\rm sd}$ is increased. Note the transition from a constant conductance at the inelastic steps to a conductance that logarithmically decays after the excitation. The curves are arbitrarily displaced for clarity.

previous chapter. This is varied by altering the coupling of the adatom to the substrate, i.e. by changing $\gamma^{\rm s-a}$, which translates in modifying the value of the adatom density of states at the Fermi level.

This time the parameters of the simulation are set as follows. The level broadening due to the coupling to the substrate (the one coupled to the tip is neglected) is set at $\Gamma_{\rm sub-S} = 0.1\,{\rm eV}$ for both Co and Fe. In order to ensure consistency in the approximations $[\Gamma_{\rm sub-S} = (\gamma_{\rm sub-S})^2/W]$ $\gamma_{\rm sub-S} = 1.5$ eV is set with the substrate bandwidth being $W = 20$ eV. One then chooses $\varepsilon_0 = 1\,{\rm eV}$ to fulfill the criterion $\varepsilon_0 \gg \varepsilon_{\rm F} = 0$. The magnitude of $J_{\rm sd}$ for both Fe and Co is held constant at 0.5 eV (the same value used for the Mn chains). Finally the axial and transverse anisotropy parameters are taken from the experimental fits of Refs. [7, 9] and are $D_{\rm Co} = 2.75$ meV, $E_{\rm Co} = 0$ meV, $D_{\rm Fe} = -1.53$ meV and $E_{\rm Fe} = 0.31$ meV, while the adsorbed atoms spins are $S_{\rm Co} = 3/2$ and $S_{\rm Fe} = 2$.

The discussion begins with the case of Co. The full diagonalization of the $H_{\rm sp}$ ($S_{\rm Co} = 3/2$) Hamiltonian gives a set of four $(2S_{\rm Co}+1)$ eigenvalues and eigenvectors. In particular the presence of a hard-axis anisotropy results in the following energy manifold $\varepsilon_m^{\rm Co} =$

$\{0.69, 0.69, 6.19, 6.19\}$ meV, i.e. in a doubly degenerate ground state. It is then found that transitions between the degenerate ground states become allowed only on inclusion of the third order term in Eq. (4.32). This is because of the selection rules imposed by the theory through the matrix elements $\langle m|S^i|n\rangle$. Such a transition appears in the spectrum of Fig. 5.7 in the form of a zero-bias Kondo peak, whose intensity increases as the value of α gets larger. The same feature is completely absent if one truncates the perturbation expansion to the second order. Note that the third order contribution to the interacting self-energy scales as α^2, while the second order one goes as α. Hence it follows that an increase of the adatom density of states (an increase of α) promotes the third order contribution to the self-energy. As such the enhancement of the Kondo peak intensity is directly related to the relative growth of the logarithmic divergence of $\Sigma^{<}_{\text{int}}$ in Eq. (4.32). The same logarithmic divergence produces a second distinctive feature in the $\mathrm{d}I/\mathrm{d}V$ traces, namely the rise of the conductance following an inelastic excitation. This can be seen, for instance, in the conduction step at 6 meV. Such a step originates from the transition from the ground state to the first excited state. One may then note that first the conductance rises sharply at the voltage corresponding to the excitation energy and then slowly decays. Although the agreement between the results and experiments will be returned to, one notes here that such conductance traces are qualitatively similar to those found in the STM experiments of Refs. [7, 10], i.e. both the zero-bias Kondo peak and the increase in conductance at the inelastic transition voltages are observed.

The results for Fe are presented next in Fig. 5.8. This time H_{sp} ($S_{\text{Fe}} = 2$) has the five eigenvalues namely $\varepsilon_m^{\text{Fe}} = \{-6.30, -6.12, -2.46, -0.60, 0.18\}$ meV, so that the ground state is non-degenerate. At zero magnetic field all the transitions allowed by the third order expansion are resolved in the conductance traces. In this case there is no zero-bias Kondo peak as the ground state is non-degenerate. Near to the zero-bias region a conductance dip is observed, which corresponds to an inelastic transition between the first two lower lying spin states. Furthermore, as in the case of Co, the presence of a

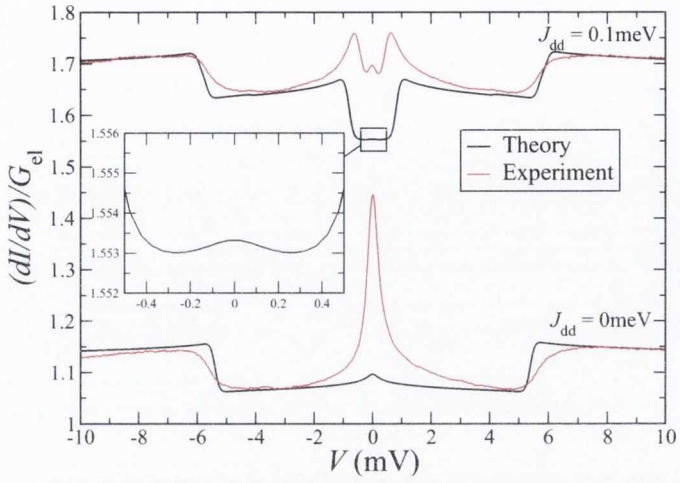

Figure 5.9: Normalised conductance spectrum for a Co adatom on CuN when it is exchange coupled to Fe as J_{dd} is increased ($J_{dd} = 0$ means that there is no magnetic coupling between Co and Fe). Note how the Co Kondo peak splits as the Fe atom acts as an effective magnetic field. The insert zooms in the zero-bias region. The calculated spectra are in black, while the corresponding experimental data from Ref. [10] are in red.

logarithmic conductance is found as an increase at the inelastic steps in the $\mathrm{d}I/\mathrm{d}V$ traces (for instance note the well pronounced one at ~ 4 mV). Again, since such a feature is directly related to the third order contribution to the interacting self-energy, it gets more pronounced as α is increased. The same feature is observed experimentally in all non-Kondo active adatoms, demonstrating the good level of description provided by the third order expansion. Note that such a behaviour was previously explained by invoking a non-equilibrium population of the Fe spin states [27]. This explanation however conflicts with the fact that the same effect is seen also for low currents [9], namely when the adatom spin state resides close to the equilibrium. Therefore, the experimental data is re-interpreted as the manifestation of third order Kondo corrections to the spin-flip inelastic tunneling spectra. This will be discussed further at the end of this chapter.

As a final test for the third order self-energy an exchanged coupled Co-Fe dimer is considered, a situation already investigated experimentally in Ref. [10]. For small, but finite, values of J_{dd} one notices a change in the $\mathrm{d}I/\mathrm{dV}$ traces of both Co and Fe, which

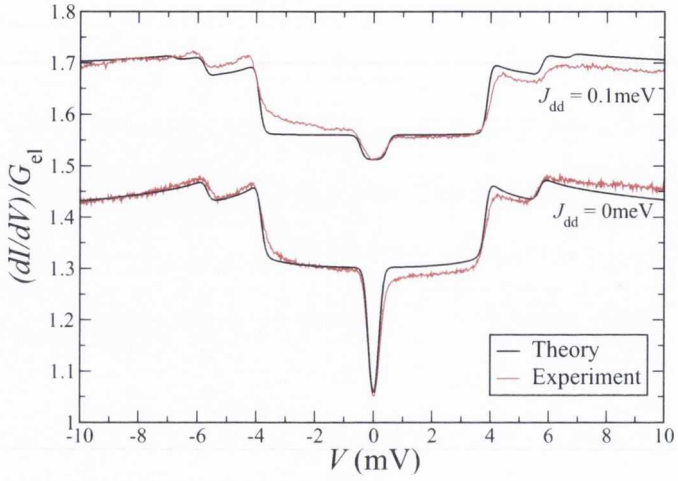

Figure 5.10: Normalised conductance spectrum for a Fe adatom on CuN when it is exchange coupled to Co as J_{dd} is increased ($J_{\mathrm{dd}} = 0$ means that there is no magnetic coupling between Co and Fe). Note that the intensity of the conductance step at 0.18 mV decreases with increased exchange coupling. The calculated spectra are in black, while the corresponding experimental data from Ref. [10] are in red.

becomes more pronounced as J_{dd} increases. Figures 5.9 and 5.10 show the conductance spectra calculated in the two situations where the tip is either positioned over Co (Fig. 5.9) or Fe (Fig. 5.10). Again a value for $\alpha = \rho J_{\mathrm{sd}} = 0.1$ is used. In the figures the experimental data [10] is superimposed for comparison.

In this situation one notices a change in the dI/dV traces of both Co and Fe as they are brought close together, i.e. as J_{dd} increases. For Fe both the conductance steps around zero-bias and that at 0.18 mV decrease in intensity with increasing J_{dd}. In contrast, Fe itself acts as an effective magnetic field that splits the zero-bias Kondo resonance present in the spectrum of Co. Both these effects are observed in the experiments of Ref. [10]. Notably Fe does not simply act as a source of magnetic field on Co, as seen in the inset of Fig. 5.9 for $J_{\mathrm{dd}} = 0.1$ meV. In the figure one can clearly observe an additional Kondo peak emerging at zero-bias in between the two principally split peaks. This is a unique feature of the exchange coupling between Co and Fe. In fact the exchange coupled Fe-Co dimer possesses $(2S_{\mathrm{Co}}+1)\times(2S_{\mathrm{Fe}}+1) = 20$ eigenvalues and additional allowed transitions

appear at each of the atomic sites. For instance for large J_{dd} the zero-bias region of the Co spectrum becomes completely dominated by a conductance dip. This originates from the opening of a spin transition between the ground state at -5.686 meV and the first excited state at -5.379 meV. Such a transition, absent for the isolated Co adatom, has a spectral intensity much larger than that of the Kondo resonance, which therefore disappears from the spectrum.

A comparison will now be made between the theoretical data and the corresponding experimental spectra [10]. Notably, whereas the calculated spectrum of Fe is in excellent quantitative agreement with the experimental one, the same cannot be said for that of Co, which only reproduces the experimental features at a qualitative level. In particular the experimental Kondo resonance is much more pronounced than the calculated one (note that the parameter α has been set in order to reproduce the experimental step in the spectrum at $\sim$ 4 mV). At this point one can only speculate on the reasons for such a disagreement. Firstly, the *s-d* model is valid only in the limit where the tunneling matrix element t is small with respect to the adatom charging energy U. This is the case in which a Hubbard-like model can be mapped onto the *s-d* one [118]. Such a limit might not be satisfied for Co on CuN. In the event of a large t/U ratio a more rigorous 2-body (Hubbard-like) approach needs to be employed to describe electrons in the localized $d-$states [119, 120], in the conducting $s-$states [35] and in situations with anisotropic exchange coupling $J_{\mathrm{sd}}^{x,y} \ll J_{\mathrm{sd}}^{z}$ [121]. It must be pointed out that in the works just mentioned a more accurate reproduction of the Kondo peak was revealed by using the non-perturbative computational method called numerical renormalization group (NRG).

5.4 Additional lineshape features: Spin-pumping

5.4.1 Spin relaxation time

In this section the various conductance lineshape features that occur due to both non-equilibrium spin pumping and a spin polarized tip will be investigated. Firstly, however, the effect of the coupling environment on the localized spin will be analyzed. This will allow a calculation of an important parameter called the spin relaxation time, T_1. This quantity defines the time that it takes for the localized spin to relax back to its ground state after being excited. In particular the magnetic field dependence of T_1 can be favourably compared with the findings of Loth *et al.* [59], who, in a ground breaking paper, calculated T_1 explicitly for an Fe-Cu dimer, which exhibits a large magnetic anisotropy on a CuN substrate. This property results in a correspondingly large T_1 and spin memory.

In order to find an expression for T_1, Eq. (4.43) for the bias dependent transition rate from an initial state l to a final state n is recalled. In particular the special non-bias-dependent case is investigated where the effect of the tip is neglected and the localized spin is only coupled to the substrate (sub). The transition rates are then

$$W_{nl} = -4\frac{(\rho J_{\mathrm{sd}})^2}{\Gamma}\sum_i \zeta(\Omega_{ln})|S^i_{nl}|^2[\Gamma_{\mathrm{sub}}]^2, \tag{5.1}$$

where $\zeta(x) = x/(1 - e^{-x/(k_BT)})$. This represents the excitation and relaxation of the localized spin due to an exchange interaction with electrons that are coming and going from the substrate. The inverse of this quantity gives a characteristic decay time. As a result, the time it takes for an excited spin system to relax back to the ground state $n = 1$ is

$$T_1 = \Big[\sum_l W_{1,l}\Big]^{-1}. \tag{5.2}$$

The values for both the excitation energies Ω_{ln} and the spin matrix elements $|S^i_{nl}|^2$ are

evaluated by diagonalizing the spin Hamiltonian originally introduced in Eq. (4.14) and evaluating the resultant eigenenergies and eigenvectors. This Hamiltonian takes the following form

$$H_{\rm sp} = g\mu_B \mathbf{B}.\mathbf{S} + D(S^z)^2 + E[(S^x)^2 - (S^y)^2], \tag{5.3}$$

where g is the Lande g-factor, μ_B is the Bohr magneton and B is a magnetic field that can be applied in an arbitrary direction. The axial and transverse anisotropy terms are measured by D and E respectively.

The formalism for calculating T_1 will be tested against one of the few experiments (Loth *et al.* [14]) that achieved an accurate estimate of the spin relaxation time of a single localized spin. In this experiment a single Fe atom is placed on a CuN substrate (see section 5.1). An additional Cu atom is then placed in close proximity to the single Fe atom to form an FeCu dimer. It was shown from the DFT calculations described in section 5.1 that the Cu atom itself carries effectively no magnetization and therefore the spin polarization of the dimer is dominated by the Fe atom which generally carries a spin quantum number $S = 2$. A magnetic field of 7T is then applied along the easy axis of magnetization (the z axis). This breaks the spin degeneracy of the spin system. However it is found that the dimer does not reproduce the same conductance spectra of a single Fe atom in a magnetic field of 7T (see Ref. [5]). In the single atom case the first conductance step is found at approximately $V = 6$meV. For the case of the FeCu dimer however, the position of this conductance step is greatly increased to roughly $V = 16.7$meV. The proposed reason for this shift is that the proximity of Cu causes a strong increase in both the axial and transverse anisotropy energies, a result verified by the DFT calculations.

The advantage of such a high magnetic anisotropy lies in the resulting long spin relaxation time T_1 when the FeCu dimer magnetic moment is excited out of its ground state. The relaxation mechanism for a spin $S = 2$ system with large axial and transverse magnetic anisotropy subject to a magnetic field of 7T can be represented by the schematic

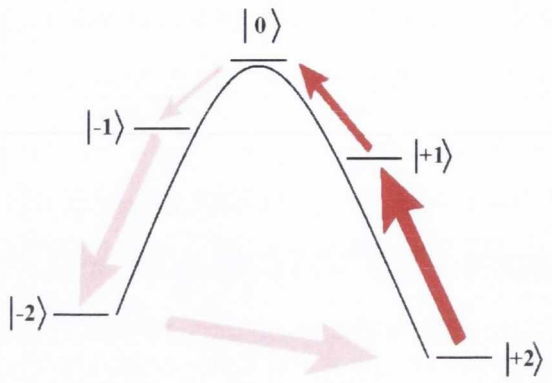

Figure 5.11: Spin relaxation mechanism for a spin $S = 2$ system. When excited above V_{thresh} the spin rapidly decays to the low lying states of $|+2\rangle$ and $|-2\rangle$. The spin relaxation time T_1 is then defined as the time taken for the decay from $|-2\rangle$ to $|+2\rangle$.

in Fig. 5.11. Under such circumstances the spin eigenvalues m_s can be considered an approximately good quantum numbers so that there is very little mixing between the spin states. As such, the ground state spin is approximately $|+2\rangle$ with first excited state being close in energy to the ground state with an eigenvector of approximately $|-2\rangle$. However, since there is a negligible spin matrix element $|S^i_{nl}|^2$ between these two states, a transition is highly unlikely and there exists an energy barrier between the states. It can be seen that the first strong excitation occurs between the ground state and the 2nd excited state $|+1\rangle$. In the experiment by Loth *et al.* the spin system can be excited by applying a pump pulse that matches the difference in energy between the $|+1\rangle$ and the $|+2\rangle$ states. This is called the threshold voltage V_{thresh}. At this point the spin is excited and rapidly decays back to the two low-lying energy states of $|+2\rangle$ and $|-2\rangle$ at a speed, which is undetectable with current measurement devices. The quantity T_1 is then defined as the time that is needed for the spin to relax from $|-2\rangle$ and $|+2\rangle$ which occurs at a much slower rate (measured times are $T_1 \sim 200$ns) and it is measured using a separate and weaker probe pulse.

An intriguing result is that the spin relaxation time of the Fe-Cu dimer initially increases as a function of the applied magnetic field but then at a certain point, $\sim 6T$, begins to decrease in value. In order to reproduce the result of this experiment, param-

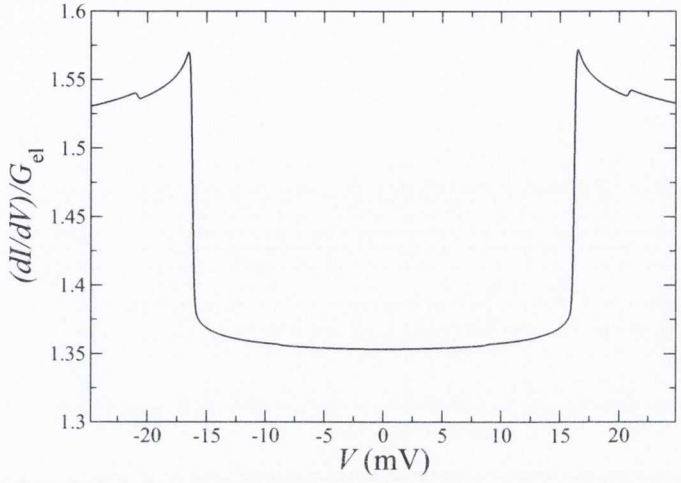

Figure 5.12: Conduction spectrum for the FeCu dimer. The first conductance step occurs at roughly 16meV. This large value is due to the increased axial and transverse magnetic anisotropy terms and represents the threshold voltage V_{thresh} at which the spin system becomes excited.

eters must be chosen that fit both the conductance spectrum for the dimer and the T_1 dependence on the magnetic field. The calculated conductance spectrum can be seen in Fig. 5.12. The values of the anisotropy used to recreate this spectrum were inferred from the corresponding values for the single Fe atom found empirically in Ref. [5], where the axial anisotropy was found to be $D_{\text{Fe}} = -1.55\text{meV}$ and the transverse $E_{\text{Fe}} = 0.31\text{meV}$. DFT results indicated that $D \sim 3D_{\text{Fe}}$. The assumption is then made that $E \sim 2E_{\text{Fe}}$ since DFT results for this parameter could not be trusted. Figure 5.13(a) shows the magnetic field dependence B of the eigenenergies of H_{sp} and 5.13(b) shows the calculated T_1 dependence on B, which closely matches what was found by Loth *et al.*. This simulation is based on the assumption that the applied magnetic field is tilted slightly with respect to the easy axis of anisotropy by roughly 5^o. It is mentioned in Ref. [14] that the easy axis of anisotropy coud not be determined experimentally but that such a deviation could take place. This effect is also key in interpreting the decrease of T_1 when $B > 6\text{T}$. The slight angular deviation results in an increased spin mixing between the two low lying states of approximately $|+2\rangle$ and $|-2\rangle$ [even though the energy separation between both states

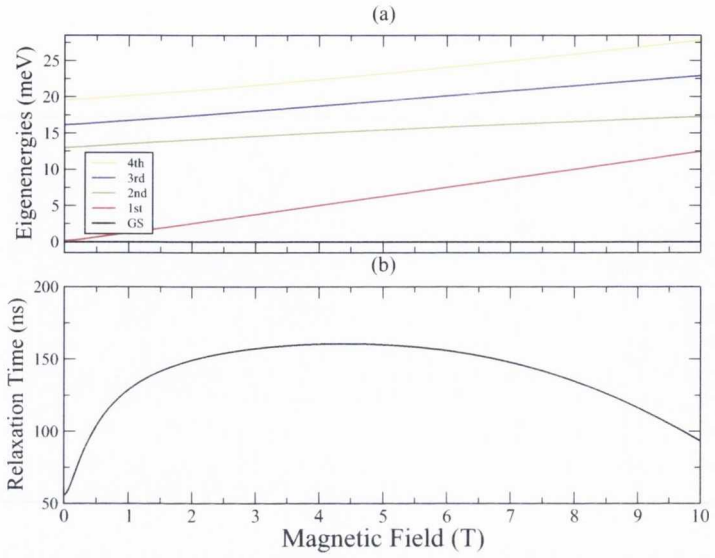

Figure 5.13: (a) Dependence of the eigenenergies of $H_{\rm sp}$ on the magnetic field B and (b) dependence of the spin relaxation time T_1 on B. In the latter it is seen that T_1 begins to decrease for $B > 6$T. This is due to an increased spin mixing between the two low lying spin states resulting from a non zero angle between the applied magnetic field and the easy axis of anisotropy.

is seen to increase linearly from Fig. 5.13(a)], which in turn increases the tunneling rate between each one. This ultimately results in quicker relaxation time between $|-2\rangle$ to $|+2\rangle$. One point of note however is that both the conductance and the T_1 dependence on B were fitted using a large Lande g-factor of roughly $g = 4$, which is drastically increased on the usual value of $g = 2$. This was also suggested in private communications with Sebastian Loth and the origin of which still remains unknown. DFT results will be performed in future works to try and ascertain the reason for the increased value of g.

5.4.2 Intense current density

Having seen the basic mechanism for spin relaxation due to the interaction between the spins and the conduction electrons from the underlying substrate, it is a natural step to study the non-equilibrium effects originating when a bias is applied between the two leads. The effects originating from driving the spin system out of equilibrium with an electronic current will now be investigated. This attempts at explaining the experiments reported in

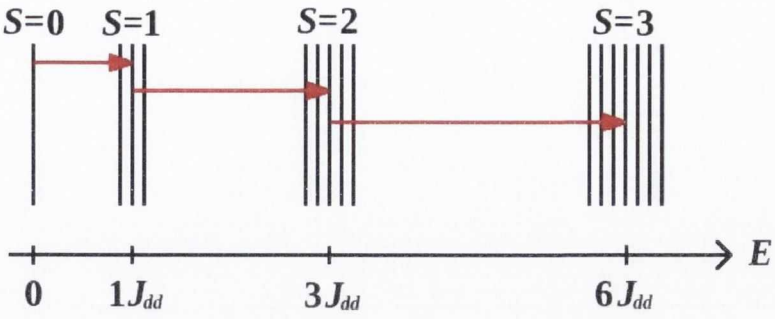

Figure 5.14: Excitation spectrum for an antiferromagnetically exchanged coupled Mn dimer deposited on CuN. The ground state is a $S = 0$ spin singlet. The first three excited state multiplets have respectively spin $S = 1$, $S = 2$ and $S = 3$. In the figure the energy separation between the various spin multiplets is indicated in units of the exchange parameter J_{dd}.

Ref. [6, 11], in which a STM tip (non-magnetic) is positioned above a Mn dimer deposited onto a CuN substrate. The conductance spectra are measured for different tip to sample distances. Varying the STM tip height is equivalent to changing both the current density and the electronic coupling between the tip and the sample. Non-equilibrium effects then appear as variations of the conductance profiles as a function of the STM tip height.

The parameters needed by the model can be extracted from table 5.3. It is also recalled that the ground state of the dimer is a singlet (total spin $S = 0$). The first excited state is a triplet with total spin $S = 1$ and the energy splitting between the ground state and such first excited state is exactly J_{dd}. The next excited level is the quintuplet with total spin $S = 2$ and it is separated from the first excited state by $2J_{\mathrm{dd}}$. This pattern continues throughout the spin manifold (see figure 5.14). The axial and transverse anisotropies cause the lifting of the spin multiplets degeneracy. In this case $\Gamma_{\mathrm{tip-S}}$ remains an adjustable parameter with the chosen values ranging from 0.125 meV to 200 meV.

Figure 5.15 shows the conductance spectra (normalized by G_{el}, the conductance calculated when $J_{\mathrm{sd}} = 0$) obtained by simply taking the numerical derivative of the current with respect to the bias. Three different tip to sample distance are considered, corresponding respectively to weak ($\Gamma_{\mathrm{tip-S}} = 0.125$ meV), intermediate ($\Gamma_{\mathrm{tip-S}} = 12.5$ meV) and strong ($\Gamma_{\mathrm{tip-S}} = 200$ meV) electronic coupling. The evolution of the conductance

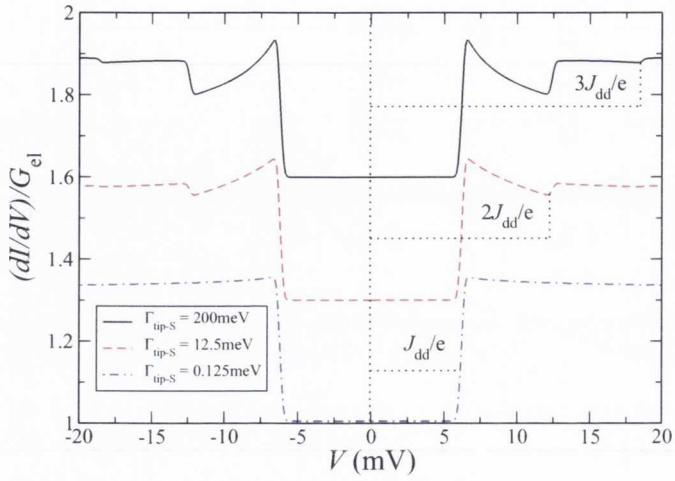

Figure 5.15: Normalized conductance spectra for the Mn dimer calculated at different tip to sample distance, i.e. for different $\Gamma_{\text{tip}-\text{S}}$ coupling strengths. We notice that the stronger is the coupling, the more the system is driven out of equilibrium. This results in the appearance of additional spin transitions, which manifest themselves as steps or drops of the conductance as a function of bias.

lineshape as a function of $\Gamma_{\text{tip}-\text{S}}$ is a direct consequence of the spin system being driven out of equilibrium. For $\Gamma_{\text{tip}-\text{S}} = 0.125$ meV the STM tip is far enough from the sample to ensure that the spin system is always in its ground state between two subsequent electron tunneling events. Therefore the only transition detected in the $G(V)$ profile is that between the $S = 0$ ground state and the first excited state with $S = 1$. This has an excitation energy equal to J_{dd} and it does manifest itself as a conductance step at a voltage $V = J_{\text{dd}}/e$, with e being the electron charge.

As the tip is brought closer to the sample ($\Gamma_{\text{tip}-\text{S}} = 12.5$ meV) the first excited triplet level ($S = 1$) starts to populate. Now an incoming electron with sufficiently large energy ($2J_{\text{dd}}$) can induce a second transition from the first to the second excited state. Note that a spin transition from the ground state to the $S = 2$ state is highly unlikely with a single electron tunneling process. This would be completely suppressed in the case of no magnetic anisotropy and it is expected to have a negligible intensity for finite, but small, values. Note that such a transition will become more probable if the spin system does

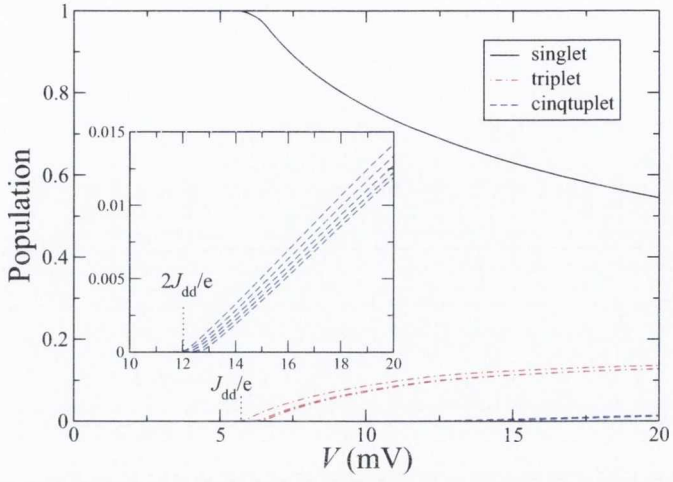

Figure 5.16: Non-equilibrium population of the Mn dimer singlet ($S = 0$), triplet ($S = 1$) and quintuplet ($S = 2$) states. The inset shows a magnified view of the population of the $S = 2$ state as it start to get populated at approximately 12 mV.

not have enough time between tunneling events to relax back to the ground state. For this case the transition appears as an increase of the conductance at the critical voltage $V = 2J_{\mathrm{dd}}/e$ with a subsequent decay. The same spectroscopic feature is further enhanced at an even larger current density ($\Gamma_{\mathrm{tip-S}} = 200$ meV), when a third conductance step appears at $3J_{\mathrm{dd}}/e$. This is associated to a transition from the $S = 2$ to the $S = 3$ spin state and it becomes possible only if the occupation of the $S = 2$ level is not zero, i.e. if the system is driven to this highly excited state. It is clear that by appropriately fixing the two adjustable parameters ε_0 and $\Gamma_{\mathrm{tip-S}}$ one can achieve almost perfect quantitative agreement with the experimental data (see Fig. 2 of Ref. [6]).

The evolution of the population of the various spin states (up to $S = 2$) as a function of bias is presented in Fig. 5.16. This is calculated in the case of strong tip to sample electronic coupling $\Gamma_{\mathrm{tip-S}} = 200$ meV. In the figure one can note the strong spin-pumping from the ground state into both the first and the second excited state. The excitation to the third excited state occurs at approximately 18 meV but it is too weak to be observed on this scale.

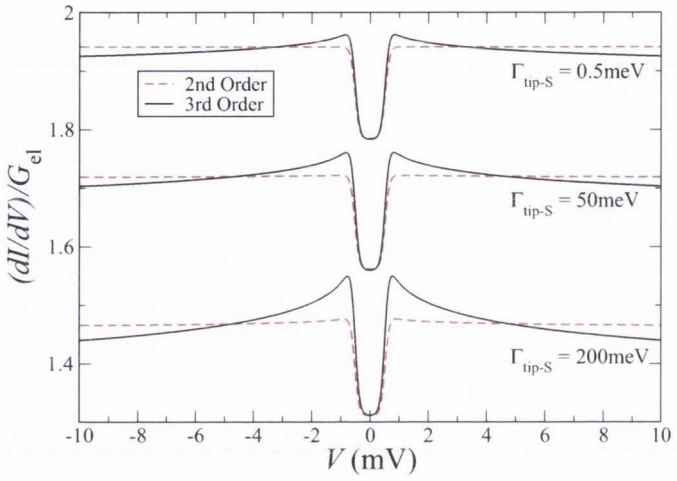

Figure 5.17: Normalized conductance spectra for a single Mn atom explored by a non spin-polarized STM tip at different tip to sample electronic couplings Γ_{tip-S}. Here a magnetic field of 3 T is applied along the z-axis. Comparison is made between calculations where the perturbation expansion is terminated either at the second or the third order.

The reason for the enhancement of the conductance step and the subsequent decay can be attributed to the bias dependence of the spin population, as described in Fig. 5.16. It is noted that there is a large dip in the ground state population at the point when the first transition occurs. Since eventually it is desirable to calculate the conductance, the derivative of the population with respect to the bias must be evaluated, which, to a good approximation, will have the appearance of a Lorentzian peak. This ultimately contributes to the conductance at the inelastic step as a peak and a subsequent dip (see Fig. 5.15). Such an effect will only appear when the system is driven out of equilibrium by increasing the tip-sample coupling Γ_{tip-S}. However, a second effect can also generate a rather similar lineshape, namely the inclusion in the perturbative expansion of third order contributions, presenting a Kondo-like logarithmic divergence, in the self-energy.

In order to make this point more clear and to qualitatively distinguish between these two possible sources of lineshape, the case of a single Mn atoms probed by a non spin-polarized tip will be investigated, whose conductance spectrum is presented in Fig. 5.17.

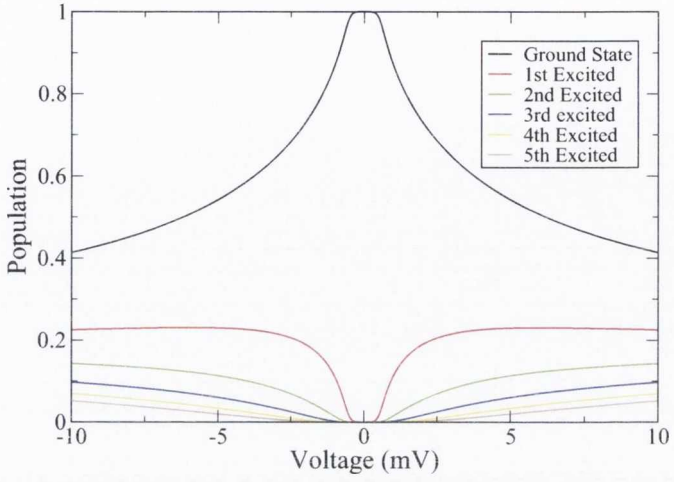

Figure 5.18: Non-equilibrium population of the various spin states of Mn on CuN as a function of bias for a non spin-polarized tip

Clearly it is observed that increasing $\Gamma_{\text{tip-S}}$ has minimal effect on the conductance line-shape. Even when $\Gamma_{\text{tip-S}} = 200$ meV and the population is driven far from equilibrium, as is seen in Fig. 5.18, no significant conductance overshoot is detected at the bias step. This effect has been explored by Novaes *et al.* in Ref. [31], where it is claimed that the conductance overshoot brought about by inelastic transitions is balanced by elastic transitions that do not alter the state of the local spin, resulting in a flat spectrum. This is in conflict with what is found in experiments, where a visible conductance peak and subsequent decay is observed at the bias step [6]. Therefore it is claimed that third order contributions to the perturbation expansion, where the logarithmic peak in this case is dependent on the parameter ρJ_{sd} and therefore exists even at equilibrium, are the main contributors to the observed non-linear conductance. This can be easily seen from the 3rd order contribution to Fig. 5.17.

5.4.3 Spin-Polarized current

A second way to induce spin-pumping, which does not necessarily require the use of intense current densities, is that of using spin-polarized electrodes. In this case the current injected into the spin-system carries a spin-imbalance, i.e. there are more electrons of a particular spin-species. This means that spin-flip transitions are likely to change the local spin always in the same direction (when the current is non-spin-polarized there is an equal probability for spin-increasing and spin-decreasing transitions). If only one of the two electrodes is spin-polarized (for instance the tip) an asymmetry in the $\mathrm{d}I/\mathrm{d}V(V)$ curve is expected, since the spin-polarization of the current, and consequently the non-equilibrium spin-population, depends on the bias polarity.

Here an attempt is made at reproducing a set of experiments from Loth *et al.* [6], in which a STM is made magnetic by placing a single Mn atom at its apex. Such a tip is then used to probe a single Mn atom deposited on a CuN substrate in the presence of a strong magnetic field (3 T and 7 T). Due to the weak anisotropy of Mn on CuN (the same parameters as those of table 5.3 are used), the strong magnetic field effectively produces a Zeeman split of the 6 levels in the $S = 5/2$ manifold. The direction of the magnetic field in these experiments is chosen so that the ground state of Mn corresponds to the spin quantum number $m = +5/2$. Since the same magnetic field is applied to the tip and to the atom to probe, their spins are collinear.

Figure 5.19 shows the calculated spectra for the system described above. In particular, a magnetic field strength of 3 T is considered and either weak ($\Gamma_{\mathrm{tip-S}} = 0.5$ meV), intermediate ($\Gamma_{\mathrm{tip-S}} = 50$ meV) or strong ($\Gamma_{\mathrm{tip-S}} = 200$ meV) tip to sample couplings. The on-site energy is fixed at $\varepsilon_0 = 1.0$ eV and the value of $J_{\mathrm{sd}} = 0.5$ eV is inferred from DFT, which results in an inelastic ratio of $\chi = 1.5$. The tip spin-polarization constant that best fits the experimental data is $\eta = -0.3$. In the weak coupling regime (when the local spin remains always close to equilibrium) the local spin resides almost entirely in its $m = +5/2$ ground state. Due to the spin-exchange selection rules and to the collinearity

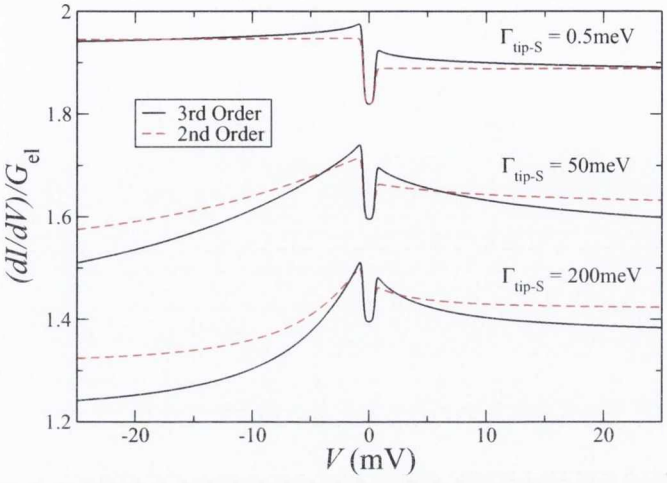

Figure 5.19: Normalized conductance spectra for a single Mn atom explored by spin-polarized STM tip at different tip to sample electronic couplings $\Gamma_{\text{tip-S}}$. Here a magnetic field of 3 T is applied along the z-axis. The asymmetry in the conductance profile is is due to the spin-polarization of the tip. Such an asymmetry is more pronounced as the system is driven further away from equilibrium. Comparison is made between second and third order calculations.

of the tip and the sample, only the minority carriers can excite the local spin out of the ground state. For a tip spin-polarization of $\eta = -0.3$, there are more minority electrons coming from the tip than those coming from the substrate. As a result, the intensity of the inelastic interaction will change depending on the direction of the current. This creates an asymmetry in the conductance spectrum with respect to the applied bias. The additional lineshape features appearing in the weak coupling case (the conductance decay following a conductance step) are due to the third order Kondo-like self-energy, which produces a logarithmic decay at the conductance steps. This result is in good agreement with experiments (see Fig. 4 of Ref. [6]).

When the spin of the Mn ion is driven further out of equilibrium, in particular in the strong coupling case, the bias asymmetry becomes more pronounced. Such spin-pumping phenomenon can be appreciated by looking at Fig. ??(a), where the populations of the six spin states of the Mn atom are shown as a function of bias for strong tip to sample coupling ($\Gamma_{\text{tip-S}} = 200$ meV). From the figure one can see that as the bias increases the

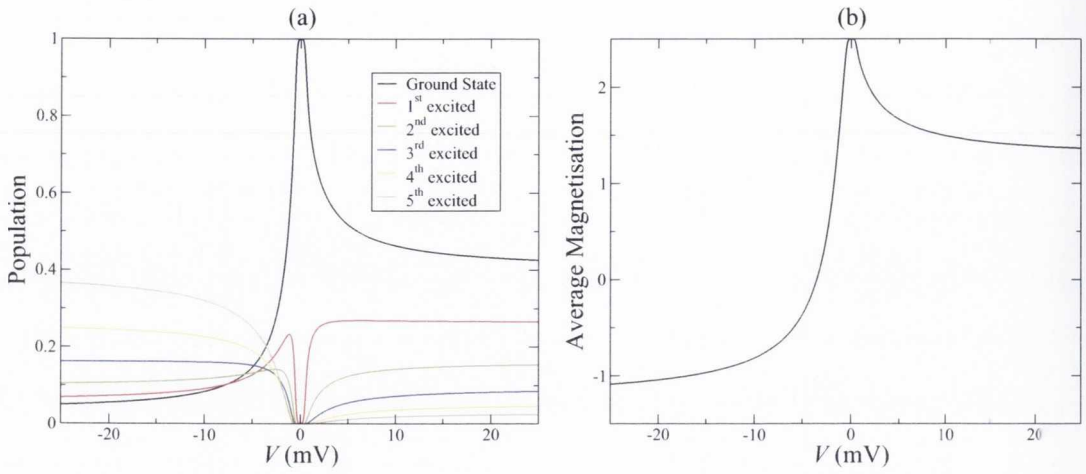

Figure 5.20: (a) Non-equilibrium population of the various spin states of Mn on CuN as a function of bias for spin-polarized tip and (b) the resulting average magnetization. These have been calculate for a magnetic field of 3 T aligned along the z-axis and for strong tip to sample electronic coupling $\Gamma_{\text{tip-S}} = 200$ meV. We notice that as the spin is driven far away from its equilibrium ground state the magnetization flips its direction.

$m = +5/2$ ground state gets depleted in favour of populating the other five excited states. In particular already at around $V = -10$ mV the population of the $m = -5/2$ level is larger than that of the ground state. In the figure the average magnetization is also plotted. This is defined as $\langle S^z \rangle = \sum_m P_m S^z_{mm}$ [see panel (b)]. Intriguingly it is found that for negative biases the spin is effectively flipped from $m = +5/2$ to $m = -1$ over a 25 meV range. The local spin is no longer collinear to the tip polarisation, and hence the inelastic signal for negative bias is weaker than that observed for positive. Therefore one observes a large dip in the conductance at negative biases when the spin is driven far from equilibrium and its polarization is effectively switched.

In Fig. 5.21 the calculated spectra for Fe is presented in the spin polarized case. Parameters in this case are chosen to conform with the experimental data of Loth *et al.* in Ref. [11]. The Fe atom is assumed to carry a quantum mechanical spin of $S = 2$ and it also exhibits a transverse easy axis anisotropy of $D = -1.53$ meV and an axial anisotropy of $E = 0.31$meV. We again assume a large value of the onsite energy, 2 eV, and we examine the spectra in the strong coupling case of $\Gamma_{\text{tip-S}} = 200$ meV with a

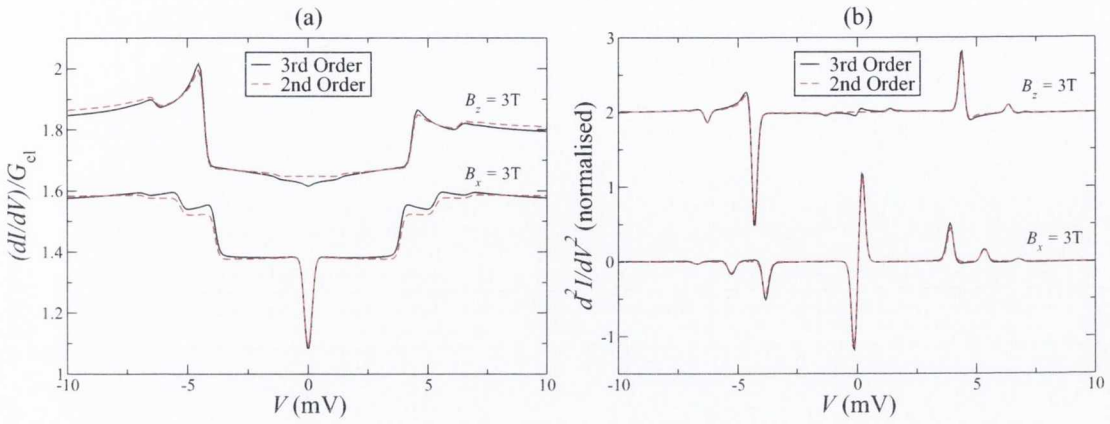

Figure 5.21: (a) 2nd and 3rd order conductance spectra for the Fe atom with spin polarization $\eta = 0.35$. The magnetic field of 3 T is applied both parallel and perpendicular to the easy axis of the Fe atom. (b) Second dervative of the current for the same spectra shown in (a).

tip polarization of $\eta = 0.35$ and magnetic field strength 3T as used in experiments. In Fig. 5.21(a) the conductance spectra for the two cases when the magnetic field is parallel or perpendicular to the easy axis of the atom (the $z-$axis in this model) is presented. As previously, it is presented for both second and third order calculations. Firstly, one notices that the spin polarized tip affects the spectra only in the case of parallel magnetic field where a clear bias asymmetry is produced. No significant asymmetry is found in the perpendicular case. This conforms with the experimental findings and is due to the fact that electron spins in the tip are no longer collinear with the localized spin of the Fe atom.

As found in the previous chapter, the inclusion of third order contributions is vital in reproducing the correct logarithmic decay at each of the conductance steps, which is particularly noticeable for the perpendicular magnetic field. More significantly, experimental spectra for the parallel case exhibit a zero bias conductance dip which is absent in the second order spectra but appears strong when third order terms are included in the perturbation expansion. This can also be seen in the calculation of the second derivative of the current in Fig. 5.21(b) where a clear zero bias anomaly is evident in the third order case.

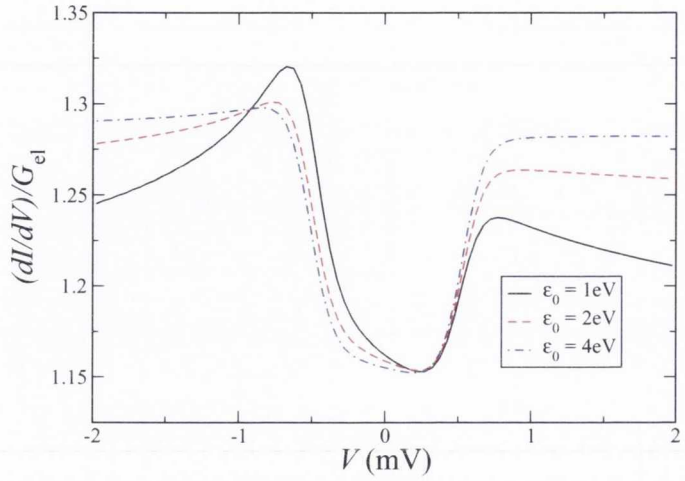

Figure 5.22: Normalized conductance spectra for a single Mn single calculated by including the real contribution to the interacting electron-spin self-energy for different on-site energies ε_0. Note that the conductance asymmetry increases with decreasing ε_0, i.e. as the onsite energy moves closer to the Fermi level.

5.4.4 Non-spin polarized asymmetry

Finally the discussion moves to the inherent asymmetry measured in the conductance profile, which is usually observed even if the tip is not spin-polarized [6, 9]. This lineshape feature is modeled by including the real part of the full interacting electron-spin self-energy derived in the previous chapter [see Eq. (4.41)]. The structure of this contribution to the self-energy shows an explicit dependence on the on-site energy, ε_0, and also a logarithmic peak of width $k_B T$ at the onset of an inelastic transition ($E - \mu_\eta = \pm\Omega_{mn}$). The asymmetry arises from the difference in polarity of the logarithmic peak for $\pm\Omega_{mn}$. The self-energy is thus an odd function of both energy and bias. This results in the conductance profile having a decrease of the step heights for $V = -\Omega_{mn}/e$ and an increase of them for $V = +\Omega_{mn}/e$.

This approach is tested by considering the case of a non-spin-polarized tip and a single Mn atom. The same anisotropy parameters are used as for the Mn dimer but, for the sake of simplicity, the spin is always in its equilibrium state and one chooses $\Gamma_{\text{tip-S}} = 0.5\text{meV}$.

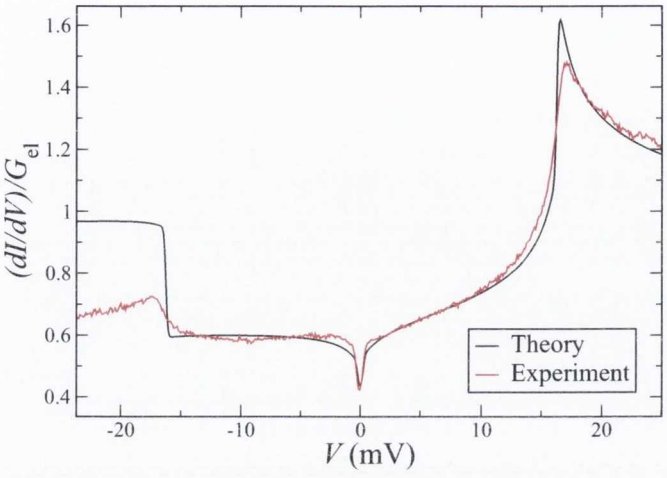

Figure 5.23: Comparison between the experimental (red) and theoretical (black) conductance spectra for a Mn trimer on CuN probed by a non-magnetic STM tip. In the calculation the real part of the interacting electron-spin self-energy has been included. This provides the conductance asymmetry with bias. The experimental data is taken from Ref. [5]

Figure 5.22 shows the resulting conductance spectra for three different choices of the on-site energy ε_0. It is clear that the closer ε_0 is to the Fermi energy (0 eV), the greater is the bias asymmetry, while as ε_0 is increased, the conductance profile becomes more symmetric. In this respect, the formalism outlined here is in agreement with the Fano lineshape argument [122] where the degree of asymmetry for electrons tunneling through a single impurity is given by a ratio of the real to the imaginary contributions to the interacting Green's function [120].

As an additional test the case of a Mn trimer is considered, whose spectrum was shown first by Hijibehedin *et al.* [5] to exhibit a large bias asymmetry when measured with a non-magnetic tip. This system is modeled by choosing an antiferromagnetic nearest neighbour exchange coupling $J_{\mathrm{dd}}^{(1)}$ =2.3 meV. Furthermore, in order to accurately describe the position of the principle conductance steps in the conductance profile, a ferromagnetic second-nearest-neighbour interaction between the local spins of magnitude $J_{\mathrm{dd}}^{(2)}$ =-1.0 meV is included [23].

The spin system is kept in equilibrium by considering a weak coupling between the STM tip and the second atom in the trimer chain ($\Gamma_{\text{tip-S}} = 0.5$ meV). The best fit to the experimental data is found with $\varepsilon_0 = -1$eV. Figure 5.23 shows the model fit to the experimental data (from Ref. [5]). Whereas previous calculations did not predict any conductance asymmetry it is clear from the figure that the inclusion of the real part of the self-energy in the description produces a significant conductance asymmetry. This is most prominent at the principle step height ($\approx \pm 16.5$meV) for each bias polarity. Although the step height for the negative bias is not as small as that found experimentally, the qualitative trends are similar. In particular one notices the logarithmic conductance increase (reduction) that occurs before (after) the onset of the step at $V = +16.5$meV, which also originates from the third order contribution to the self-energy.

Based on a perturbative approach of the $s-d$ model, here it has been shown that the entire lineshape of the spin-flip IETS can be re-conciliated with experiments by considering an expansion of the self-energy to the third order, which also includes its real part. As such it has been shown that the conductance asymmetry can be described also if the electronic orbitals forming the sample's spin are not explicitly taken into account, indicating that the origin of the asymmetry comes from a density of states effect. This has also been suggested by Delgado and Fernandez-Rossier [29].

Chapter 6

IETS as a predictive tool

Up until now the validity of the nonequilibrium Green's function approach has been tested against known experimental works and good agreement has been achieved when examining higher orders of perturbation and in spin-polarized STM tips that are subject to intense current. Given the success of the method in describing such experiments, the obvious follow-on step is to use it as a predictive tool for prospective experiments that have not yet been performed. Two topics will be treated in this chapter, namely the proposed electric field spin-crossover effect and spin impurities deposited on 2D topological insulator edges, each of which can be combined with S-P IETS to generate some intriguing results with interesting applications in the field of spintronics and quantum computng.

6.1 Electric field induced spin-crossover effect

It has been theoretically predicted that exchange coupling between local spins can be controlled electrically both for a two centre dimer [61]. In this work it has been postulated that the dependence of the Stark shift of a given magnetic system on its magnetic state results in an exchange coupling parameter that has a quadratic dependence on the applied bias voltage. This enables a spin-crossover from a low spin to high spin configuration. In this section the possibility of using a scanning tunneling microscope (STM) to detect the

dependence of the exchange coupling on an electrical potential will be investigated. A bias-dependent conductance spectrum of the most basic molecule comprising two coupled fully quantum mechanical spin 1/2 atoms will be calculated as opposed to a similar treatment for a classical localised spins[64].

6.1.1 Theoretical methods

The same single-orbital tight-binding model as in previous sections is used where a magnetic system (S) is coupled to two non-interacting electrodes denoted as tip (tip) and substrate (sub). The scattering region containing the magnetic nanostructure consists of a one-dimensional chain of N atoms. Each atom λ carries a quantum mechanical spin $\mathbf{S}_\lambda$ and it is characterized by an on-site energy ε_0. Again, it is assumed that the tip and substrate can only couple to one atom at a time in the scattering region thus broadening the electronic level ε_0 through the interaction with the electrode by $\Gamma_{\mathrm{tip/sub}}$. The total broadening due to the leads is given by $\Gamma = \Gamma_{\mathrm{tip}} + \Gamma_{\mathrm{sub}}$. The total Hamiltonian is thus described by $H_{\mathrm{S}} = H_{\mathrm{e}} + H_{\mathrm{sp}} + H_{\mathrm{e-sp}}$ where H_{e} is the tight-binding electronic part, H_{sp} is the spin part and $H_{\mathrm{e-sp}}$ describes the electron-spin interaction. The Hamiltonian writes

$$H_{\mathrm{e}} = \varepsilon_0 \sum_{\lambda\,\alpha} c^{\dagger}_{\lambda\alpha} c_{\lambda\alpha} \,, \tag{6.1}$$

$$H_{\mathrm{sp}} = 2J_{\mathrm{dd}}(V) \sum_{\lambda}^{N-1} \mathbf{S}_\lambda \cdot \mathbf{S}_{\lambda+1} + \sum_{\lambda}^{N} g\mu_{\mathrm{B}} \mathbf{B} \cdot \mathbf{S}_\lambda, \tag{6.2}$$

$$H_{\mathrm{e-sp}} = J_{\mathrm{sd}} \sum_{\lambda\,\alpha,\alpha'} (c^{\dagger}_{\lambda\alpha} [\boldsymbol{\sigma}_\lambda]_{\alpha\alpha'} c_{\lambda\alpha'}) \cdot \mathbf{S}_\lambda. \tag{6.3}$$

The electron ladder operators $c^{\dagger}_{i\alpha}/c_{i\alpha}$ create/annihilate an electron at site i with spin α $(=\uparrow,\downarrow)$ and onsite energy ε_0.

The spin-spin interaction between the localized spins $\{\mathbf{S}_\lambda\}$ is modeled by a nearest neighbour Heisenberg Hamiltonian with coupling strength J_{dd}. In this work it is assumed that spin-spin interaction takes on a quadratic bias dependence i.e. $J_{\mathrm{dd}}(V) = a + bV^2$ as

suggested by Baadji *et al.*[61] for spin crossover molecules. The parameter a is the zero bias value of $J_{\rm dd}^0$ and b defines the value of the critical voltage at which $J_{\rm dd}$ switches between ferromagnetic and anti-ferromagnetic order, $V_{\rm C} = \pm\sqrt{-a/b}$. Furthermore an interaction with an external magnetic field $\mathbf{B}$ ($\mu_{\rm B}$ is the Bohr magneton and g the gyromagnetic ratio) is assumed.

The electron-spin interaction Hamiltonian is again constructed within the s-d model [51] where the transport electrons, s, are locally exchanged coupled to quantum spins, $\{\mathbf{S}_\lambda\}$ (d indicates that the local moments originate from the atomic d shell). In this case the interaction strength is $J_{\rm sd}$ and in Eq. (6.3) $\boldsymbol{\sigma}$ is a vector of Pauli matrices.

Diagonalization of Eq. (6.2) gives the eigenenergies (ε_n) and eigenstates ($|n\rangle$) of the spin system in the interacting region. From chapter 4 it was found that the second order transition rates between two eigenstates $|n\rangle$ and $|l\rangle$ with a non-spin polarized tip is given by

$$W_{nl} = 4\frac{\rho J_{\rm sd}^2}{\Gamma}\sum_{i,\eta,\eta'}|S_{nl}^i|^2\Gamma_\eta\Gamma_{\eta'}\zeta(\mu_\eta - \mu_{\eta'} - \Omega_{nl}), \tag{6.4}$$

where the spin matrix elements $S_{nl}^i = \langle n|S^i|l\rangle$ with $i = \{x, y, z\}$ are that of a single spin in the chain that is coupled to the tip (the index λ is then dropped). Furthermore it is recalled that $\zeta(x) = x/(1 - e^{-x/(k_BT)})$ and μ_η is the chemical potential in lead $\eta = \{\text{tip}, \text{sub}\}$. It is also assumed that the onsite energy is large enough that the density of states of the sample remains constant in the small energy window of interest (meV). Therefore $\rho = \Gamma/(\varepsilon_0^2 + \Gamma^2)$. The above transition rates can be used to evaluate the bias dependence of the population of the spin system states from the steady state solution of the following

$$\frac{dP_n}{dt} = \sum_l \Big[P_n(1 - P_l)W_{ln} - P_l(1 - P_n)W_{nl}\Big] + (P_n^0 - P_n)/\beta, \tag{6.5}$$

This is iterated until self-consistency is reached for an initial guess of the population

$(P_l = P_l^0)$.

Up to second order in perturbation the normalized current through a single spin (as calculated in chapter 4) can be expressed compactly as a function of bias (see Appendix E)

$$I(V)/G_{\rm el} = V + \frac{\rho J_{\rm sd}^2}{\Gamma} \sum_{i,m,k} |S_{nl}^i|^2 P_k(V) i_-(V - \Omega_{mk}), \tag{6.6}$$

where the normalization constant is given by the elastic conductance

$$G_{\rm el} = \left(\frac{2e^2}{h}\right) \frac{\rho \Gamma_{\rm tip} \Gamma_{\rm sub}}{\Gamma}, \tag{6.7}$$

and where $i_-(V - \Omega_{mk}) = \zeta(V - \Omega_{mk}) - \zeta(-V - \Omega_{mk})$. The resulting normalized conductance, in addition to the elastic contribution, has two parts G_1 and G_2 that contribute to the total conductance $G(V)$

$$G_1(V) = \frac{\rho J_{\rm sd}^2}{\Gamma} \sum_{i,m,k} |S_{nl}^i|^2 P_k(V) \frac{d}{dV} i_-(V - \Omega_{mk}), \tag{6.8}$$

$$G_2(V) = \frac{\rho J_{\rm sd}^2}{\Gamma} \sum_{i,m,k} |S_{nl}^i|^2 i_-(V - \Omega_{mk}) \frac{d}{dV} P_k(V), \tag{6.9}$$

$$G(V) = 1 + G_1(V) + G_2(V). \tag{6.10}$$

In the equilibrium case when P_k is constant with bias for all k then G_1 becomes the only contributor and represents the conductance step whenever the bias coincides with the inelastic energy transition Ω_{mk}. The conductance step height over the elastic conductance is then governed by the ratio $\rho J_{\rm sd}^2/\Gamma$. However in the non-equilibrium case when $P_k(V)$ varies with bias both G_1 and G_2 contribute and result in more complicated non-linear conductances.

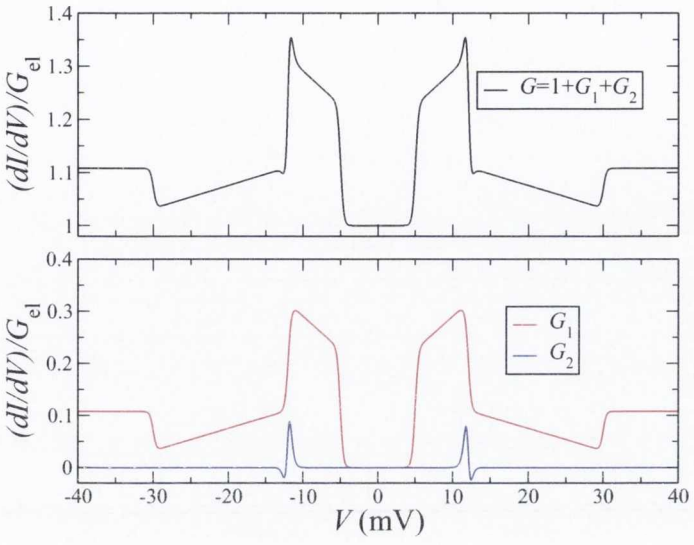

Figure 6.1: (Color online) Upper Panel: Total contribution to the normalized conductance spectra for the spin 1/2 dimer. Lower Panel: Normalized conductance contributions to the total. The large dip in conductance at 12 mV represents the spin crossover critical voltage.

6.1.2 Results

As a test of the fully quantum mechanical treatment of electric field induced spin crossover in magnetic molecules the simplest case of a pair of spin $S = 1/2$ atoms coupled through the bias dependent spin exchange parameter $J_{\rm dd}(V) = a + bV^2$ is examined. At zero biasit is assumed that the local spins are coupled anti-ferromagnetically by the parameter $a = +6$meV. Diagonalization of Eq. (6.2) reveals that at zero bias the resulting ground state of the spin system is a singlet with total spin $S_{\rm tot} = 0$. The excited state is a triplet with total spin $S_{\rm tot} = 1$ and is split from the singlet state by the zero bias exchange energy $a = +6$meV. A value for $b = -0.04\text{meV}/(\text{mV})^2$ is chosen in line with DFT predictions [61]. A spin-crossover between total spin states $S_{\rm tot} = 0$ and $S_{\rm tot} = 1$ is encountered when the voltage reaches the critical point $V_{\rm C} = \pm\sqrt{-a/b}$ where $J_{\rm dd}(V)$ switches from anti-ferromagnetic (positive) to ferromagnetic (negative).

To construct a full conductance profile of the spin crossover event from Eqs. (6.8)-(6.10) one must chose values for the remaining parameters which are retrieved from both experimental and theoretical descriptions of similar STM setups. Firstly it is assumed that

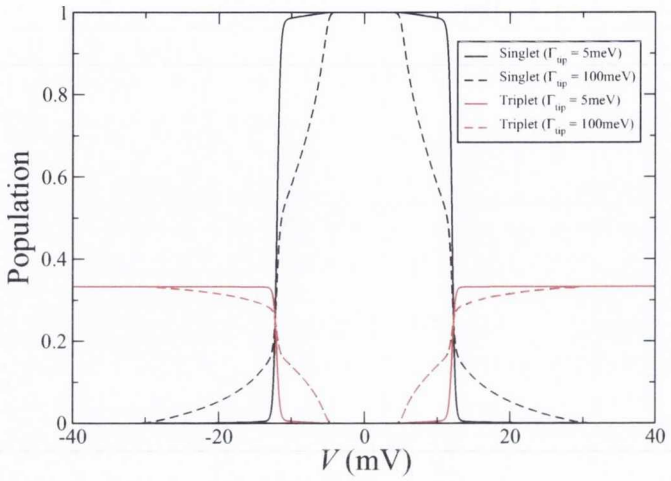

Figure 6.2: (Color online) Population of the singlet (black) and triplet (red) states for weak (solid line) and strong (dashed line) coupling to the tip.

the s-d exchange is $J_{\mathrm{sd}} = 500\mathrm{meV}$ as found from DFT calculations [116]. It is assumed that the electronic energies of the dimer atoms are of the order of 1eV, far enough from the fermi energy to ensure a constant density of states ρ in the low energy window of interest. The atoms are coupled to the underlying substrate strongly enough to produce a broadening of the onsite energies of $\Gamma_{\mathrm{sub}} = 250\mathrm{meV}$. Furthermore it is assumed that the tip is non spin-polarized and movable such that conductance spectra can be investigated for a range of Γ_{tip}. The effect of magnetic fields on the spectra will also be investigated and a Lande g-factor of 2 is assumed. All spectra are obtained at a temperature of 1.5K.

The top panel of Fig. 6.1 shows the total conductance (G) for the above parameters with the tip positioned above one of the atoms in the dimer with a weak tip-atom coupling of $\Gamma_{\mathrm{tip}} = 5\mathrm{meV}$. The bottom panel shows how the spectrum is broken up into its various components, G_1 and G_2 from Eqs. (6.8) and (6.9). It is clear that the main features of the total conductance (G) are reproduced by G_1 where the derivative of the population is not considered. The first conductance step represents the spin-excitation from singlet to triplet. The spin crossover then occurs at $V_{\mathrm{C}} = \pm\sqrt{-a/b} = \pm 12.25\mathrm{meV}$ and is represented

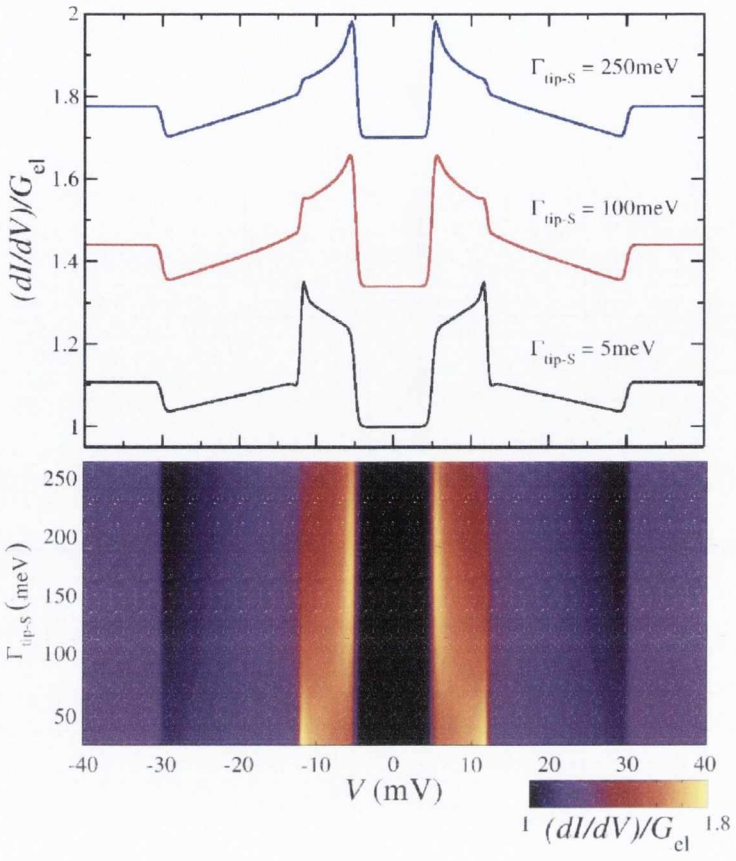

Figure 6.3: Upper panel: Normalized conductance spectra of the spin 1/2 dimer for varying values of Γ_{tip}. Lower panel: Corresponding colour plot. The conductance drop at V_C weakens for strong tip-atom couplings.

by a large dip in conductance. This is well explained by the bias dependent population plot in Fig. 6.2 (solid black and red lines). At the crossover point, a change in the ground state occurs and the population of the singlet state rapidly decreases from full (1) to empty (0) while the triplet states are equally filled from 0 to 1/3. As the voltage increases, the split between the new ground state triplet and new excited state singlet becomes larger. A voltage is then reached (30mV) where a spin excitation between the new ground and excited state occurs. The contribution of G_2 is seen as an additional non-linear effect at the spin-crossover point brought about by the derivative of the population of the states.

The upper and lower panels of Fig. 6.3 show that by increasing the coupling of the tip to the atom, the conductance spectra can be greatly modified. It can be clearly seen from

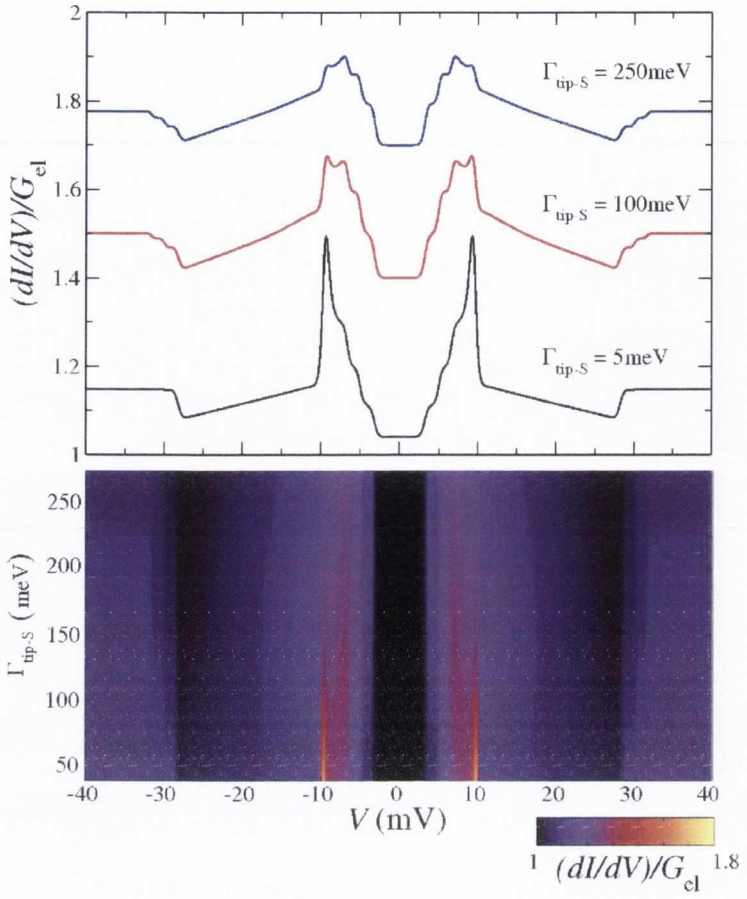

Figure 6.4: Upper Panel: Normalized conductance spectra of the spin 1/2 dimer for varying values of Γ_{tip} with applied magnetic field of 20T. Lower Panel: Corresponding colour plot. One notices the Zeeman splitting of the triplet levels.

both plots that the magnitude of the conductance dip at the crossover point becomes less severe. This is due to a change in the population of the states when the coupling is increased (see the dashed black and red lines of Fig. 6.2) where pumping out of the ground state into the excited state occurs before the onset of the spin-crossover. This also results in the enhancement of the first conductance step and resultant decay as was discussed in chapter 5.

Finally the effect of applying a magnetic field to the spin system is investigated. For the purpose of clear illustration a large value of 20T is applied in the z direction. It is pointed out to the reader however that this value is in general experimentally unattainable. Figure 6.4 shows the variation of the spectra for different values of Γ_{tip}. One notices in

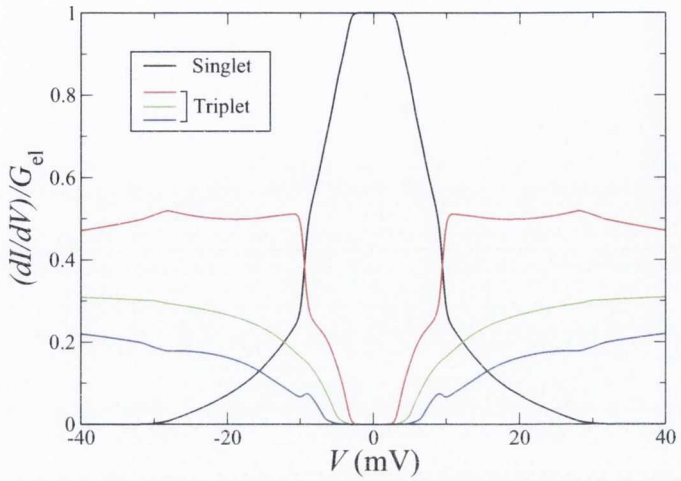

Figure 6.5: (Color online) Population of the singlet and triplet states for strong coupling of the tip to the atom $Gamma_{\mathrm{tip}}$. The large splitting of the triplet state populations is notable.

both upper and lower panels that the onset of the magnetic field splits the triplet into its Zeeman components which is manifested as three equal sized conductance steps around the zero-bias spin-exchange parameter. As in the zero-field case the magnitude of the conductance drop at the spin-crossover point decreases with increasing Γ_{tip}. The second conductance step (30mV) from ground state triplet to excited state singlet takes a slightly different form for increasing tip-atom coupling. The resolution of the Zeeman-split triplet states occurs at high couplings. This is explained by Fig. 6.5 where the populations of the 4 states are now well separated at high tip-atom coupling. Due to the varied populations of the triplet states, the probability of a spin transition from the triplet state to the excited singlet state becomes highly dependent on Γ_{tip}.

6.2 Spin-pumping and inelastic electron tunneling spe troscopy in topological insulators

In this section it will be shown how a magnetic impurity deposited at the edge of a Z_2 TI and presenting a uni-axial magnetic anisotropy, which makes it non-Kondo-active [74], can be manipulated by a quantum spin Hall (QSH) current. The topological nature of the QSH state has profound consequences on the SF-IETS conductance spectrum. At low current intensity there is a complete suppression of the conductance steps appearing at the critical biases characteristic of the activation of an inelastic spin-scattering channel [3]. In contrast, for currents large enough to produce spin-pumping the spin of the magnetic impurity is driven away from the anisotropy axis. This breaks the topological protection of the helical edge states and the conductance steps reappear. Intriguingly, in this situation there is a strong dependence of the SF-IETS conductance spectrum on the bias polarity. Again, the calculations are conducted by using the non-equilibrium Green's function method for transport combined with a perturbative approach to spin-scattering from magnetic impurities as introduced in the previous chapters.

6.2.1 Kane-Mele Hamiltonian

The initial structure that will be dealt without considering the effect of a spin impurity is a Z_2 2-D topological insulator (TI) ribbon on a honeycomb lattice with zig-zag edge geometry as in Fig. 6.6. The left and right leads are square lattice structures coupled to the T.I. The Kane-Mele model to describe the single particle electrons in the device region with the following Hamiltonian H_{KM}

$$H_{KM} = \varepsilon_0 \sum_{i\alpha} \xi_i c^\dagger_{i\alpha} c_{i\alpha} + t_1 \sum_{\langle ij\rangle,\alpha} c^\dagger_{i\alpha} c_{j\alpha} + it_2 \sum_{\langle\langle ij\rangle\rangle,\alpha\beta} \nu_{ij} c^\dagger_{i\alpha} [\sigma^z]_{\alpha\beta} c_{j\alpha}. \tag{6.11}$$

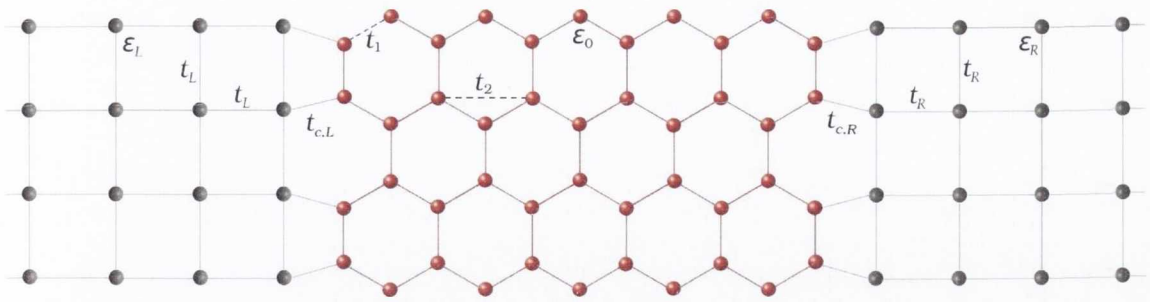

Figure 6.6: Schematic representation of the device considered in this work, comprising a TI with honeycomb lattice structure coupled between two semi-infinite square leads

The first term describes a staggered sub-lattice potential with on-site energy ε_0 and ξ_i being $\xi_i = +1$ for the A sub-lattice and $\xi_i = -1$ for the B one. Here $c^{\dagger}_{i\alpha}$ ($c_{i\alpha}$) creates (annihilates) an electron at site i with spin α. The second term is the nearest neighbour hopping with strength t_1 (t_1 sets the energy scale of the problem). Finally the third term, which drives the topological phase, is a second nearest neighbour hopping with strength t_2 ($i = \sqrt{-1}$). This describes the coupling of the electrons orbital motion to their spins via the z-component of the Pauli matrices (σ^z). The parameter ν_{ij} is $+1$ for counter-clockwise hopping and -1 for clockwise. The dimension of the device is simply $2N = 2(n_x \times n_y)$ where n_x is the number of atoms per zig-zag row n_y and the factor of 2 takes into account the electronic spin. The leads are assumed to be of a square lattice structure, the properties of which will be dealt with in the following section.

6.2.2 Two-dimensional lead self energy

The procedure for calculating transport properties of two dimensional systems is significantly different to that used for one dimensional systems [123]. In particular, scalar quantities of one dimensional arrays such as nearest neighbour couplings must now be recast in terms of matrices that describe the two dimensional structure of the TI ribbon and connecting leads. In the following the example of a square lattice is used to show how to calculate the self energy of a given lead, as introduced in Fig. 6.6. For simplicity $n_s = 4$ is used where n_s is the number of surface atoms in the lead. The central device

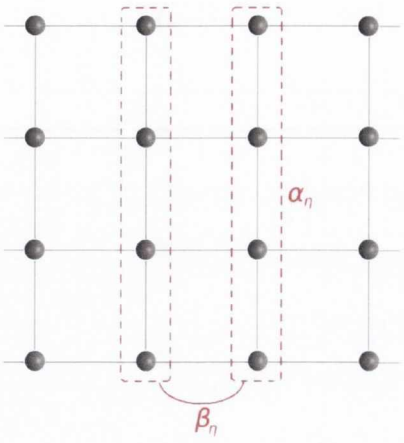

Figure 6.7: Schematic illustrating the construction of the various coupling matrices in the 2D model. Each layer labeled by α_η is coupled to its nearest neighbour by β_η

region can take any structural form and it is assumed that it contains a total of N atoms.

The two matrices $[\alpha_\eta]$ and $[\beta_\eta]$ are introduced where $\eta = L, R$. The schematic in Fig. 6.7 shows how these matrices are constructed within given layers containing n_s atoms. $[\alpha_\eta]$ contains the onsite energies ε_η and the intra-layer coupling t_η whereas $[\beta_\eta]$ contains the inter-layer coupling, also with stength t_η. It is seen how the lead can be constructed layer by layer with each α_η coupled to the adjacent one by β_η. These matrices are then $n_s \times n_s$ in dimension and can be defined as

$$[\alpha_\eta]_{n_s \times n_s} = \begin{pmatrix} \varepsilon_\eta & t_\eta & 0 & 0 \\ t_\eta & \varepsilon_\eta & t_\eta & 0 \\ 0 & t_\eta & \varepsilon_\eta & t_\eta \\ 0 & 0 & t_\eta & \varepsilon_\eta \end{pmatrix} ; \; [\beta_\eta]_{n_s \times n_s} = \begin{pmatrix} t_\eta & 0 & 0 & 0 \\ 0 & t_\eta & 0 & 0 \\ 0 & 0 & t_\eta & 0 \\ 0 & 0 & 0 & t_\eta \end{pmatrix}. \tag{6.12}$$

Following from this the surface Green's function of the lead η can be defined by using Dyson's equation and it is found that

$$[g_{s,\eta}]_{n_s \times n_s} = [(E + i0^+)\mathbb{1} - \alpha_\eta - \beta_\eta^\dagger g_{s,\eta} \beta_\eta]^{-1}, \tag{6.13}$$

where 0^+ is a positive infinitesimal and the identity matrix $\mathbb{1}$ is also $n_s \times n_s$ in dimension.

Since the surface Green's function is self-dependent, a self consistent approach is needed to evaluate its value at each energy E. As such the appropriate initial guess for the surface Green's function is

$$[g^0_{s,\eta}]_{n_s \times n_s} = [(E + i0^+)\mathbb{1} - \alpha_\eta]^{-1}. \tag{6.14}$$

The result is then iterated until self-consistency is reached.

The coupling between the lead and the central device region (of dimension N) is described by the matrix $[\tau_\eta]$. This has dimension $N \times n_s$ and using the nearest-neighbour approximation will describe coupling of strength $t_{c,\eta}$ between the outermost atoms in both the leads and the device region. The matrix then takes the following form

$$[\tau_\eta]_{N \times n_s} = \begin{pmatrix} t_{c,\eta} & 0 & 0 & 0 \\ 0 & 0 & 0 & 0 \\ \vdots & \vdots & \vdots & \vdots \\ 0 & t_{c,\eta} & 0 & 0 \\ 0 & 0 & 0 & 0 \\ \vdots & \vdots & \vdots & \vdots \\ 0 & 0 & t_{c,\eta} & 0 \\ 0 & 0 & 0 & 0 \\ \vdots & \vdots & \vdots & \vdots \\ 0 & 0 & 0 & t_{c,\eta} \end{pmatrix}. \tag{6.15}$$

All the quantities that are needed to construct the self energy of the lead are now in place. This has the dimensions of the device region, $N \times N$, and through Dyson's equation can be defined as

$$[\Sigma_\eta]_{N \times N} = [\tau_\eta]_{N \times n_s} [g_{s,\eta}]_{n_s \times n_s} [\tau^\dagger_\eta]_{n_s \times N}. \tag{6.16}$$

The self energies are complex quantities whose real part renormalizes the eigenstates in the device region. The imaginary part is also important and contributes to the broadening function which can be defined by

$$[\Gamma_\eta] = i[\Sigma_\eta - \Sigma_\eta^\dagger]. \tag{6.17}$$

This results in a finite lifetime for each eigenstate in the device region.

For a given Hamiltonian H that describes the central device region, the retarded and advanced Green's functions of the unperturbed system without spin interaction can be defined as

$$[G_0^r]_{N\times N} = [(E + i0^+)\mathbb{1} - H - \Sigma_L - \Sigma_R]^{-1}, \tag{6.18}$$

$$[G_0^a]_{N\times N} = [(E - i0^+)\mathbb{1} - H - \Sigma_L^\dagger - \Sigma_R^\dagger]^{-1} \tag{6.19}$$

where the resulting transmission function takes the form

$$T(E) = \mathrm{Tr}[\Gamma_L G_0^r \Gamma_R G_0^a]. \tag{6.20}$$

If a bias V is applied between left and right lead the corresponding current and conductance profiles for the given device region can be calculated. To do this the definition is needed for the Fermi functions in each of the leads as a function of the energy E $f_\eta(E) = 1/\{1 + \exp[(E - \mu_\eta)/k_B T]\}$. This describes the electonic filling of each of the leads with the chemical potentials $\mu_L = \varepsilon_F + V/2$ and $\mu_R = \varepsilon_F - V/2$. Following on from the original formalism for one dimensional transport introduced in chapter 3, the greater and lesser Green's functions in the device region and self energies in the leads can be

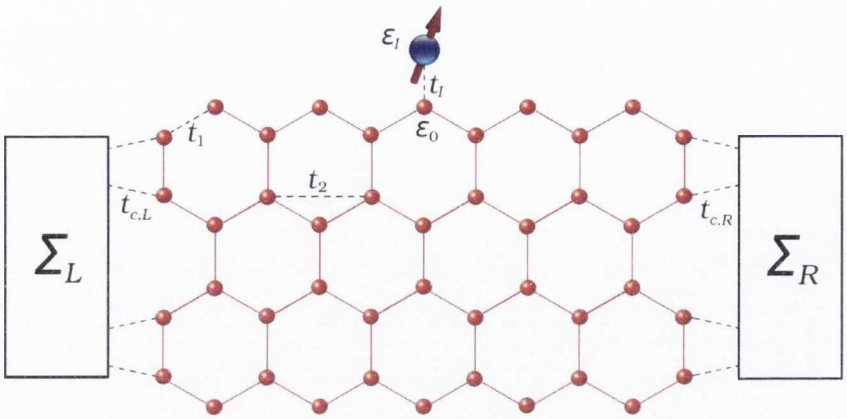

Figure 6.8: Schematic representation of the device with spin impurity (I) coupled to the TI edge. The square leads have been replaced by the self energies Σ_L and Σ_R

written as

$$[\Sigma_\eta^<] = f_\eta[\Gamma_\eta] \; ; \; [\Sigma_\eta^>] = (1 - f_\eta)[\Gamma_\eta], \tag{6.21}$$

$$[G_0^<] = [G_0^r(\Sigma_L^< + \Sigma_R^<)G_0^a]. \tag{6.22}$$

6.2.3 Spin impurity on topological insulator edge

In this subsection a spin impurity is introduced that can be attached to a given site λ in the honeycomb lattice discussed previously. The full contribution to the electronic part of the Hamiltonian H_{el} including the Kane-Mele Hamiltonian from Eq. (6.11) is

$$H_{\text{el}} = H_{KM} + \varepsilon_I \sum_\alpha c_{I\alpha}^\dagger c_{I\alpha} + t_I \sum_{\langle I\lambda\rangle,\alpha} c_{I\alpha}^\dagger c_{\lambda\alpha}, \tag{6.23}$$

where I labels the spin impurity with onsite energy ε_I and the coupling to nearest neighbour site λ is given by t_I. The spin is labeled by α and the total dimension is now $2N = 2(n_x n_y + 1)$. A schematic of the device with the spin impurity is seen in Fig. 6.8. In addition to the electronic part of the total Hamiltonian the spin degree of freedom of the localized impurity must be incorporated in which it is assumed that the given spin experiences an axial anisotropy due to coupling to the underlying staggered lattice structure.

Therefore

$$H_{\rm sp} = DS_z^2, \tag{6.24}$$

where D is the zero field splitting parameter describing the uni-axial anisotropy which in this case is assumed to be in the plane along the z-axis. Diagonalization of the Hamiltonian yields the eigenvalues ε_n with eigenvectors $|n\rangle$, which are used to obtain the populations P_n given by the Boltzmann distribution

$$P_n = \frac{\exp(-\varepsilon_n/k_BT)}{\sum_m \exp(-\varepsilon_m/k_BT)}. \tag{6.25}$$

One can also define the spin matrix elements which represent the transition probability from one state to another. These are given by $\langle m|S^i|n\rangle = S^i_{mn}$ where $i = +, -, z$ and $S^{\pm} = (S^x \pm iS^y)$.

The coupling between the localized spin and the current carrying electrons in the localized atom will again be considered here where it will be assumed that it can be described by the s-d interaction.

$$H_{\rm el-sp} = J_{\rm sd} \sum_{\alpha\beta} c^{\dagger}_{I\alpha}[\boldsymbol{\sigma}]_{\alpha\beta} c_{I\beta}.\mathbf{S}, \tag{6.26}$$

where the strength of the interaction is $J_{\rm sd}$ and $[\boldsymbol{\sigma}]$ is a vector of Pauli matrices. The coupling between electron spins and localized spins will again be treated perturbatively as done in previous chapters. The result is an interacting spin dependent self energy which when truncated at second order is proportional to the non-interaction Green's function $G_0(E \pm \Omega_{mn})$ where $\Omega_{mn} = \varepsilon_m - \varepsilon_m$ and describes the spin flip mechanism of an incoming electron interacting with a localized spin $\mathbf{S}$. It can be written in the following form for

the lesser and greater interacting self-energy (recall Eq. (4.34) and (4.35))

$$[\Sigma^{\lessgtr}_{\text{int}}(E)]^{(2)}_{\uparrow\uparrow} = -J^2_{\text{sd}} \sum_{m,n} [G^{\lessgtr}_0(E \pm \Omega_{mn})]_{\uparrow\uparrow} \Big(\delta_{nm} \chi P_n S^z_{mn} + P_n(1 - P_m)|S^z_{mn}|^2 \Big)$$
$$- J^2_{\text{sd}} \sum_{m,n} [G^{\lessgtr}_0(E \pm \Omega_{mn})]_{\downarrow\downarrow} P_n(1 - P_m)|S^{\pm}_{mn}|^2, \tag{6.27}$$

$$[\Sigma^{\lessgtr}_{\text{int}}(E)]^{(2)}_{\downarrow\downarrow} = -J^2_{\text{sd}} \sum_{m,n} [G^{\lessgtr}_0(E \pm \Omega_{mn})]_{\downarrow\downarrow} \Big(-\delta_{nm} \chi P_n S^z_{mn} + P_n(1 - P_m)|S^z_{mn}|^2 \Big)$$
$$- J^2_{\text{sd}} \sum_{m,n} [G^{\lessgtr}_0(E \pm \Omega_{mn})]_{\uparrow\uparrow} P_n(1 - P_m)|S^{\mp}_{mn}|^2, \tag{6.28}$$

where $\chi = \varepsilon_I / J_{\text{sd}}$ is the inelastic ratio. It is also noted from previous results that by driving the current in the system (achieved previously by bringing the STM tip closer to the given adatom) a bias dependent population of the local spin states emerges and the spin system is out of equilibrium. This reflects the effect that the current carrying electrons has on the localized spin. If more and more electrons come in contact with the spin then it will not be allowed relax back to its ground state and the higher excited states will begin to be populated. This bias dependent population is treated within the local spin self energy (refer to chapter 4) and the resulting master equation governing each state $|n\rangle$ is given by

$$\frac{dP_n}{dt} = \sum_l \Big[P_n(1 - P_l) W_{ln} - P_l(1 - P_n) W_{nl} \Big] + (P^0_n - P_n)/\beta, \tag{6.29}$$

where the transition rates between initial state $|l\rangle$ and final state $|n\rangle$ is given by the expression:

$$W_{nl} = -\frac{J^2_{\text{sd}}}{\pi} \sum_{i,\alpha,\beta} \Big(\chi S^i_{nm} \delta_{\alpha\beta} \sigma^i_{\alpha\alpha} + |S^i_{nl}|^2 |\sigma^i_{\alpha\beta}|^2 \Big) \int_{-\infty}^{+\infty} d\omega [G^{<}_0(\omega)]_{\beta\beta} [G^{>}_0(\omega - \Omega_{nl})]_{\alpha\alpha}. \tag{6.30}$$

It will be shown in subsequent sections that this quantity is highly dependent on the strength of the parameters $t_{c,\eta}$. The greater the coupling, the more the system is driven

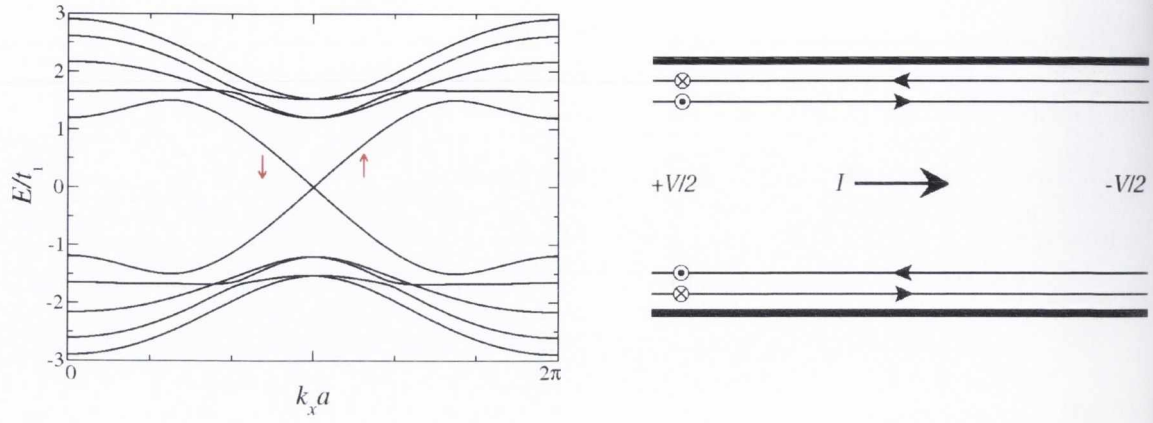

Figure 6.9: (a) Band-structure of the TI ribbon constrained to 10 atoms along the y axis. The edge states are spin filtered so that electrons with opposite spins propagate in opposite directions. (b) Schematic of the situation when a potential difference is applied between the two leads it is seen that spin down electrons travel anti-clockwise and spin up electrons travel clockwise.

out of equilibrium and higher excited states populated.

With all this at hand the current and conductance at a given lead η can now be constructed. This takes the following form

$$I_\eta(V) = \int \mathrm{Tr}\Big[\Sigma_\eta^<(E)G^>(E) - \Sigma_\eta^>(E)G^<(E)\Big]dE, \tag{6.31}$$

and the conductance is simply the derivative of the above quantity with respect to the bias. The Green's function in this case is the full interacting one and is defined as follows:

$$G^\lessgtr(E) = G^r(E)\Big[\Sigma_L^\lessgtr(E) + \Sigma_R^\lessgtr(E) + \Sigma_{\mathrm{int}}^\lessgtr(E)\Big]G^a(E). \tag{6.32}$$

6.2.4 Results: Spin-flip mechanism on topological insulators

The discussion begins by first looking at the electronic structure and transport properties of the ribbon in absence of the magnetic impurity. Figure 6.9(a) shows the band-structure for such a zig-zag structure that extends to infinity along the x-axis and is constrained to a length of $n_y = 10$ along the y axis without a spin impurity. The ratio $t_1/t_2 = 1/3$

(a choice which preserves the topology [125]) and the onsite energy ε_0 is chosen to be zero (the choice of ε_0 is arbitrary and will have little effect on dynamics around the Fermi energy). At the Fermi energy $\varepsilon_F = 0$ it can be seen that two bands traverse the bulk band-gap and each are localized at the edges of the strip with degenerate copies for each edge. These 'edge states' are spin filtered, meaning that electrons with opposite spins propagate in opposite directions with spin down electrons traveling anti-clockwise and spin up electrons traveling clockwise. Therefore if a potential difference is set up between the left and the right ends of a graphene strip the situation outlined in figure 6.9(b) is encountered when electric current flows from left to right.

The transport properties of the TI ribbon are investigated by calculating the spin-resolved transmission coefficients along a given edge [124] for a *finite* slab of the zig-zag structure. This quantity is defined as

$$T^s_{\alpha\alpha'}(\varepsilon_{\rm F}) = {\rm Tr}_{n_x}[\Gamma_{\rm L} G^r \Gamma_{\rm R} G^a]^s_{\alpha\alpha'} \,, \tag{6.33}$$

where α is the spin index ($\alpha = \uparrow, \downarrow$), s labels the edges (s = top, bottom) and G^a is the advanced Green's function. The trace is over the number of atoms, n_x, along the given edge and the transmission coefficient is evaluated at the Fermi energy, $\varepsilon_{\rm F}$. As a matter of notation a (n_x, n_y) ribbon contains n_x atoms in the direction of transport and n_y along the transverse one. When the Fermi level is fixed at the half-filling point the ribbon is insulating in the bulk, but presents edge topological protected states (here $t_{\eta{\rm R}} = t_\eta = t_1 = 1$, and $t_2 = t_1/3$, which ensures that the KM Hamiltonian describes a QSH state). In this situation we find for a (11, 6) ribbon, $T^{\rm top}_{\uparrow\uparrow} = 0.9$, $T^{\rm top}_{\downarrow\downarrow} = 0.1$, $T^{\rm bottom}_{\uparrow\uparrow} = 0.1$ and $T^{\rm bottom}_{\downarrow\downarrow} = 0.9$. Such values demonstrate that the current along the QSH edges is spin-polarized, although not completely because of the finite size of the ribbon. Calculations for a (7, 4) ribbon give us $T^{\rm top}_{\uparrow\uparrow} = 0.85$, $T^{\rm top}_{\downarrow\downarrow} = 0.15$, $T^{\rm bottom}_{\uparrow\uparrow} = 0.15$ and $T^{\rm bottom}_{\downarrow\downarrow} = 0.85$.

The magnetic interaction between a $S = 1$ local spin and a (11, 6) ribbon is now

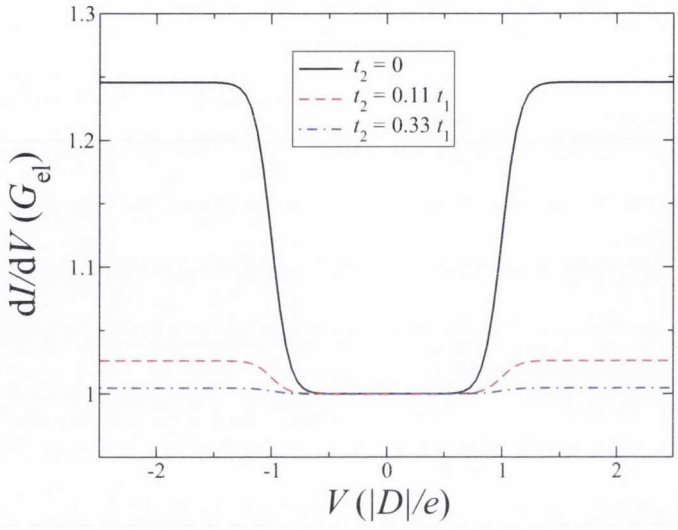

Figure 6.10: SP-IETS conductance spectrum for a TI (11, 6) ribbon with a $S = 1$ magnetic impurity attached at the upper edge. Note that the conductance step at the voltage characteristic of the inelastic excitation gets suppressed as the t_2 parameter is increased, i.e. as the ribbon is brought well inside the topological region of the phase diagram.

investigated. In general the impurity is placed at the centre of the edge and a coupling parameter, t_I, and an onsite energy, ε_I, is chosen to ensure that the density of states localized at the impurity site, $\rho_I(E)$, is approximately constant for energies, E, around the Fermi level (this ensures the convergence of the perturbation scheme). The exchange coupling, $J_{\rm sd}$, is chosen so that the perturbation parameter, $\rho_I J_{\rm sd}$, is approximately 0.1. These conditions are satisfied for: $\varepsilon_I = J_{\rm sd} = t_1/2$ and $t_I = t_1/4$. The spin degeneracy is lifted by an axial anisotropy $D = -10^{-3}\, t_1$, which corresponds to $D = -2.0$ meV, if the nearest neighbour hopping in the ribbon is fixed at a reasonable value of $t_1 = 2$ eV ($k_{\rm B}T = 0.05$). The uni-axial anisotropy gives a degenerate ground state with the two spin states $|-1\rangle$ and $|+1\rangle$ separated from the first excited state $|0\rangle$ by $|D|$. As a result no Kondo-like behaviour is expected since no allowed transition between the degenerate ground state may occur. The second order perturbation expansion is then well justified. The values $t_\eta = 4t_{\eta\rm R} = t_1$ ensure that the spin system remains in equilibrium, i.e. in its ground state, throughout the spin-scattering process.

Figure 6.10 shows the calculated conductance spectra, $G(V)$, normalized to the $V = 0$

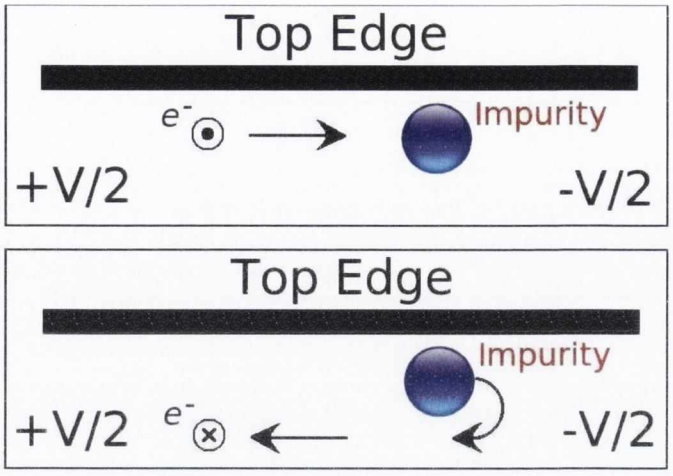

Figure 6.11: Cartoon that describes the spin-flip scattering event. A right-going electron with up spin direction (top panel) is inelastically back-scattered by the magnetic impurity. In the process both the electron and the impurity spins are reversed (bottom panel). Note that, given the topological nature of the ribbon, spin-flip forbids electron transmission as the edge presenting a right-going spin-up state does not possess a right-going spin-down one.

conductance, $G_{\rm el}$, for three values of the parameter governing the QSH state, t_2. For $t_2 = 0$ there are no topologically protected edges and the characteristic inelastic conductance step at a voltage $V = D/e$ is observed, when the transition from the ground state to $|0\rangle$ becomes possible (e is the electron charge). However, as t_2 is increased and the topological phase is entered, a suppression of the inelastic contribution to the conductance is observed, with an almost full suppression at the maximum value of $t_2 = t_1/3$. The cartoon in Fig. 6.11 helps to understand the mechanism for such a suppression. At a positive bias, the right-going current is up spin-polarized. This means that the $|-1\rangle \rightarrow |0\rangle$ transition scatters out spin-down electrons. These cannot propagate towards the right electrode since there is no right-moving spin-down state in the upper edge and, as a consequence, they are completely reflected. Hence, as spin-flip events can only lead to backscattered electrons, the inelastic channel does not contribute to the current. Note that the residual conductance increase in Fig. 6.10 for $t_2 = t_1/3$ is simply due to the finite size of the ribbon.

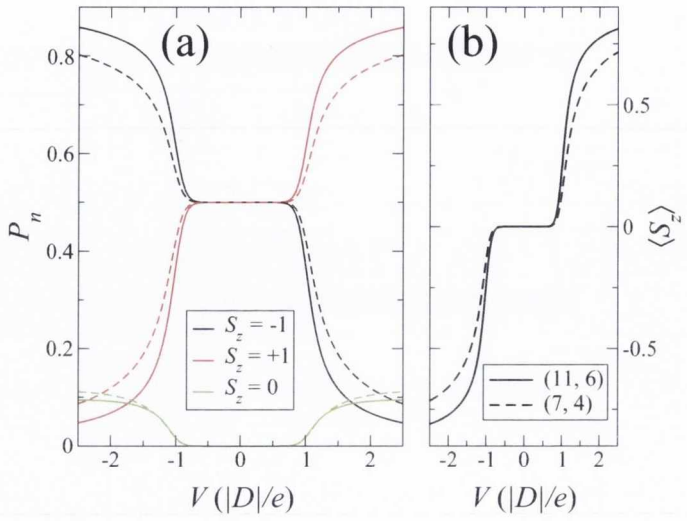

Figure 6.12: (Color online) (a) Non-equilibrium population as a function of bias of the $S = 1$ impurity spin states for a (7, 4) (broken lines) and a (11, 6) ribbon (solid lines). In panel (b) we show the average magnetization of the impurity for the same ribbons.

6.2.5 Results: Current driven local spin dynamics

The possibility of manipulating the impurity spin direction is now investigated. This is achieved by increasing the overall conductance, i.e. by increasing the average current density. When one works with an STM setup bringing the tip closer to the impurity [6] does the job, while here the control parameter is the electronic coupling between the leads and the ribbon, $t_{c\eta}$. As such all the calculations that follow have been performed with $t_{c\eta} = t_1$.

The calculated populations of the various spin states are plotted as a function of bias in Fig. 6.12(a) for both a (11, 6) and a (7, 4) ribbon. A $S = 1$ spin in a uni-axial anisotropy field and in thermal equilibrium with an electron bath presents an equal probability to occupy the $|+1\rangle$ and the $|-1\rangle$ states, i.e. for $V = 0$ one has $P_{+1} = P_{-1} = 1/2$. As soon as the bias is increased at and above $|D|/e$, excitations to the $|0\rangle$ state become possible due to spin-flip back-scattering. In this case however the current is intense, so that in between two scattering events the impurity spin does not have the time to relax back to the degenerate ground state. This means that now a spin-up electron (the majority species in the upper

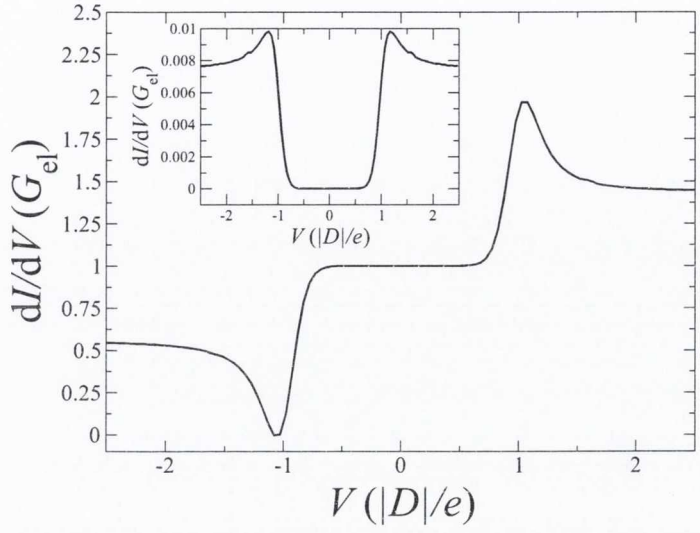

Figure 6.13: SP-IETS conductance spectrum for a TI (11, 6) ribbon with a $S = 1$ magnetic impurity attached at the upper edge. In this case the current is intense and drives the impurity spin away from the uni-axial anisotropy axis (see Fig. 6.10). Notably now there is a step in the differential conductance at the voltage corresponding to the inelastic transition $|\pm 1\rangle \rightarrow |0\rangle$, The magnitude and sign of such step depends on the bias polarity. In the inset the inelastic contribution to the conductance.

edge right-going channel) can also induce the transition $|0\rangle \rightarrow |+1\rangle$. The consequence is that the electronic current flowing at the upper edge, in virtue of its spin polarization and its intensity, produces a net flow of population between the two degenerate ground state, i.e. for $V > +|D|/e$ one has $P_{+1} > P_{-1}$. In other words the impurity spin is driven by the current away from its uni-axial anisotropy axis. This can be fully appreciated by looking at Fig. 6.11(b), where the average magnetization $\langle S^z \rangle = \sum_m P_m S^z_m$ as a function of bias is shown. Such spin-pumping is essentially identical to what happens for spin-polarized tips [28, 29] except that now one does not need either a magnetic electrode or an external magnetic field. Note that at a negative bias the effect is reversed, i.e. for $V < -|D|/e$ one has $P_{-1} > P_{+1}$, and that placing the impurity on the lower edge is equivalent to reversing the bias polarity.

The effects of the spin-pumping on the shape of the conductance spectrum are finally presented in Fig. 6.13. This time the $G(V)$ trace presents a step at the voltage corresponding to the $|\pm 1\rangle \rightarrow |0\rangle$ transition, i.e. the electron transport becomes sensitive to spin-flipping events. Such an appearance of the conductance step signals the suppression

of the topological helical states induced by the transverse magnetization of the spin impurity [125]. Intriguingly, the magnitude and sign of the conductance step depends on the bias polarity. In particular it is noted that there is an inelastic contribution, which is symmetric with respect to the sign of V, and an elastic one which is anti-symmetric, i.e. the elastic current increases for $V > |D|/e$ and decreases for $V < -|D|/e$. Placing the impurity on the opposite edge yields a mirror symmetric conductance trace (i.e. $V \rightarrow -V$).

Chapter 7

Conclusions

The interaction between conduction electrons and localized spins in transition metals with partially filled d shells is central to many low-temperature spin effects, which may underpin the development of spintronics and quantum information devices. The continuous advances in low-temperature scanning tunneling microscopy (STM) have enabled the detection of excitations of spin origin, a spectroscopy which is usually named spin-flip inelastic electron tunneling spectroscopy (SF-IETS). Crucially, this allows one to characterize the elementary spin excitations of magnetic nanostructures at the atomic level. When adsorbed on the surface of a metallic host, magnetic transition metal atoms exhibit various distinctive features in the conductance spectrum of SF-IETS experiments, which are indicative of many-body scattering between the conduction electrons and localized spins. These manifest themselves as conductance steps at voltages corresponding to the quasi-particle energies of specific magnetic excitations and as zero-bias conductance peaks, known as Kondo resonances. Many-body scattering events have been detected for Mn [5], Fe [9] and Co [7, 10] adatoms adsorbed on a CuN insulating substrate, with the latter exhibiting a Kondo peak at zero-bias. Furthermore, it has been shown that localized spins can be controlled by using out of equilibrium spin polarized STM [6]. The spin system can be driven far from equilibrium by manipulating the tip-atom distance and therefore can be forced into an opposite spin state. Such experiments on single atom systems form

the basis of SF-IETS and provide an experimental background to the theoretical work undertaken in this thesis.

The purpose of this thesis is then to formulate a theory that can appropriately describe the aforementioned experiments. Although many of these experiments can be described at the level of master equation [23, 24, 25, 26, 27, 28, 29, 30, 31], the formulation outlined in this thesis is based on the nonequilibrium Green's function method and a perturbative description of the electron-spin interaction. This is proposed to have two principle advantages over the master equation approach. Firstly, it provides the prospect of expansion to high orders in perturbation. To date, master equation treatments of the problem have stopped at the second order of perturbation. Secondly, using the Green's function formalism offers the promise of describing more complicated systems in two and three dimensions while at the same time proving more amenable to linking with ab-initio methods like density functional theory. The latter in particular has a profound effect when considering IETS on 2D and 3D topological insulators [125], which is an area of increasing interest and the prospect of which is discussed in Chapter 6. Therefore it is proposed that the formalism outlined in this thesis, though similar to the master equation procedure, offers many more advantages when dealing with more complicated materials.

The discussion began in Chapter 2 where the fundamentals of density functional theory was discussed with a view to using the *ab-initio* results as input parameters in the Green's functional formalism for transport later in the thesis. Chapters 3 and 4 then highlighted how to use Green's functions for both elastic and inelastic transport calculations. Most notably, Chapter 4 introduced the $s-d$ interaction which defines the coupling between conduction electrons and the localized spin and underpins the SF-IETS mechanism. In particular an expression for the interacting self-energy at the level of the first Born approximation in the electron-spin interaction was derived. This was used to calculate the current-voltage and the conductance-voltage curves for a 1D system of magnetically coupled spins at finite bias and in a magnetic field. In Chapter 5 it was shown that results

reproduce well the features of recent SF-IETS experiments for 1D Mn chains using parameters mostly calculated from DFT and some taken empirically from the experiments. The severe dependence of the conductance spectra on the chain parity and the selection-rule suppression of certain transitions was a direct outcome of the theory. This proved that the NEGF approach is therefore a valid alternative to master equation based schemes.

Having shown the ability of the mechanism up to second order, it was natural to expand the perturbation series further. The effects of including third order contributions to the interacting self-energy were also investigated in Chapters 4 and 5. A close expression for the third order electron-spin self-energy was derived within the NEGF formalism. Two main features in the conductance spectra emerged from the formalism, namely a logarithmic decay of the conductance as a function of bias subsequent to a conductance step and zero-bias Kondo resonances. An almost perfect quantitative agreement was obtained for the spectrum of the non-Kondo active Fe adatom, but only a qualitative one for the Kondo active Co. The level of agreement is similar for both the situations where the adatoms are isolated or when they interact with each other via the Heisenberg-like exchange interaction.

The low computational effort needed by the method makes it a valuable alternative to full many-body treatments in describing spin inelastic phenomena at the atomic level. However, to improve the Kondo results, a more rigorous treatment, including two-body Hubbard terms in the Hamiltonian might better describe the Co conductance spectra.

The lineshape details of the conductance profile of Mn atoms deposited on CuN and probed with a STM tip which can or can not carry spin-polarization was also studied. In particular the asymmetry of the conductance with the bias polarity was investigated. Firstly, the perturbative approach is extended to spin-scattering to the spin-polarized case and considered an expansion of the complex part of the electronic propagator up to the third order. This allows the reproduction of the logarithmic decay of the conductance subsequent to a conductance step, which is observed in experiments but could not be

explained by a second order theory.

When the current density was increased and the tip was spin-polarized the conductance profile started to develop a significant asymmetry with respect to the bias polarity. These were indicative of the spin system being driven out of equilibrium. A second order expansion of the spin-propagator capable of evaluating the non-equilibrium population of the various spin energy levels was derived. This was put favorably to the test against a series of experiments probing single Mn and Fe ions with a spin-polarized STM tip in an intense magnetic field. Furthermore the same formalism was capable of describing excitations occurring away from the ground state for a Mn dimer probed by a non-magnetic tip. Also in this case the agreement with experiments was very satisfactory.

Finally, in an attempt to describe the bias asymmetry in the case of non-spin-polarized STM tips an analytic expression for the real part of the electron-spin interacting self-energy was derived. This contained logarithmic peaks at the excitation energies that are odd with respect to the energy and voltage. Such parity resulted in an asymmetry in the conductance profiles. The scheme was tested for the case of a Mn monomer and a Mn trimer and compared reasonably well with experiments.

In Chapter 6 the prospect of applying the new formalism to predict possible future experiments and devices was explored. Firstly the detection of an electric field induced spin-crossover in a dimer containing two local spin 1/2 atoms using a STM-generated conductance spectrum was predicted. This was achieved by imposing a quadratic bias dependence on the exchange coupling parameter J_{dd} between the two spins. It was shown that the conductance spectra exhibit multiple spin-flip and spin-crossover features which are strongly dependent on the population of the local spin states as the ground state switches from antiferromagnetic to ferromagnetic with increasing bias. The pumping of further transitions by increasing the tip-atom coupling constant is also seen after the application of a strong magnetic field. Secondly, it was demonstrated that a quantum spin Hall (QSH) current flowing at the edge of a Z_2 topological insulator (TI) can be

used to manipulate the spin of a magnetic impurity. This did not require either an external magnetic field or magnetic electrodes, i.e. it allows one to implement spintronics without magnetism. Importantly the fingerprint of the manipulation could be found in the conductance profiles themselves, making SF-IETS a tool for preparing, manipulating and reading a quantum spin in the solid state. It also served as an appropriate test of the formalism in describing higher dimensional systems. It was found that increasing the size of the TI resulted in larger spin polarization of the edge and could only be captured by a Green's function formalism.

As regards to a future direction for the work undertaken in this thesis, focus must centre around the development of the magnetic impurity on a TI edge. The work presented in this thesis is very much in its infancy and further investigations must be performed. In particular, an intriguing situation is believed to arise when two or more magnetic atoms are placed on the TI edge. In this case it is conceivable that the two spins on one edge of the TI could be indirectly coupled each other through constant back-scattering of the conduction electrons. It would also be interesting to see what can happen if the two spins can be coupled at opposite edges of the TI. Furthermore, after gaining more insight into the fundamentals of the underlying physics of the problem, a model for a prospective read/write device should also be conceived. Since in general spin-pumping is achieved by bringing the leads closer to the scattering region in order to increase the amount of electrons in the scattering region, the proposed set-up in Chapter 6 makes this difficult to achieve in practice. It is proposed therefore that the amount of electrons entering the scattering region can be modulated by applying a gate voltage at each of the leads. This can be quite readily investigated for the model considered in this work.

Bibliography

[1] R.C. Jaklevic and J. Lambe, Phys. Rev. Lett. **17**, 1139 (1966).

[2] B.C. Stipe, M.A. Rezaei and W. Ho, Science **280**, 1732 (1998).

[3] A.J. Heinrich, J.A. Gupta, C.P. Lutz and D.M. Eigler, Science **306**, 466 (2004).

[4] D.M. Eigler and E.K. Schweizer, Nature (London) **344**, 524 (1990).

[5] C.F. Hirjibehedin, C. Lin, A.F. Otte, M. Ternes, C.P. Lutz, B.A. Jones and A.J. Heinrich, Science **317**, 1199 (2007).

[6] S. Loth,C. P. Lutz and A. J. Heinrich, Nature Physics **6**, 340 (2010)

[7] A. F. Otte, M. Ternes, K. Bergmann, S. Loth, H. Brune, C. P. Lutz, C. F. Hirjibehedin and A. J. Heinrich, *et al.*, Nature Phys, **4**, 847 (2008).

[8] J. J. Parks, A. R. Champagne, T. A. Costi, W. W. Shum, A. N. Pasupathy, E. Neuscamman, S. Flores-Torres, P. S. Cornaglia, A. A. Aligia, C. A. Balseiro, G. K.-L. Chan, H. D. Abrua and D. C. Ralph1 *et al.*, Science **328**, 1370 (2010).

[9] C.F. Hirjibehedin, C P. Lutz and A.J. Heinrich, Science **312**, 1021 (2006).

[10] A. F. Otte, M. Ternes, S. Loth, C. P. Lutz, C. F. Hirjibehedin, and A. J. Heinrich, Phys. Rev. Lett. **103**, 107203 (2009).

[11] S. Loth, C. P. Lutz and A. J. Heinrich, 2010 New J. Phys. **12** 125021

[12] X. Chen, Y.-S. Fu, S.-H. Ji, T. Zhang, P. Cheng, X.-C. Ma, X.-L. Zou, W.-H. Duan, J.-F. Jia and Q.-K. Xue, Phys. Rev. Lett. **101**, 197208 (2008).

[13] A. A. Khajetoorians, J. Wiebe, B. Chilian, R. Wiesendanger, Science **332**, 1062 (2011)

[14] S. Loth, S. Baumann, C. P. Lutz, D. M. Eigler, A. J. Heinrich, Science **335**, 196 (2012)

[15] J. Park, A. N. Pasupathy, J. I. Goldsmith, C. Chang, Y. Yaish, J. R. Petta, M. Rinkoski, J. P. Sethna, H. D. Abrua, P. L. McEuen and D. C. Ralph, Nature **417**, 722-725 (2002)

[16] C. Romeike, M. R. Wegewijs, W. Hofstetter, and H. Schoeller, Phys. Rev. Lett. **96**, 196601 (2006)

[17] T. Choi, (2011), *STM studies of charge transfer and transport through metal-molecule complexes on ultrathin insulating films*, PhD thesis, The Ohio State University

[18] T.Choi, S. Bedwani, A. Rochefort, C. Chen, A. J. Epstein and J. A. Gupta, Nano Lett., **10**, 41754180, (2010)

[19] A. R. Schmidt, M. H. Hamidian, P. Wahl, F. Meier, A. V. Balatsky, J. D. Garrett, T. J. Williams, G. M. Luke and J. C. Davis, Nature **465**, 09073, (2010)

[20] J. Paaske, A. Rosch, P. Wlfle, N. Mason, C. M. Marcus and J. Nygrd, Nature Physics **2**, 460 - 464 (2006)

[21] C. Romeike, M.R. Wegewijs and H. Schoeller, Phys. Rev. Lett. **96**, 196805 (2006).

[22] J. Tersoff and D.R. Hamann, Phys. Rev. Lett. **50**, 1998 (1983).

[23] J. Fernandez-Rossier, Phys. Rev. Lett. **102**, 256802 (2009).

[24] J. Fransson, O. Eriksson and A.V. Balatsky, Phys. Rev. B **81**, 115454 (2010).

[25] N. Lorente and J. Gauyacq, Phys. Rev. Lett. **103**, 176601 (2009).

[26] M. Persson, Phys. Rev. Lett. **103**, 050801 (2009).

[27] B. Sothmann and J. König, New J. Phys. **12**, 083028 (2010).

[28] F. Delgado, J.J. Palacios and J. Fernandez-Rossier, Phys. Rev. Lett. **104**, 026601 (2010).

[29] F. Delgado and J. Fernandez-Rossier, Phys. Rev. B **82**, 134414 (2010).

[30] F. Delgado and J. Fernandez-Rossier, Phys. Rev. Lett. **108**, 196602 (2012)

[31] F. D. Novaes, N. Lorente, and J. P. Gauyacq, Phys. Rev. B **82**, 155401 (2010)

[32] K. G. Wilson, Rev. Mod. Phys. **47**, 773 (1975).

[33] R. Zitko, R. Peters, T. Pruschke, New J. Phys. **11**, 053003 (2009).

[34] R. Zitko and T. Pruschke, New J. Phys. **12**, 063040 (2010).

[35] M. Misiorny, I. Weymann, and J. Barna, Phys. Rev. Lett. **106**, 126602 (2011).

[36] J. Paaske, A. Rosch and P. Wlfle, Phys. Rev. B **69**, 155330 (2004)

[37] L. G. G. V. Dias da Silva and E. Dagotto, Phys. Rev. B **79**, 155302 (2009)

[38] T. Hotta and K. Ueda, Phys. Rev. Lett. **108**, 247214 (2012)

[39] R. Korytar, N. Lorente and J.-P. Gauyacq, Phys. Rev. B **85**, 125434 (2012)

[40] M. Maltseva, M. Dzero, and P. Coleman, Phys. Rev. Lett. **103**, 206402 (2009)

[41] J. Figgins and D. K. Morr, Phys. Rev. Lett. **104**, 187202 (2010)

[42] F. F. Assaad, Phys. Rev. B, **65**, 115104 (2002)

[43] G. Stefanucci and S. Kurth, Phys. Rev. Lett. **107**, 216401 (2011)

[44] L.V. Keldysh, Sov. Phys. JETP **20**, 1018 (1965).

[45] S. Datta, *Electronic Transport in Mesoscopic Systems*, (Cambridge University Press, Cambridge, 1995)

[46] A.R. Rocha, V.M. Garcia-Suarez, S. Bailey, C. Lambert, J. Ferrer and S. Sanvito, Phys. Rev. B **73**, 085414 (2006).

[47] I. Rungger and S. Sanvito, Phys. Rev. B **78**, 035407 (2008).

[48] C.D. Pemmaraju, I. Rungger, X. Chen, A.R. Rocha and S. Sanvito, Phys. Rev. B **82**, 125426 (2010).

[49] M. Galperin, M.A. Ratner and A. Nitzan, J. Chem. Phys. **121**, 11965 (2004).

[50] V.P. Antropov, M.I. Katsnelson, M. van Schilfgaarde and B.N. Harmon, Phys. Rev. Lett. **79**, 729 (1995).

[51] M. Stamenova, T.N. Todorov and S. Sanvito, Phys. Rev. B **77**, 054439 (2008).

[52] A. Pertsova, M. Stamenova, and S. Sanvito, Phys. Rev. B **84**, 155436 (2011)

[53] F. Delgado and J. Fernandez-Rossier, Phys. Rev. B **84**, 045439 (2011)

[54] J. Paaske, A. Anderson, and K. Flensberg, Phys. Rev. B **82**, 081309 R (2010)

[55] M. Pletyukhov and D. Schuricht, Phys. Rev. B **84**, 041309(R) (2011)

[56] T. Balashov, T. Schuh, A. F. Takacs, A. Ernst, S. Ostanin, J. Henk, I. Mertig, P. Bruno, T. Miyamachi, S. Suga and W. Wulfhekel, Phys. Rev. Lett., **102**, 257203 (2009)

[57] Piotr Bonski and Jürgen Hafner, J. Phys.: Condens. Matter **21**, 426001 (2009)

[58] S. Lounis, P. Mavropoulos, P. H. Dederichs, and S. Blgel, Phys. Rev. B **73**, 195421 2006

[59] S. Loth, M. Etzkorn, C. P. Lutz, D. M. Eigler and A. J. Heinrich, Science, **329**, 5999 (2010)

[60] B. Chilian, A. A. Khajetoorians, S. Lounis, A. T. Costa, D. L. Mills, J. Wiebe, and R. Wiesendanger, Phys. Rev. B **84**, 212401 (2011)

[61] N. Baadji, M. Piacenza, T. Tugsuz, F. D. Sala, G. Maruccio and S. Sanvito, Nature Materials **8**, 813 - 817 (2009) .

[62] M. Diefenbach and K.S. Kim, Angew. Chem., Int. Ed. **46**,7640 (2007).

[63] G. A. Timco, S. Carretta, F. Troiani, F. Tuna, R. J. Pritchard, C. A. Muryn, E. J. L. McInnes, A. Ghirri, A. Candini, P. Santini, G. Amoretti, M. Affronte and R. E. P. Winpenny, Nat. Nanotechnol. **4**, 173 (2009)

[64] S. K. Shukla and S. Sanvito, Phys. Rev. B **80**, 184429 (2009)

[65] C.L. Kane and E.J. Mele, Phys. Rev. Lett **95**, 226801 (2005).

[66] C.L. Kane and E.J. Mele, Phys. Rev. Lett **95**, 146802 (2005).

[67] B.A. Bernevig, T.L. Hughes and S.C. Zhang, Science **314**, 1757 (2006).

[68] M. König, S. Wiedmann, C. Brüne, A. Roth, H. Buhmann, L.W. Molenkamp, X.L. Q and S.C. Zhang, Science **318**, 766 (2007).

[69] A. Roth, C. Brüne, H. Buhmann, L.W. Molenkamp, J. Maciejko, X.L. Qi and S.C. Zhang, Science **325**, 294 (2009).

[70] I. Knez, R.R. Du and G. Sullivan, Phys. Rev. Lett **107**, 136603 (2011).

[71] C.-C. Liu, W. Feng and Y. Yao, Phys. Rev. Lett **107**, 076802 (2011).

[72] M. Ezawa, New Journal of Physics **14**, 033003 (2012).

[73] C. Weeks, J. Hu, J. Alicea, M. Franz and R. Wu, Phys. Rev. X **1**, 021001 (2011).

[74] J. Maciejko, Phys. Rev. B **85**, 245108 (2012).

[75] A.M. Lunde and G. Platero, Phys. Rev. B **86**, 035112 (2012).

[76] R.G. Parr and W. Yang.*Density-functional theory of atoms and molecules.* vol. 16 of The International Series of Monographs on Chemistry, Oxford University Press, Oxford, UK, (1989)

[77] H. Hohenberg and W. Kohn. Phys. Rev., 136:B864, 1964.

[78] W. Kohn and L.J. Sham. Phys. Rev., 140:A1133, 1965.

[79] R.M. Martin. Electronic Structure: Basic Theory and Practical Methods. Cambridge University Press, Cambridge, UK, (1989)

[80] M. Levy, Proceedings of the National Academy of Sciences, **76** (12): 60626065 (1979).

[81] M. A. L. Marques, E. K. U. Gross, C. Fiolhais and F. Nogueira, Time-Dependent Density Functional Theory, Springer (2003).

[82] D.C. Langreth and M.J. Mehl. Phys. Rev. B, 28:1809, 1983.

[83] J.P. Perdew. Phys. Rev. Lett., 55:1665, 1985.

[84] J.P. Perdew, K. Burke, and M. Ernzerhof. Phys. Rev. Lett., 77:3865, 1996.

[85] C.D. Pemmaraju, S. Sanvito, and K. Burke. cond-mat/07082814.

[86] T. Körzdörfer, M. Mundt, and S. Kümmel. cond-mat/07082870

[87] V.I. Anisimov, F. Aryasetiawan and A.I.Lichtenstein, J. Phys.: Condens. Matter **9**, 767 (1997)

[88] V. I. Anisimov, J. Zaanen, and O. K. Andersen, Phys. Rev. B. **44**, 943 (1991)

[89] V. I. Anisimov, M. A. Korotin, J. A. Zaanen, and O. K. Anderson, Phys. Rev. Lett. **68**, 345 (1992).

[90] C. Tablero, J. Phys.: Condens. Matter **20**, 325205 (2008).

[91] M. T. Czyzyk and G. A. Sawatzsky, Phys. Rev. B **40**, 14211 (1994).

[92] M. Cococcioni and S. Gironcoli, Phys. Rev. B **71**, 035105 (2005).

[93] N. Troullier and J.L. Martins. Phys. Rev. B, 43:1993, 1991.

[94] L. Kleinman and D.M. Bylander. Phys. Rev. Lett., 48:1425, 1982.

[95] L. Kleinman, Phys. Rev. B **21**, 26301 (1980)

[96] G. B. Bachelet and M. Schüter Phys. Rev. B 25 21038 (1982)

[97] L Fernandez-Seivane, M AOliveira, S Sanvito and J Ferrer, J. Phys.: Condens. Matter **18** 79998013 (2006)

[98] G. D. Mahan, *Many-Particle Physics*, (Plenum Press, New York, 2nd edition, 1990)

[99] M. Gell-Mann and F. Low, Phys. Rev. **84**, 350354 (1951)

[100] J. Schwinger, J. Math. Phys. **2**, 407 (1961)

[101] G.C. Wick, Phys. Rev. **80**, 268 - 272 (1950)

[102] H. Haug and A.P. Jauho, *Quantum Kinetics in Transport and Optics of Semiconductors*, (Springer, 1996)

[103] J. Kondo, Prog. Theor, Phys. 32, 37 (1964)

[104] P.W. Anderson, Phys. Rev. 124 (1961)

[105] Hubbard, J. Proceedings of the Royal Society of London **276** (1365): 238257 (1963)

[106] K. Yosida, *Theory of Magnetism*, (Springer-Verlag, Berlin, 1996)

[107] D. Coffey, T. M. Rice, and F. C. Zhang, Phys. Rev. B **44**, 1011210116 (1991)

[108] X. Wang, C.D. Spataru, M.S. Hybertsen and A.J. Millis, Phys. Rev. B **77**, 045119 (2008).

[109] T. Frederiksen, M. Brandbyge, N. Lorente and A. P. Jauho, J. Comput. Electron. **3**, 423 (2004).

[110] P. Hyldgaard, S. Hershfield, J. H. Davies, and J. W. Wilkins, Ann. Phys. (N.Y.) **236**, 1 (1994).

[111] A. Yanik, G. Klimeck and S. Datta, Phys. Rev. B **76**, 045213 (2007).

[112] W. Lee, N. Jean and S. Sanvito, Phys. Rev. B **79**, 085120 (2009).

[113] J.M.D. Coey, *Magnetism and Magnetic Materials*, Oxford University Press, 2009.

[114] P. E. Blöchl, Phys. Rev. B **50**, 17953 (1994)

[115] A. N. Rudenko, V. V. Mazurenko, V. I. Anisimov and A. I. Lichtenstein, Phys. Rev. B **79**, 144418 (2009)

[116] P. Lucignano, R. Mazzarello, A. Smogunov, M. Fabrizio and E. Tosatti, Nature Materials, **8**, 563 (2009).

[117] A. B. Shick, F. Mca, and A. I. Lichtenstein, J. Appl. Phys. **105**, 07C309 (2009)

[118] J. R. Schrieffer and P. A. Wolff, Phys. Rev. **149**, 491 (1966).

[119] F. Elste and C. Timm, Phys. Rev. B **81**, 024421 (2010).

[120] O. Újsághy, J. Kroha, L. Szunyogh and A. Zawadowski, Phys. Rev. Lett **85**, 2557 (2000).

[121] M. N. Leuenberger and E. R. Mucciolo, Phys. Rev. Lett **106**, 126601 (2006).

[122] U. Fano, Phys. Rev. **124**, 18661878 (1961)

[123] M. Buttiker, Phys. Rev. B **38**, 9375 (1988).

[124] L. Sheng, D.N. Sheng, C.S. Ting, and F.D.M. Haldane, Phys. Rev. Lett **95**, 136602 (2005).

[125] A. Narayan and S. Sanvito, Phys. Rev. B **86**, 041104(R) (2012).

[126] S. Sanvito, C. J. Lambert, J. H. Jefferson and A. M. Bratkovsky, Phys. Rev. B **59**, 11936 (1999).

Appendix A

Surface Green's function and Broadening

The self-energy of the substrate (sub) and the tip (tip) as introduced in Chapter 3 for the non-interacting case of transport through a scattering region can be expressed as follows in terms of the surface Green's functions, $\hat{g}_{\mathrm{tip}}$ and $\hat{g}_{\mathrm{sub}}$, and the coupling matrices between the leads and the scattering region $H_{\alpha-\mathrm{S}}$ (α=tip, sub)

$$\Sigma_{\mathrm{tip}}(\omega) = H^{\dagger}_{\mathrm{tip-S}}\, \hat{g}_{\mathrm{tip}}(\omega)\, H_{\mathrm{tip-S}}\,, \tag{A1}$$

$$\Sigma_{\mathrm{sub}}(\omega) = H_{\mathrm{sub-S}}\, \hat{g}_{\mathrm{sub}}(\omega)\, H^{\dagger}_{\mathrm{sub-S}}\,. \tag{A2}$$

The surface Green's functions can be found by first constructing the Green's function for an infinite system and then by applying the appropriate boundary conditions [126]. For a single-ste nearest-neighbour one-dimensional tight-binding chain $\hat{g}_{\alpha}$ takes a simple close form

$$\hat{g}_{\mathrm{tip}}(\omega) = \hat{g}_{\mathrm{sub}}(\omega) = \frac{1}{\gamma_0} e^{ik(\omega)}\,, \tag{A3}$$

$$k(\omega) = \cos^{-1}\left(\frac{\omega - \varepsilon_0}{2\gamma_0}\right), \tag{A4}$$

where $k(\omega)$ and γ_0 are respectively the inverse dispersion relation (k vs. ω) and the hopping parameter. Equal hopping parameters in the leads are assumed. The interaction between the

scattering region and the leads has the effect of broadening the scattering region's discrete energy levels. The broadening function due to the coupling to the leads is defined as:

$$\Gamma_{\text{tip}}(\omega) = i(\Sigma_{\text{tip}}(\omega) - \Sigma^{\dagger}_{\text{tip}}(\omega)), \tag{A.5}$$

$$\Gamma_{\text{sub}}(\omega) = i(\Sigma_{\text{sub}}(\omega) - \Sigma^{\dagger}_{\text{sub}}(\omega)), \tag{A.6}$$

which for coupling constants γ_{tip} and γ_{sub} can be rexpressed as [using Eqs. (A.1)-(A.4)] as

$$\Gamma_{\text{tip}}(\omega) = \frac{2\gamma^2_{\text{tip}}}{\gamma_0}\sqrt{1 - \left(\frac{\omega - \varepsilon_0}{2\gamma_0}\right)^2}, \tag{A.7}$$

$$\Gamma_{\text{sub}}(\omega) = \frac{2\gamma^2_{\text{sub}}}{\gamma_0}\sqrt{1 - \left(\frac{\omega - \varepsilon_0}{2\gamma_0}\right)^2}. \tag{A.8}$$

Appendix B

Spin operators

The spin operators that are used throughout this thesis and have been introduced first in section 4.1 of Chapter 4) obey the following commutation relations for all directions $i = \{x, y, z\}$ (note $\hbar = 1$)

$$[S_i, S_j] = i\varepsilon_{ijk}S_k, \tag{B.1}$$

where ε_{ijk} is the Levi-Civita symbol. A good quantum number is defined as the eigenvalue of a given operator whose eigenvectors remain the same, with the same eigenvalue, as time evolves. For a basis set that spans the spin quantum numbers $m = \{-S, -S+1, ..., S-1, S\}$ where S is the total quantum spin it can be shown that the only "good" quantum numbers in the spin system are the eigenvalues of the operators S^2 and S_z

$$S^2|S, m\rangle = S(S+1)|S, m\rangle, \tag{B.2}$$

$$S_z|S, m\rangle = m|S, m\rangle, \tag{B.3}$$

and these operators correspondingly commute $[S^2, S_z] = 0$. It is useful also to define the raising and lowering operators $S_\pm$, which obey the following relation for raising or lowering the quantum

number m

$$S_{\pm}|S,m\rangle = \sqrt{S(S+1) - m(m\pm 1)}|S,m\pm 1\rangle, \tag{B.4}$$

where $S_{\pm} = S_x \pm iS_y$.

In the special case where where the total spin $S = 1/2$, the spin operators can be expressed in terms of the Pauli matrices

$$\sigma_x = \begin{pmatrix} 0 & 1 \\ 1 & 0 \end{pmatrix}, \quad \sigma_y = \begin{pmatrix} 0 & -i \\ i & 0 \end{pmatrix}, \quad \sigma_z = \begin{pmatrix} 1 & 0 \\ 0 & -1 \end{pmatrix}, \tag{B.5}$$

where $S_i = \sigma_i/2$.

Appendix C

Derivation of third order self-energy

In this appendix it will be shown how the integral in Eq. (4.31) is evaluated over the time-ordered contour τ_2. The part of the self-energy in Eq. (4.31), which is of interest, will be denoted by $\mathcal{I}$ and it is written as follows

$$\mathcal{I}(\tau_1,\tau_3) = \sum_{m,n,l} D_m(\tau_3,\tau_1) \int_C d\tau_2 G_0(\tau_1,\tau_2) G_0(\tau_2,\tau_3) D_n(\tau_1,\tau_2) D_l(\tau_2,\tau_3)\,. \tag{C.1}$$

In order to express the quantity above in terms of real time integrals over a contour going first from $-\infty \to +\infty$ and then from $+\infty \to -\infty$ [44] is performed so that only the ground-state at $t = -\infty$ is well defined. The various branches along the contour result in four different Green's function, which are illustrated in Fig. 3.1. These are respectively the lesser and the greater Green's functions ($G^<$ and $G^>$) and both the time ordered and anti-ordered Green's functions (G^t and $G^{\bar{t}}$). The lesser ($<$) contributions to $\mathcal{I}$ enter into Eq. (C.1) as

$$\begin{aligned}
\mathcal{I}^<(t_1,t_3) &= \sum_{m,n,l} D_m^>(t_3,t_1)\times \\
&\Big\{ \int_{-\infty}^{+\infty} dt_2 G_0^t(t_1,t_2) G_0^<(t_2,t_3) D_n^t(t_1,t_2) D_l^<(t_2,t_3) \\
&+ \int_{+\infty}^{-\infty} dt_2 G_0^{\bar{t}}(t_1,t_2) G_0^>(t_2,t_3) D_n^{\bar{t}}(t_1,t_2) D_l^>(t_2,t_3) \Big\}
\end{aligned} \tag{C.2}$$

where one defines $G_0^t(t,t') = G_0^<(t,t') + G_0^r(t,t')$ and $G_0^{\bar{t}}(t,t') = G_0^<(t,t') - G_0^a(t,t')$. If these expressions are now inserted into Eq. (C.1) eight integrals are obtained that can be evaluated separately. These are

$$\begin{aligned}
\mathcal{I}^<(t_1,t_3) = & \sum_{m,n,l} D_m^>(t_3,t_1)\times \\
& \Big\{ \int_{-\infty}^{+\infty} d\tau_2 G_0^r(t_1,t_2) G_0^<(t_2,t_3) D_n^r(t_1,t_2) D_l^<(t_2,t_3) \\
& + \int_{-\infty}^{+\infty} dt_2 G_0^r(t_1,t_2) G_0^<(t_2,t_3) D_n^<(t_1,t_2) D_l^<(t_2,t_3) \\
& + \int_{-\infty}^{+\infty} dt_2 G_0^<(t_1,t_2) G_0^<(t_2,t_3) D_n^r(t_1,t_2) D_l^<(t_2,t_3) \\
& + \int_{-\infty}^{+\infty} dt_2 G_0^<(t_1,t_2) G_0^<(t_2,t_3) D_n^<(t_1,t_2) D_l^<(t_2,t_3) \\
& - \int_{-\infty}^{+\infty} dt_2 G_0^<(t_1,t_2) G_0^<(t_2,t_3) D_n^<(t_1,t_2) D_l^<(t_2,t_3) \\
& + \int_{-\infty}^{+\infty} dt_2 G_0^<(t_1,t_2) G_0^<(t_2,t_3) D_n^<(t_1,t_2) D_l^a(t_2,t_3) \\
& + \int_{-\infty}^{+\infty} dt_2 G_0^<(t_1,t_2) G_0^a(t_2,t_3) D_n^<(t_1,t_2) D_l^<(t_2,t_3) \\
& - \int_{-\infty}^{+\infty} dt_2 G_0^<(t_1,t_2) G_0^a(t_2,t_3) D_n^<(t_1,t_2) D_l^a(t_2,t_3) \Big\} .
\end{aligned} \tag{C.3}$$

Importantly several of these integrals cancel each other, while a few other can be grouped together by using the various definitions of $G^{\lessgtr}$ and $G^{r/a}$ [98, 109]. By performing these simplifications one finally obtains a much more compact expression

$$\begin{aligned}
\mathcal{I}^<(t_1,t_3) = 2 \sum_{m,n,l} D_m^>(t_3,t_1) \Big\{ & \int_{-\infty}^{+\infty} dt_2 G_0^r(t_1,t_2) G_0^<(t_2,t_3) D_n^<(t_1,t_2) D_l^<(t_2,t_3) \\
& + \int_{-\infty}^{+\infty} dt_2 G_0^<(t_1,t_2) G_0^<(t_2,t_3) D_n^r(t_1,t_2) D_l^<(t_2,t_3) \Big\} ,
\end{aligned} \tag{C.4}$$

which after performing the integration over t_2 becomes

$$\mathcal{I}^<(t_1,t_3) = 2\sum_{m,n,l} P_l(1-P_m)\int\int d\omega d\omega' e^{i(\varepsilon_m-\omega-\omega')(t_1-t_3)}$$
$$\times\left\{G_0^r(\omega)G_0^<(\omega+\omega'-\varepsilon_l)P_n\delta(\omega'-\varepsilon_n)+G_0^<(\omega)G_0^<(\omega+\omega'-\varepsilon_l)D_n^r(\omega')\right\}. \qquad \text{(C.5)}$$

Note here that $G_0^r(\omega) = 1/(\omega-\varepsilon_0+i\Gamma_s)$ and $G_0^<(\omega) = \Gamma_s f_s(\omega)/[(\omega-\varepsilon_0)^2+\Gamma_s^2]$ (refer to Chapter 3). Again it is assumed that the coupling to the tip is negligible leaving only the contribution to the broadening from the substrate. This is governed by the Fermi function $f_s(\omega)$. The spin subsystem is assumed to be weakly coupled to a surrounding heat bath kept at a temperature T, which ensures that the system remains in thermal equilibrium. Therefore, to a good approximation, one can write $D_m^r(\omega) = 1/(\omega-\varepsilon_m+ik_BT)$ and $D_m^<(\omega) = P_n\delta(\omega-\varepsilon_m)$. In the latter it has been assumed that k_BT is small enough that the lesser Green's function can be approximated by a delta-function multiplied by the occupation of the specific spin state. With this information at hand one notes that the first term in the curly brackets in Eq. (C.5) will not produce a logarithmic Kondo term but represents merely a small third order correction to the scattering and can thus be neglected, as also found in Ref. [98]. The second term contains the interesting third order contribution which after Fourier transform becomes

$$\mathcal{I}^<(E) = 2\sum_{m,n,l} P_l(1-P_m)G_0^<(E+\varepsilon_m-\varepsilon_l)\int_{-W}^{+W} d\omega G_0^<(\omega)\mathrm{Re}[D_n^r(E-\omega+\varepsilon_m)]\,. \qquad \text{(C.6)}$$

Here the real part of D_n^r has been kept since the only interesting quantity is $\mathrm{Im}\mathcal{I}^r(E) = [\mathcal{I}^<(E)+\mathcal{I}^>(E)]/2$. The effect of $\mathrm{Re}\mathcal{I}^r(E)$ on the conductance is negligible in the case $\varepsilon_0 \gg \varepsilon_F$. It is also due to this fact that the density of states ρ around ε_F is approximately constant and therefore can be taken outside of the integral in Eq. (C.6). This leads to a new expression for $\mathcal{I}^<(E)$, which reads

$$\mathcal{I}^<(E) = 2\sum_{m,n,l} P_l(1-P_m)G_0^<(E+\varepsilon_m-\varepsilon_l)\rho\int_{-W}^{-V} d\omega\mathrm{Re}\Big[\frac{1}{(E-\omega+\varepsilon_m-\varepsilon_n)+ik_BT}\Big]\,. \qquad \text{(C.7)}$$

Finally the integral is performed and the entire procedure for $\mathcal{I}^{>}(E)$ is repeated. One then arrives at the final expression which reveals the logarithmic divergences present at the allowed transitions

$$\mathcal{I}^{\lessgtr}(E) = -2 \sum_{m,n,l} P_l(1 - P_m) G_0^{\lessgtr}(E \pm \Omega_{ml}) \rho \ln\left[\frac{W^2}{(E + V \pm \Omega_{mn})^2 + (k_B T)^2}\right]. \tag{C.8}$$

Appendix D

Derivation of transition rates

In this appendix the steady-state non-equilibrium distribution of the population, $P_m(V)$, of the spin system as the broadening due to coupling to the tip, $\Gamma_{\text{tip-S}}$, is increased will be calculated. In order to do so equation (4.22) is expanded up to the n-th order in the interaction Hamiltonian

$$[D(\tau,\tau')]_{n,m} = \sum_n \frac{(-i)^{n+1}}{n!} \int_C d\tau_1 \ldots \int_C d\tau_n \, \frac{\langle 0|T_C\{H_{\text{e-sp}}(\tau_1)\ldots H_{\text{e-sp}}(\tau_n)d_n(\tau)d_m^\dagger(\tau')\}|0\rangle}{U(-\infty,-\infty)}, \tag{D.1}$$

where U is the time-evolution unitary operator and the time-averages are over the known non-interacting ($J_{\text{sd}} = 0$) ground state $|0\rangle$. The time integration over τ is ordered on the contour C going from $-\infty$ to $+\infty$ and then returning from $+\infty$ to $-\infty$ [102].

Inserting the expression for $H_{\text{e-sp}}$ from Eq. (4.15) into the above and expanding to second order one gets [note for ease of description the elastic contribution of J_0 is omitted but is included in the final expression in Eq. (D.7)]

$$[D(\tau,\tau')]^{(2)}_{n,m} = \frac{(-i)^3}{2!} J_{\text{sd}}^2 \sum_{\alpha,\alpha',\beta,\beta'} \int_C d\tau_1 \int_C d\tau_2 \, \langle 0|T_C\{c_\alpha^\dagger(\tau_1)c_{\alpha'}(\tau_1)c_\beta^\dagger(\tau_2)c_{\beta'}(\tau_2)d_n(\tau)d_m^\dagger(\tau')\}|0\rangle$$
$$\times \sum_{i,j} \langle 0|T_C\{S^i(\tau_1)S^j(\tau_2)\}|0\rangle [\sigma^i]_{\alpha\alpha'}[\sigma^j]_{\beta\beta'}, \tag{D.2}$$

where the indexes i and j run over the Cartesian coordinates x, y and z for the given spin connected to the tip. The operator breakdown of the spin from Eq. (4.21) is now substituted

into Eq. (D.2)

$$[D(\tau,\tau')]^{(2)}_{n,m} = \frac{(-i)^3}{2!} J^2_{\rm sd} \sum_{k,k',l,l'} \int_C d\tau_1 \int_C d\tau_2 \langle 0|T_C\{d_n(\tau) d^\dagger_k(\tau_1) d_{k'}(\tau_1) d^\dagger_l(\tau_2) d_{l'}(\tau_2) d^\dagger_m(\tau')\}|0\rangle$$
$$\times \sum_{\alpha,\alpha',\beta,\beta'} \langle 0|T_C\{c_{\alpha'}(\tau_1) c^\dagger_\beta(\tau_2) c_{\beta'}(\tau_2) c^\dagger_\alpha(\tau_1)\}|0\rangle \sum_{i,j} S^i_{kk'} S^j_{ll'} [\sigma^i]_{\alpha\alpha'} [\sigma^j]_{\beta\beta'}. \quad \text{(D.3)}$$

The time-ordered contractions of the two brackets in Eq. (D.3) can be re-written in terms of their respective non-interacting Green's functions, $D_0(\tau,\tau')$ and $G_0(\tau,\tau')$ as follows:

$$[D(\tau,\tau')]^{(2)}_{n,m} = - J^2_{\rm sd} \sum_{k,k',l,l'} \int_C d\tau_1 \int_C d\tau_2 \delta_{nk}\delta_{lk'}\delta_{ml'} [D_0(\tau,\tau_1)]_{n,n} [D_0(\tau_1,\tau_2)]_{l,l} [D_0(\tau_2,\tau')]_{m,m}$$
$$\times \sum_{\alpha,\alpha',\beta,\beta'} \delta_{\alpha'\beta}\delta_{\alpha\beta'} [G_0(\tau_1,\tau_2)]_{\beta\beta} [G_0(\tau_2,\tau_1)]_{\alpha\alpha} \sum_{i,j} S^i_{kk'} S^j_{ll'} [\sigma^i]_{\alpha\alpha'} [\sigma^j]_{\beta\beta'}, \quad \text{(D.4)}$$

where the extra factor of 2 emerges from the fact that a second contraction of the time-ordered bracket merely exchanges τ_1 and τ_2. Then, by using Dyson's equation [98], one can write the second order contribution to the interacting spin self-energy (Π) which reads

$$[\Pi(\tau_1,\tau_2)]^{(2)}_{n,m} = -2J^2_{\rm sd} \sum_{\alpha,\beta} [G_0(\tau_1,\tau_2)]_{\beta\beta} [G_0(\tau_2,\tau_1)]_{\alpha\alpha} \sum_l [D_0(\tau_1,\tau_2)]_{l,l} \sum_{i,j} S^i_{nl} S^j_{lm} [\sigma^i]_{\alpha\beta} [\sigma^j]_{\beta\alpha}, \quad \text{(D.5)}$$

where the assumption that the electrons are spin degenerate has been used thus omitting the spin index on $G_0(\tau_1,\tau_2)$ and including a factor of 2. The real-time quantities are now calculated, such as the lesser (greater) self-energies, by using the Langreth's theorem for time ordering over the defined contour [102]. After including the elastic contribution one gets

$$[\Pi^{\lessgtr}(t_1,t_2)]^{(2)}_{n,m} = - 2J^2_{\rm sd} \sum_{\alpha,\beta} [G^{\lessgtr}_0(t_1,t_2)]_{\beta\beta} [G^{\gtrless}_0(t_2,t_1)]_{\alpha\alpha} \sum_l [D^{\lessgtr}_0(t_1,t_2)]_{l,l}$$
$$\times \sum_{i,j} \Big(S^i_{nl} S^j_{lm} [\sigma^i]_{\alpha\beta} [\sigma^j]_{\beta\alpha} + \delta_{ij}\delta_{\alpha\beta} \chi S^i_{nm} [\sigma^i]_{\alpha\beta} \Big). \quad \text{(D.6)}$$

In computing the Fourier transform it is noted the two different expressions for the lesser and

greater Green's functions are

$$[\Pi^{\lessgtr}(E)]^{(2)}_{n,m} = -\frac{J_{\mathrm{sd}}^2}{\pi}\sum_{l} P_l^{\lessgtr}\sum_{\alpha,\beta}\int_{-\infty}^{+\infty} d\omega [G_0^{<}(\omega)]_{\beta\beta}[G_0^{>}(\omega \pm (E-\varepsilon_l))]_{\alpha\alpha}\times$$
$$\sum_{i,j}\Big(S^i_{nl}S^j_{lm}[\sigma^i]_{\alpha\beta}[\sigma^j]_{\beta\alpha} + \delta_{ij}\delta_{\alpha\beta}\chi S^i_{nm}[\sigma^i]_{\alpha\beta}\Big), \tag{D.7}$$

where one defines $P_l^{<} = P_l$ and $P_l^{>} = 1 - P_l$ and $D_0^{\lessgtr}(t_1,t_2)_{l,l} = P_l^{\lessgtr}\exp[-i\varepsilon_l(t_1-t_2)/\hbar]$. Assuming that the spin system is in thermal contact with a heat bath of temperature T, the energy levels ε_l should be broadened by the factor $\beta = k_B T$ but this can be neglected for ease of calculation since in general $T << 1$. However the broadening in the electronic Green's function due to contact to tip and substrate is not disregarded as this is pivotal to the calculation of the non-equilibrium spin populations.

Appendix E

Explicit form for the current vs bias

In this section, an explicit form for the bias-dependent current introduced in Chapter 4 will be derived as this offers a more clear picture of the physics behind the spin-crossover effect discussed in Chapter 6. The original form of the current in terms of the full many-body Green's functions is recalled from Eq. (4.47)

$$I_\eta = \int_{-\infty}^{+\infty} d\omega \Big[\Sigma_\eta^<(\omega)G^>(\omega) - \Sigma_\eta^>(\omega)G^<(\omega)\Big], \tag{E.1}$$

where $\Sigma_\eta^< = \Gamma_\eta f_\eta$ and $\Sigma_\eta^> = \Gamma_\eta(1 - f_\eta)$. $f_\eta(\omega) = 1/[1 + \exp(\frac{\omega - \mu_\eta}{k_B T})]$. The full interacting lesser and greater Green's functions, as they appear in the above equation, are written in terms of the retarded and advanced Green's functions and the interacting and lead self energies

$$G^\lessgtr = G^r\Big(\Sigma_L^\lessgtr + \Sigma_R^\lessgtr + \Sigma_{\text{int}}^\lessgtr\Big)G^a, \tag{E.2}$$

$$\approx \frac{\rho}{\Gamma}\Big(\Sigma_L^\lessgtr + \Sigma_R^\lessgtr + \Sigma_{\text{int}}^\lessgtr\Big), \tag{E.3}$$

where the density of states at the Fermi energy ε_F is $\rho = \Gamma/[(\varepsilon_0)^2 + \Gamma^2]$ and $\Gamma = \Gamma_\text{L} + \Gamma_\text{R}$. The above approximation can be written by assuming that the onsite energy ε_0 is far enough from the Fermi energy so that the density of states can be assumed constant. The interacting

self-energy is the one derived earlier in Chapter 3

$$\Sigma^{\lessgtr}_{\rm int}(\omega)^{(2)} = -2J^2_{\rm sd}\sum_{i,m,n}|\langle m|S^i|n\rangle|^2 P_n(1-P_m)G_0^{\lessgtr}(\omega \pm \Omega_{mn})\,. \tag{E.4}$$

Inserting this into the expression for the current one arrives at

$$I_\eta = \rho\frac{\Gamma_L\Gamma_R}{\Gamma}\int_{-\infty}^{+\infty}\Big\{f_L(\omega)[1-f_R(\omega)] - [1-f_L(\omega)]f_R(\omega) \tag{E.5}$$

$$- 2J^2_{\rm sd}\frac{\rho}{\Gamma}\sum_{i,m,n}|S^i_{mn}|^2 P_n(1-P_m)f_L(\omega)[1-f_R(\omega-\Omega_{mn})] \tag{E.6}$$

$$+ 2J^2_{\rm sd}\frac{\rho}{\Gamma}\sum_{i,m,n}|S^i_{mn}|^2 P_n(1-P_m)[1-f_L(\omega)]f_R(\omega+\Omega_{mn})]\Big\}d\omega, \tag{E.7}$$

where a number of equal quantities have been canceled out. At this point one can use the following result

$$\int_{-\infty}^{+\infty} f_\eta(\omega)[1-f_{\eta'}(\omega-\Omega_{mn})]d\omega = \zeta(\mu_\eta-\mu_{\eta'}-\Omega_{mn}) = \frac{\mu_\eta-\mu_{\eta'}-\Omega_{mn}}{1-\exp[-\frac{\mu_\eta-\mu_{\eta'}-\Omega_{mn}}{k_BT}]}. \tag{E.8}$$

Finally, the explicit form of the normalized current with respect to the bias can be written as

$$I(V)/G_0 = V + \frac{\rho J^2_{\rm sd}}{\Gamma}\sum_{i,m,k}|S^i_{nl}|^2 P_k(1-P_m)i_-(V-\Omega_{mk}), \tag{E.9}$$

where the quantity $i_-(V-\Omega_{mk}) = \zeta(V-\Omega_{mk}) - \zeta(-V-\Omega_{mk})$ has been defined. The normalization constant is the non-interacting conductance $G_0 = 2\rho\frac{\Gamma_L\Gamma_R}{\Gamma}$.

Appendix F

Publications stemming from this work

Spin-flip inelastic electron tunneling spectroscopy in atomic chains, A. Hurley, N. Baadji and S. Sanvito, Phys. Rev. B **84**, 035427 (2011).

Perturbative approach to the Kondo effect in magnetic atoms on nonmagnetic substrates, A. Hurley, N. Baadji and S. Sanvito, Phys. Rev. B **84**, 115435 (2011).

Bias asymmetry in the conductance profile of magnetic ions on surfaces probed by scanning tunneling microscopy, A. Hurley, N. Baadji, and S. Sanvito, Phys. Rev. **86**, 125411 (2012)

Spin-pumping and inelastic electron tunneling spectroscopy in topological insulators, A. Hurley, A. Narayan and S. Sanvito, arXiv:1209.1579 (2012).

Observation of the electric field induced spin-crossover effect in magnetic molecules, A. Hurley, N. Baadji and S. Sanvito, In preparation.